NTNU – Trondheim
Norwegian University of
Science and Technology

Characterisation of quantum dot-intermediate band solar cells with optical spectroscopy

Andreas Liudi-Mulyo

Condensed Matter Physics
Submission date: August 2013
Supervisor: Morten Kildemo, IFY
Co-supervisor: Turrid Worren Reenaas, IFY
Lars Martin Sandvik Aas, IFY

Norwegian University of Science and Technology
Department of Physics

Abstract

This report describes the development of a photoreflectance (PR) technique in order to study InAs/GaAs quantum dots-based intermediate band solar cells (QD-IBSC). The motivation for this study, is that PR has previously been applied to detect the optical transitions involving the intermediate band as well as the excited states of the quantum dots (QDs). Such excited states are detrimental for the QD-IBSC performance, and they are not readily detected by photoluminescence (PL).

The PR signals show several unique peaks for all samples, related to their properties. The Franz-Keldysh oscillations (FKO) are observed and the fitting is done by using Airy function. These oscillations can be used to determine electro-optic energy and the built-in electric field. Energy bandgap of the various materials composing the sample ($Al_{0.3}Ga_{0.7}As$, GaAs, wetting layer (WL) and QDs) is resolved using first derivative Lorentzian lineshape function.

To complement PR findings, PL measurements for a wide range of excitation energies are conducted at room-temperature. The energy bandgap of the WL is identified in the low PL excitation energy.

Acknowledgement

At the beginning of this work, I did not realize how this study would develop. As the time passed, the level of difficulty was gradually increased. Fortunately, I have great supervisors to support me in finishing what I have started. **Prof. Morten Kildemo** for his commitment, advice and discussion in PR. I would also like to thank **Prof. Turrid Worren Reenaas**, from whom I get the sample and help in analyzing the PL result. My gratitude also goes to **Lars Martin Aas**, for his practical knowledge in the key concept of PR and PL. I am also indebted to **Daniel Skåre**, who was staff engineer in the Prof. Morten's lab, for help regarding detail in PR experiment. Time and their dedication in this study are priceless.

Facing the same tense situation during my master education with other students: Andrew Dibbs, Andrea Klubička, Frew Gabramehedin, Mona Karbaschi, Maryam Vatanparast, Polina Dobrovolskaia and Sethulakshmy Jayakumari; It has become strong reason for me to keep struggling when the harsh and unexpected condition met. Each of them shows their unique determination and commitment from which I can learn and applied to myself. I am blessed to have them as my first international classmate.

Uncountable number of memories, kindness and supports I have received during my two years stay in Trondheim. Starting from all of my friends in Indonesia Bible Study Group, the congregation of Trondheim Baptist Church, and also Indonesia Student Association in Trondheim. Undoubtedly, they have become already part of my life.

My final acknowledgement belongs to my parents for believing me to pursue my dream in Norway. Though we are separated in 15.902 km, one thing I believe, their everlasting love has guided me reaching the finish line of my master education.

Without all of them, this report is not possible to finish.

Trondheim, August 2013

Table of Contents

List of Tables

List of Figures

Nomenclature

Acronyms

AC, a.c.	modulated signal
0D	zero-dimensional
2D	two-dimensional
2DEG	two dimensional electron gas
3D	three-dimensional
BE	bound exciton
CB	conduction band
DC, d.c.	unmodulated signal
DOS	density of states
EQE	external quantum efficiency
FE	free exciton
FWHM	full width half maximum
FK	Franz–Keldysh
FKO	Franz–Keldysh oscillations
HH	heavy hole
IBSC	intermediate band solar cell
IR	infrared
LH	light hole
LO	longitudinal optical
MBE	molecular beam epitaxy
ML	monolayer
MOCVD	metal organic chemical vapor deposition
NTNU	Norwegian University of Science and Technology
OAP	off axis parabolic mirror
PL	photoluminescence
PLE	photoluminescence excitation
PR	photoreflectance
QW	quantum well
QD	quantum dot
SNR	signal to noise ratio
VB	valence band
WL	wetting layer

ROMAN SYMBOLS

A	real amplitude
B	polarization and transition strength
d	width, diamter
e	electron charge
E_0	energy bandgap at 0 K
E_g	energy bandgap
E_n	photon energy at the n_{th} extreme
E_q	energy subband
E_{inc}	incident electric field
E_{refl}	reflected electric field
$F(\eta)$	first kind of Airy function
f	focal length
$G(\eta)$	second kind of Airy function
$H(z)$	phenomenological broadening parameter
$H(\eta)$	unit step function
h	Planck constant
I_0	light intensity
J_{SC}	current density
$K(\omega)$	extinction coefficient
k	wavevector
m	critical point
$m*$	effective mass
$N(\omega)$	complex refractive index
n	refractive index
n_{th}	maximum or minimum oscillation
q	electron charge
R	Reflectance
r	distance
$r(\omega)$	reflectivity coefficient
s	distance from object to optical component
s'	distance from image to optical component
T	temperature
T_{QD}	quantum dot growth temperature
T_{SL}	spacer layer growth temperature
$u_k(r)$	perturbation, function of the periodicity of the lattice
V_{OC}	open circuit voltage

GREEK SYMBOLS

α	Seraphin coefficient
α_{abs}	absorption coefficient
α_j	polarizability
β	Seraphin coefficient
Γ	broadening parameter
ϵ	dielectric function
$\epsilon'(\omega)$	real part of dielectric function
$\epsilon''(\omega)$	imaginary part of dielectric function
$\theta(\omega)$	phase component of $r(\omega)$
κ	loss of light
λ_0	wavelength
$\mu_{\|\|}$	effective mass
ν	frequency
ξ	modulation, built–in electric field
$\rho(\omega)$	amplitude component
τ	lifetime
ϕ	phase factor
χ	arbitrary phase factor
$\psi(k,r)$	wavefunction, as the function of k and r
Ω	electro-optic frequency
ω	angular frequency

OTHER SYMBOLS

$\hbar$	reduced Planck constant or Dirac constant

MATHEMATICAL NOTATIONS

$e\xi a_0$	characteristic energy of the perturbation
$e\xi$	uniform field of force
$\Delta\epsilon_i$	change in dielectric field for imaginary part
$\Delta\epsilon_r$	change in dielectric field for real part
ΔR	change in R arised from the modulation, $R_{laserON} - R_{laserOFF}$
$\Delta R/R$	ratio of small reflectance change induced by modulation to reflectance
$\hbar\Omega$	electro-optic energy
$\hbar\omega$=$h\nu$	energy of photon

Chapter 1

Introduction

1.1 Background

Optical spectroscopy is employed to extract information from the semiconductor structure. Two of them which are being utilized in this study are modulation spectroscopy and PL. Modulation spectroscopy is a technique based on the changes of the reflectivity of a sample when a periodic perturbation is applied. Piezoreflectance, thermoreflectance and wavelength modulation are the examples of the modulation spectroscopy, which the perturbation source comes from applied stress, temperature and wavelength, respectively. They are belong to the first-derivative modulation spectroscopy technique. Modulation spectroscopy provides derivative-like spectrum related to the optical transitions in the semiconductor structure, while eliminates uninteresting background [1–5].

Modulation spectroscopy based on applied electric field is called electromodulation. Electromodulation is a well-known tool for studying various material issues in different semiconductor heterostructures, like quantum wires, quantum wells (QWs) and QDs. The basic idea of this technique is to measure the derivative of the reflectance spectrum with respect to modulating electric field. From a spectroscopic point of view, the result of electromodulation is particularly significant, because third-derivative lineshapes are characterized by the presence of strongly enhanced critical point structures and suppressed background effects [1–3, 5].

The modulation of the electric field can be achieved in two ways, and these are contact and contactless modes. The contact mode, also called electroreflectance, has a direct probe on the material either by Schottky barrier or semiconductor/electrolyte junction. This method is destructive for samples, therefore, contactless mode (contactless electroreflectance and PR) is more favoured [4].

Contactless electroreflectance has the same advantage as in PR: they are useful tool to study quantum structures, do not need special mounting on the sample or specific sample preparation, can be employed in-situ on wafer-sized material, perform in room-temperature and have large spectral range. Both of the techniques are able to produce sharp spectral features at photon energies corresponding to interband transitions. With an appropriate field working range, investigation to built-in electric field (Franz-Keldysh

(FK)) and Fermi-level position in semiconductor heterostructures are possible [2, 4, 6]. Determination towards energy bandgap and carrier concentration have been reported [7].

For PR measurement, the modulation of the electric field is caused by the photo-generated carriers created by a mechanically chopped laser (photon energy of the laser is usually larger than the band gap of the semiconductor). However, photo-excited electron-hole pairs can be trapped by surface states and in this way the surface band bending is modulated [4].

The drawback of using PR is the presence of the unwanted PL signal caused by the photo-generated carriers [2, 8]. Contactless electroreflectance does not produce PL signal and therefore investigation of weak optical transitions is made possible. The band bending modulation is probed deeper in the PR compared to contactless electroreflectance, hence generating higher signal intensity, resolution and sensitivity from the substrate. The screening effect in contactless electroreflectance is higher with respect to PR. Interference effects resulting oscillation features below energy bandgap of material in multi-layer structure are observed in the PR. In some cases, this observation could be useful to determine the thickness of the epilayer, but in most cases the presence of oscillation features complicates the analysis of PR spectrum [4]. Contactless electroreflectance spectroscopy does not generate additional carriers, therefore oscillation features are not produced in the contactless electroreflectance spectrum [8].

Compared to homostructure, heterostructure offers thinner active layer: the area where carriers and photons are confined; resulting in increasing of amplifier gain and reducing loss. It has become important material for high-speed and optoelectronic devices due to its nature as direct bandgap semiconductor. As the size of active layer becomes smaller than de Broglie wavelength, quantum effects determine the performance of the semiconductor. Techniques utilized to grow heterostructure materials are molecular-beam epitaxy (MBE), liquid-phase epitaxy and vapor-phase epitaxy [9]. Heterostructure material can be found in many applications around us, such as in solar cell. Solar cell produces electricity energy by photovoltaic effects when it is exposed to sunlight. There are five major issues influencing conventional solar cell (1st and 2nd generation) performance: thermalization loss, recombination loss, junction loss, contact loss and unabsorbed low energy photons [10].

The last issue is being addressed by the third generation solar cells, defined as intermediate band solar cell (IBSC). Utilizing intermediate band, it facilitates photon whose energy lower than bandgap of the material to excite electron from valence band (VB) to conduction band (CB). The cell with intermediate band is able to reach efficiency of 63.1% compared to 40.7% which belongs to the conventional single junction solar cell [11]. Formation of the intermediate band can be achieved by several ways, but most attention has been given to arrays of QDs.

Realizing the potential of the QD-IBSC, characterization using PR technique is conducted. PR measurement setup has been established in Norwegian University of Science and Technology (NTNU) equipped with Si and InGaAs detector. The InGaAs detector will help in the identification of the QDs transition in the near-infrared (IR) region. The likelihood of discovering interesting features in the wavelength extending from 300 nm to 1100 nm is accommodated with the Si detector. To support and complement PR result, preliminary PL measurement is executed.

1.2 Objectives

The purposes of this study are listed as follows:

1. Updating PR system, such as increasing flux and noise reduction,
2. Implementation of the mathematical models of the PR signal, in order to perform quantitative curve fitting of the recorded data based on a physical model,
3. Performing PR and analysis on the IBSC samples,
4. Performing preliminary PL and analysis on the IBSC samples.

1.3 Outlines

Following introduction in chapter 1, several key terms and physical concepts encountered in this study are presented in chapter 2. Chapter 3 deals with the addressed issue in the previous optical setup and the solution for it, together with the early test to verify the new PR setup. Mathematical models based on the theory given in chapter 2 will be implemented in chapter 4. The result of the PR and PL are shown in chapter 5, along with the interpretation of the spectra. In chapter 6, outlook with future setup possibilites are presented. The conclusions of this study are given in chapter 7.

Chapter 2

Theory

2.1 Confined Structure and Exciton

2.1.1 Quantum Well

QW is material composed of a thin layer of semiconductor whose energy bandgap is smaller than surrounding material and this thin layer is sandwiched between them, i.e. the structure with low energy bandgap in between of a structure with high energy bandgap [9]. The depth of the confining potential well for CB side is determined by the CB offset between them, and also similar for VB side. The structure and bandgap profile of QW is shown in figure 2.1.

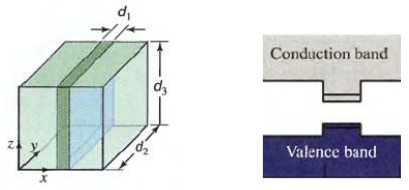

(a) The QW structure

(b) the bandgap profile

Figure 2.1: The QW structure and bandgap profile [9].

QW structure has carriers confined in x-direction and can only move freely in the y-z plane (figure 2.1a). QW structure is also called quasi two-dimensional (2D) system [12]. This system is different from the bulk semiconductor, in which the carriers are free to move in three dimensions (3D). The bandgap profile experiences discontinuity since it is composed of materials with different energy bandgap (figure 2.1b). Confinement in the x-direction forces electron and hole states occupation at certain discrete energies (quantization). The nature of energy quantization gives rise to subbands q_l formed in the QW, illustrated in figure 2.2.

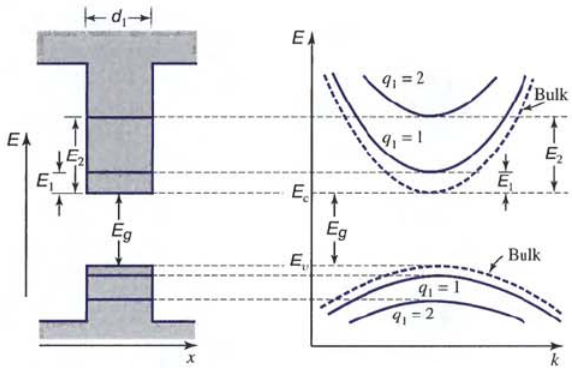

Figure 2.2: The subband of QW [9].

Energy transition of the electrons from the subband in the CB to subband in the VB obeys law of conservation of energy. Based on the time-independent Schrödinger equation, the general expression for the subband energy levels E_q of a effective mass m^* confined to a one-dimensional rectangular potential well with the width d is given as follows [9]:

$$E_q = \frac{\hbar^2 q^2 \pi^2}{2m^* d^2}, \quad q = 1, 2, 3, ... \tag{2.1}$$

The density of states (DOS) is different for the QW structure compared to a bulk semiconductor. DOS is described as the number of available states per unit volume between two closely adjacent energy. Because of the quasi 2D nature, the DOS becomes stair-formed, instead of smooth-curved line as in bulk semiconductor (figure 2.3). The important difference of DOS between QW and bulk semiconductor is that the QW DOS has finite value at the bottom of the ground state, while the bulk semiconductor DOS tends towards zero. As a result, QW structure will have kinetic energy even at T=0 K at the ground state [12]. DOS of CB and VB is highest in the lowermost and uppermost subband, respectively.

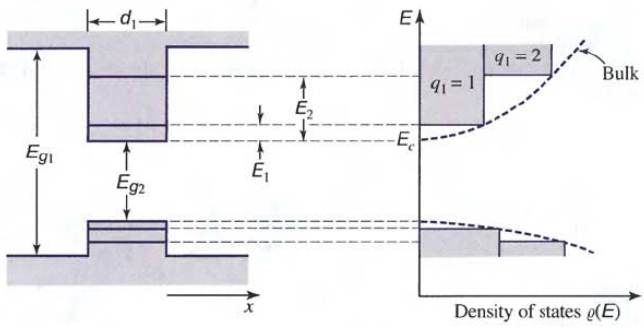

Figure 2.3: The DOS of QW (solid curve) and bulk semiconductor (dashed curve) [9].

2.1.2 Quantum Dot

In a QD structure, the carriers are confined in three-directions: x, y and z direction, and this confinement forms quasi zero-dimensional (0D) system. The QD structure is given in figure 2.4a. This structure is made of a low bandgap nanocrystal implanted in a large bandgap material. [10]. This confinement depicts a complete control of electron movement in semiconductor. QD energy is determined by the size of the dot and depth of the confining potential. As the dot size decreases, confinement energy as well as depth of the confining potential increase [10]. The DOS of the QD (figure 2.4b) is represented by a sequence of delta functions at the allowed energies [9].

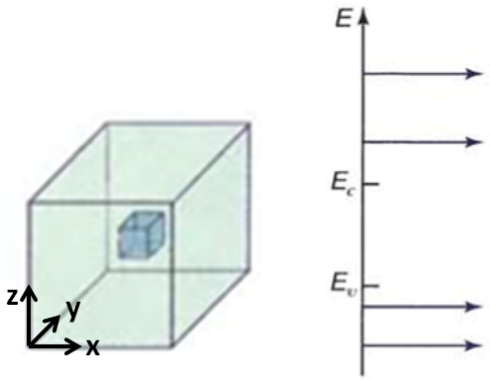

(a) The QD structure **(b)** The DOS of QD

Figure 2.4: The QD structure and DOS [9].

The physics of QD shares similarities with the behaviour of naturally occurring quantum systems in atomic physics, hence QD also called artificial atom [13]. Therefore, it is an artificially structured system that can be filled with electrons and required energy to add or remove a single electron from the dot is called charging energy (analogous to the ionization energy) [14]. The dot can be coupled via tunnel barriers, so that electrons can be exchanged [13]. Typically, QD is small regions defined in a semiconductor material with a size of order 10 nm [10].

Electronic properties in QD semiconductor influenced by confinement characteristics [13]. Its tunability deetermining the QD size leads to the characterization of energy bandgap. This is very advantageous due to QD flexibility in adapting its size for specific bandgap energy, without changing the material or the construction. To change the size of QD, tuning the duration and/or temperature of synthesis are done. The solar cell based on QD has been developed, called QD-IBSC making use of discrete nature of electron DOS in the nanostructure and the flexibility in tuning energy bandgap based on the requirement [15].

2.1.3 Exciton

Exciton is the bound of electron-hole pair in spatially closely located [12]. The bound of energy between them is governed by the coulomb interaction. Exciton usually exhibits in the structure which has photon energies lower compared to the energy gap of material and it is conveyed in the reflectance and absorption spectra. The characteristics of exciton are the ability to circulate through the crystal, transporting energy and electrically neutral. There are two types of excitons based on the separation of electron-hole compared to lattice constant and bound level: small and tightly bound (Frenkel) and large and weakly bound (Mott and Wannier). Figure 2.5 gives an brief illustration location of the exciton levels relative to CB and VB [16]. Exciton which is free to move in a crystal, called free exciton (FE). In a semiconductor, an exciton can be trapped in the impurity. This is called bound exciton (BE) and it has lower energy compared to the FE due to the binding energy to an impurity [17].

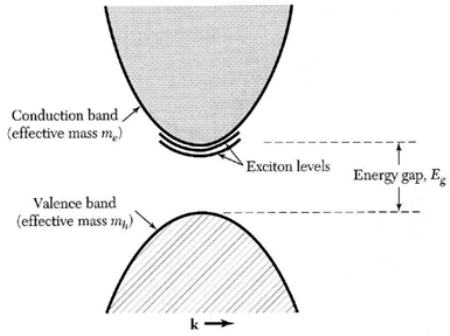

Figure 2.5: Exciton levels location relative to between CB and VB [16].

2.2 Heterojunctions, Photon Intaraction and Intermediate Band Solar Cell

2.2.1 Heterojunctions

This form of junction consists of two materials (p-type and n-type) with different energy bandgap, heavy donor doped (assuming that it has wider energy gap) in one side and acceptor doped in another side (assuming that it has narrower energy bandgap). There will be the same Fermi energy level (thermal equilibrium) in the two materials, and band bending takes place due to the pinned Fermi energy to the heavy donor doped and the potential of the acceptor doped is increased with respect to the potential of the heavy donor doped, as it is shown in figure 2.6. A notch potential is formed at the interface between this two materials, where the transferred electron will accumulate and form a two dimensional electron gas (2DEG). The notch potential formed in heterojunctions is the realization of the QW structure. 2DEG separates electrons from the donor impurities, giving faster time

response because of the higher mobility of electrons. High electron mobility transistors is based on this structure [12].

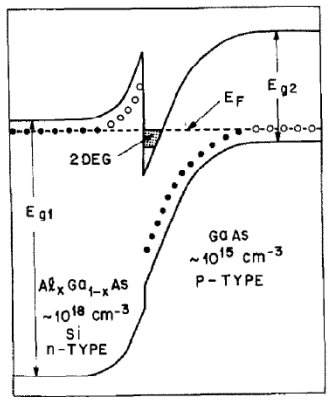

Figure 2.6: Heterojunctions energy band position at the thermal equilibrium [18].

2.2.2 Photon Interactions with Charge Carriers in Confined Structure

There are four type transitions of photon in confined structure, illustrated in figure 2.7 [9],

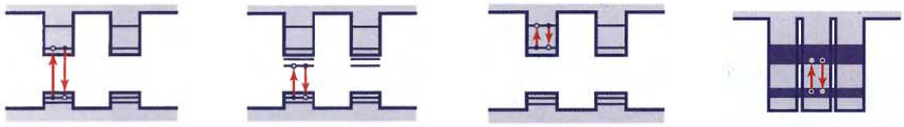

(a) Interband transitions

(b) Excitonic transitions

(c) Intraband transitions

(d) Miniband transitions

Figure 2.7: Type of transitions [9].

Interband transitions (figure 2.7a) show that emission and absorption of carriers happened between states in the VB and CB. This transition is common in bulk semiconductors. Excitonic transitions (figure 2.7b) occur when there is a carrier confinement in 2D, resulting an increment in the exciton binding energy. Excitonic transitions play an important role in multiple-QW electroabsorption modulators. Intersubband (intraband) transitions (figure 2.7c) conduct transition interaction within a single band. The examples of this transition are QW quantum cascade laser and QW infrared photodetector. Miniband transitions (figure 2.7d) triggered by a broadening of discrete multiple-QWs energy levels, developing minibands separated by a minigaps. Miniband transitions play a crucial role in the operation of superlattice quantum cascade laser. Together with intersubband transitions, it exhibit fast relaxation and large nonlinearities and therefore become suitable candidate for all-optical switching and demultiplexing.

2.2.3 Intermediate Band Solar Cell

One example of the heterojunctions semiconductor is IBSC. It is composed of the different p-n material energy bandgap (heterostructure) and has intermediate band, located between CB and VB (figure 2.8). Through intermediate band, electrons absorbing photons whose energy is lower than energy bandgap of material, can contribute to the additional photocurrents. Electrons will be excited from VB to intermediate band and from intermediate band to CB. While in conventional solar cell, energy required to excite electrons from VB to CB has to be higher than energy bandgap of material, limiting generated photocurrent. In order to make absorption processes possible, the intermediate band should be half-filled with electrons [19].

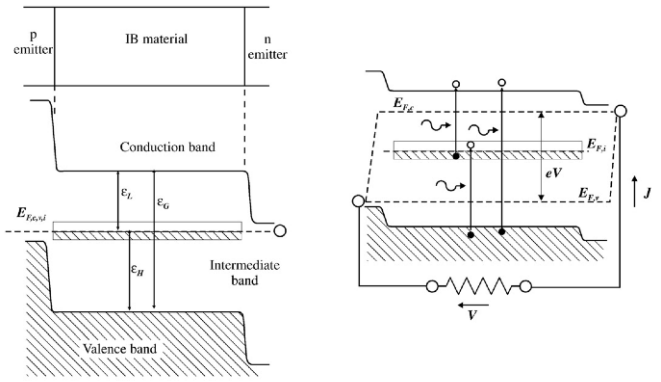

Figure 2.8: Basic structure of an IBSC with the simplified bandgap diagram in equilibrium (left) and simplified bandgap diagram under illumination and forward biased (right) [19].

2.3 Franz-Keldysh Effect

For several transparent materials subjected to applied external electric field (low-frequency), it gives rise to change of optical properties, such as refractive index. This is called electro-optic effect. In semiconductor, when electron in VB absorbs energy from light coming from external to the material (for example: laser), whose energy of the light larger than bandgap, the electron will be able to cross bandgap to the CB, leaving hole in the VB, therefore electron-hole pair created and the material becomes optically transparent. As the external electric field applied to semiconductor, it can reduce the bandgap of material. This is a phenomenon where optical properties changed by an electric field via absorption. The absorption triggers change of material from transparent to opaque. The occurance of change in absorption characteristics of a medium in applied electric field, called electroabsorption [9].

The bandgap of material is reduced when there is an external applied electric field (ON), explained by the existence of electron tunneling (figure 2.9a). Electron tunneling gives rise to extension of absorption edge (tails) into forbidden gap, i.e bandgap energy

becomes smaller $h\nu_2 < h\nu_1$. When there is no perturbation of applied external applied field (OFF), electroabsoprtion becomes absent from the material, i.e bandgap of material returns to normal. Change of bandgap energy is known as the FK effect and the effect itself resulting in shift of the absorption spectrum to smaller photon energy (figure 2.9b). The FK effect itself also triggers broadening, and ultimate disappearance of the exciton absorption peaks [9].

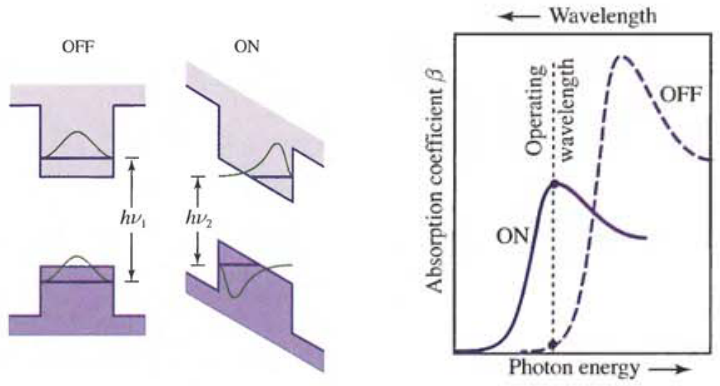

(a) Change of band from normal to bending

(b) Shifting of absorption spectrum to smaller photon energy

Figure 2.9: The FK effect [9].

In p-n junction semiconductor, modulation by the formation of the electron-hole pair in the energy band structure will lead to the reduced built-in electric field. Flowing of the electrons and holes in the opposite direction due to the drift explains this reduction: electrons will be swept away to the n-side while holes drift to the p-side, neutralizing trapped charge in surface state, thus reducing built-in electric field, as shown figure 2.10.

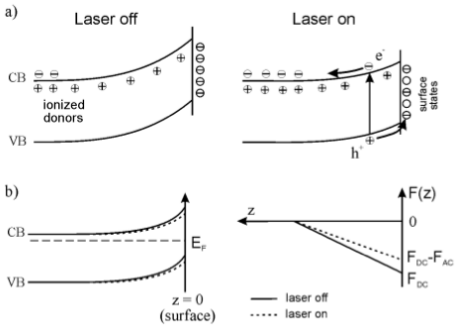

Figure 2.10: FK effect on p-n junction semiconductor (a) in the space charge region, when the laser is ON and OFF (b)The overall behaviour of the band bending with (ON) and without (OFF) modulation (left picture) and also the electric field with (ON) and without (OFF) modulation (right picture) [20]

2.4 Bloch Theorem

The solution of the Schrödinger equation for a periodic potential:

$$\psi(k, r) = u_k(r)e^{ikr} \tag{2.2}$$

Bloch theorem describes interaction between plane wave e^{ikr} with perturbation $u_k(r)$, which is a function of the lattice periodicity. There are two types of perturbation: the first one is the perturbation which maintains periodicity, i.e. translational symmetry is maintained and having good quantum number within a reciprocal lattive vector, so that optical transitions continue to be vertical as shown in upper part of figure 2.11. The examples of this perturbation are found in piezoreflectance, thermoreflectance and wavelength modulation. This changes appear directly as small shifts in energy bandgap and it can be approximated with first-derivative lineshapes [1].

The second perturbation has characteristics opposing the first one. The electric field, which is a modulation parameter, accelerates electron and the quantum number is not preserved as a good in terms of field directions within a reciprocal lattice vector. The lattice periodicity is destroyed due to the acting of electron acceleration leading to the absent of the translational symmetry. This perturbation yields to the mixing of Bloch functions of the unperturbed crystal, causing spreading of vertical transitions over a finite range of initial and final momenta, as shown in lower part of figure 2.11. As there is a spreading, meaning that the resolution of this difference can be approximated only by higher derivatives, i.e. third-derivative lineshapes. The example of this perturbation is electromodulation [1].

2.5 Photoreflectance

The basic of electromodulation is perturbation of the electric field triggering alteration of the dielectric property of the unperturbed system. The source of the modulation in PR is mechanically chopped laser. The PR technique is based on the alteration of dielectric function due to the external modulation, and hence a change in the reflectance is observed. Modulation in PR is caused by photo-excited electron-hole pairs created by pump source chopped at a given frequency, which gives photon energy larger than the bandgap of the semiconductor. The modulation makes a bending of the energy bands at the semiconductor surface and/or interface, as shown in figure 2.10.

PR exhibits third-derivative lineshapes, which show information about the material [1]. It is characterized by the presence of strongly enhanced critical point structures and suppresses background effects. The information provided by the PR are lifetime broadening (widths of third-derivative critical point structures), resolved degenerate critical points (well localized in energy), accurate actual energy band structure approximation in the vicinity of critical points [1], uniformity, homogeneity, strains, doping concentrations, electro-optic energy and built-in electric field [4, 21].

The periodic lineshape of PR spectrum varies with different thickness of the front barrier layer. It proofs that PR lineshapes are related to the interference terms. The interference terms are modulated by the internal electric field and contribute to the observed lineshapes [6].

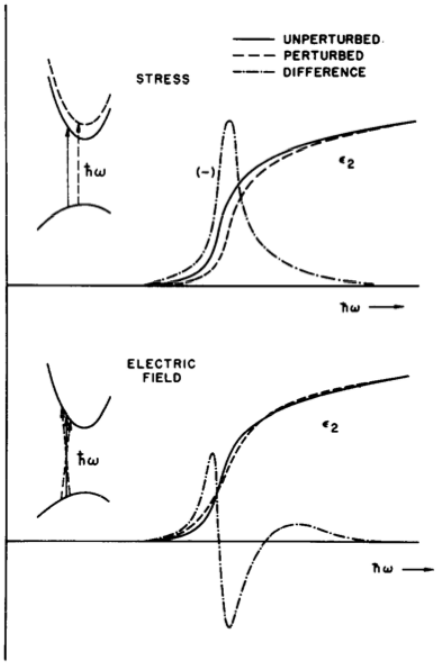

Figure 2.11: Different response of the structure to the two different perturbations: first derivative modulation where lattice periodicity is preserved; on the left showing one zero crossing of optical transition in the energy band structure (top) and electric field modulation where lattice periodicity is not preserved; on the left showing two zero crossings of optical transition in the energy band structure (bottom) [1].

The relative change of the reflectivity $\Delta R/R$ measured in the experiment of PR is expressed as the ratio of a small reflectance change induced by modulation light ΔR to the reflectance R [20],

$$\frac{\Delta R}{R} = \frac{R_{on} - R_{off}}{R_{off}} \tag{2.3}$$

There are two well-known coefficients in the PR expression, called Seraphin coefficients (α and β) and they are directly related to the lineshapes of the modulation reflectance [22],

$$\frac{\Delta R}{R} = \alpha\Delta\epsilon_r + \beta\Delta\epsilon_i \qquad \alpha = \frac{1}{R}\frac{dR}{d\epsilon_r} \quad \beta = \frac{1}{R}\frac{dR}{d\epsilon_i} \tag{2.4}$$

Reflectance R is the function of angular frequency ω. ΔR is the difference between reflectance with the modulation ξ and the reflectance without modulation ($\xi = 0$), i.e $\Delta R = R(\omega, \xi) - R(\omega, \xi = 0)$. Change in dielectric function for real $\Delta\epsilon_r$ and imaginary part $\Delta\epsilon_i$ are the function of modulation parameter ξ. It is important to keep in mind that $\Delta\epsilon_r$ and $\Delta\epsilon_i$ are related by Kramers-Kronig inversion [2, 22]. If the measurement is done in the vicinity area of fundamental gap, β ∼0, then the PR expression becomes: $\frac{\Delta R}{R} = \alpha\Delta\epsilon_r$ [2].

PR signal consists of two parts, one is the a.c. modulation signal $I_0(\lambda)\Delta R(\lambda)$ produced by modulation source (e.g. chopped laser) and the other is the d.c. reflectance signal $I_0(\lambda)R(\lambda)$ from probe beam. One advantage of the PR spectroscopy is that, there is no necessity to collect every photon reflected from the sample in the detector (intensity of the probe beam I_0). If there is a loss light, i.e $\kappa < 1$,

$$\frac{\kappa I_0 \Delta R}{\kappa I_0 R} = \frac{\Delta R}{R} \tag{2.5}$$

Equation 2.5 tells us that the PR signal is independent to the intensity of probe beam I_0 and loss of light. The signal of the PR spectrum will not be affected too much with the amplitude of the I_0 and κ. The importance of these two values come in relation with the goodness of signal to noise ratio (SNR) [2, 4].

The only drawback of PR is the spurious modulated background signal reaching the detector due to luminescence from the sample and/or scattered light from pump source. This is triggered by trapped photo-generated carriers in surface states. To reduce scattered light from the pump source, suitable long-pass filter is needed or using crossed-polarizer in the front of detector. Another way to solve this issue is by using double monochromator, tunable dye laser probe beam, sweeping PR, differential PR, double a.c. modulation or an offset technique [2, 4]. Contactless elecroreflectance is able to handle spurious background signal.

Plasma-induced damage of Si-substrate in the atmosphere and low-dimensional GaAs are examples of the structure investigation using PR. It is proven that this technique is extremely useful compared to e.g. Raman spectroscopy [21, 23]. With the response to change of surface potential, PR technique can detect defects in the vicinity of the surface of the material. The change of surface potential by modulation decrases as the PR signal decreases due to localized or defect level that changes space charge density [23].

Modulation in PR affects both interband and intraband mechanisms [1]. Perturbation theory in PR implies the existence of two energies per mechanism: the characteristic energy of the perturbation and a characteristic energy of the system. For interband mechanisms, a potential drop across the unit cell $e\xi a_0$ represents the characteristic energy of the perturbation and the energy separation between the pair of bands E_g is a characteristic energy of the system. Intraband mechanism is characterized by the electro-optic energy $\hbar\Omega$ as the perturbation characteristic energy and broadening parameter Γ plays role in system characteristic energy. Broadening parameter Γ is related to the critical point energy, and has connection with lifetime τ, defined by $\tau \backsim \hbar/(2\Gamma)$ [1]. Broadening parameter Γ gives rise to the energy uncertainty, provided by dislocations, impurities, alloy scattering and phonon absorption processes [24]. The electro-optic energy $\hbar\Omega$ is expressed by,

$$\hbar\Omega = \left[\frac{e^2\xi^2\hbar^2}{2\mu_{||}}\right]^{1/3} \tag{2.6}$$

where e is electron charge, which is typically 1.6×10^{-19} C, ξ is the electric field, $\hbar$ is the Planck constant with the value of 6.63×10^{-34} m^2 kg s^{-1} and $\mu_{||}$ is the effective mass. Electro-optic energy is obtained in the quantum mechanical solution of a particle of effective mass $\mu_{||}$, which is accelerated in a uniform field of force, $e\xi$ [1].

The different relationship between relative magnitudes of the pairs of characteristic energies lead naturally to three ranges of PR [1]:

2.5.1 Low-field regime

This regime is characterized by $e\xi a_0 \ll E_g$ and $|\hbar\Omega| \leqslant \Gamma/3$. . Interband mechanism can be neglected in this regime due to the small contribution of perturbation compared to the energy bandgap of the material substrate, resulting the same band structure [1]. Due to the modulation of the electric field, the perturbation destroys the translational symmetry of the crystal and it can be approached by third-derivative spectroscopy [20]. The reason of the PR technique in producing derivative-like spectrum is located on the capability to reject all contributions to reflectance except those originating from high symmetry points in the Brillouin zone [25]. The fitting relation to the lineshape of PR spectrum can be expressed by [26–30],

$$\frac{\Delta R}{R} = Re\left[Ae^{i\phi}(E - E_g + i\Gamma)^{-m}\right] \tag{2.7}$$

where A is a real amplitude, ϕ is the phase factor and m is a parameter that depends on the type of critical point and order of the derivative: m=3 corresponds to the third derivative of a two-dimensional critical point, m=2.5 defined as third derivative of a three-dimensional critical point and m=2 is the first derivative of Lorentzian function. Bound states such as excitons or confined states of a QW and QD, the fitting procedure is approached using first derivative of the Lorentzian function, m=2. A typical PR spectrum with the fitting plot is shown in figure 2.12.

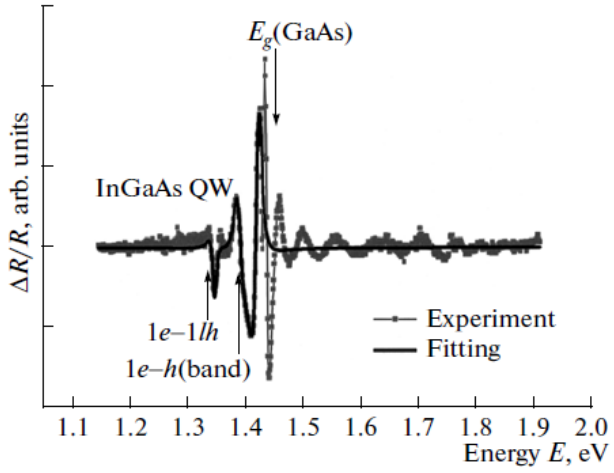

Figure 2.12: Regular PR spectrum (bold line) along with the fitting [29].

2.5.2 Intermediate-field regime

This regime is indicated with $e\xi a_0 \ll E_g$ and $|\hbar\Omega| \gtrsim \Gamma$. Similar with the low-field regime, this regime conducts unchanged band structure due to the small value of perturbation in interband mechanism. What makes this regime different from low-field regime is the existance of the subsidiary oscillations, called FKO, in which possess exponential absorption edge behaviour. Satisfying these conditions, the dielectric function can exhibit FKO. The expression of the $\Delta R/R$ relating with the FKO is [5, 31],

$$\frac{\Delta R}{R} \propto \frac{1}{E^2(E-E_g)} exp\left[-2(E-E_g)^{1/2}\frac{\Gamma}{(\hbar\Omega)^{3/2}}\right] \cos\left[\frac{4(E-E_g)^{3/2}}{3(\hbar\Omega)^{3/2}} + \chi\right] \quad (2.8)$$

χ is arbitrary phase factor. The attribute of FKO are represented clearly in the equation 2.8, oscillation terms are defined by cos term and the oscillations are damped with the term exp. Equation 2.8 determines the position of an n-th extreme in the FKO given by [20],

$$n\pi = \frac{4}{3}\left(\frac{E_n - E_g}{\hbar\Omega}\right)^{3/2} + \chi \quad (2.9)$$

E_n is the photon energy of the n_{th} extreme oscillations. The importance of this equation lead to the generated figure with the relation between $\frac{4}{3\pi}(E-E_g)^{3/2}$ and the index number n, leading to a straight line with the slope $\hbar\Omega^{3/2}$. This finding, called linearity plot, will reveal the value of built-in electric field ξ. To make this more clear, see the FKO and the linearity plot in figure 2.13.

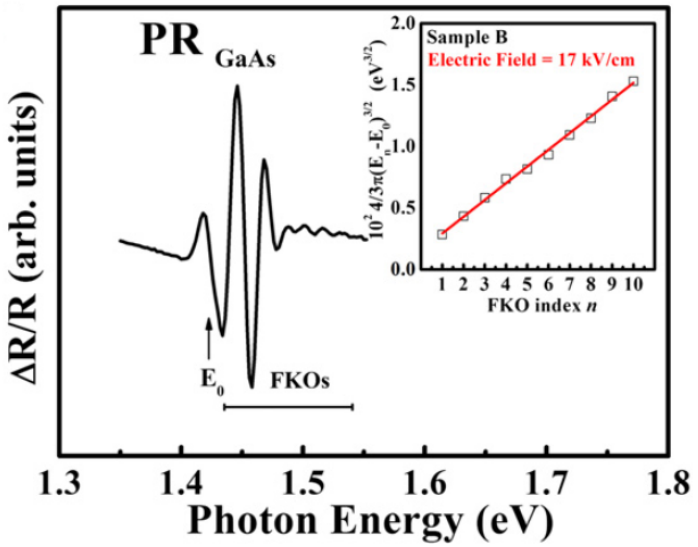

Figure 2.13: The PR spectrum shows FKO above the band edge of gaAs with the inset showing linearity plot, $\frac{4}{3\pi}(E-E_g)^{3/2}$ with the index number n [30].

The behaviour of the PR in the intermediate-field regime is able to be observed using Airy functions. Equation 2.4 relates Seraphin coefficients and change in dielectric constant. Modulation gives rise to change in the dielectric constant of real and imaginary parts near critical points. Both part of dielectric constant change is resolved by involving Airy function evaluation: $\Delta\epsilon_r = \frac{B\Omega^{1/2}}{\omega^2}G(\eta)$ and $\Delta\epsilon_i = \frac{B\Omega^{1/2}}{\omega^2}F(\eta)$ for real and imaginary parts, respectively [7]. There are two electro-optic function, the first kind $F(\eta)$ and the second kind $G(\eta)$ which have expression as follow [7, 32, 33],

$$F(\eta) = C\pi[Ai'^2(\eta) - \eta Ai^2(\eta)] - (-\eta)^{1/2}H(-\eta) \qquad \eta = \frac{E_g - E}{\hbar\Omega} \tag{2.10}$$

$$G(\eta) = C\pi[Ai'(\eta)Bi'(\eta) - \eta Ai(\eta)Bi(\eta)] + \eta^{1/2}H(\eta) \tag{2.11}$$

where C is constant, $Ai(\eta)$, $Bi(\eta)$, $Ai'(\eta)$ and $Bi'(\eta)$ are Airy functions and their derivatives, and $H(\eta)$ is the unit step function. Electro-optic function of the first kind $F(\eta)$ is depicted in the figure 2.14.

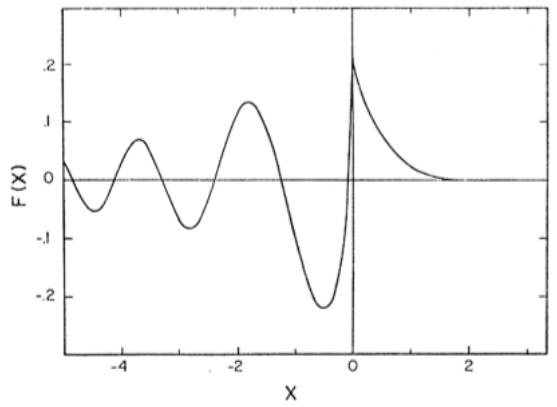

Figure 2.14: The electro-optic function of the first kind $F(\eta)$ [32].

2.5.3 High-field regime

This regime is given by $e\xi a_0 \sim E_g$ and $|\hbar\Omega| \gtrsim \Gamma$. This regime accomodates the breakdown of selection rules, Stark shifts which causes alteration of energy bands, and first-derivative of PR spectra. Due to the same amount of energy between perturbation and system, the band structure in this regime modified. Contribution at this field is dominated by intraband mechanism and the interesting point is located in the point of degeneracy [1].

2.6 Reflection and Dielectric Properties

Dielectric constant determines the reflectance of the investigated structure. As the electric field modulation applied to the structure, dielectric constant will altered, followed by the

change in the reflectance structure. It is affected by the thickness and refractive index of the cap layer, barriers and the QW width [6].

The reflection phenomenon from heterojunction semiconductor is not the same as the reflection from single material, because there will be several reflections occured in the heterojunction, depicted in figure 2.15. As a note, the higher-order reflection can be neglected due to its small value of the intensity [6].

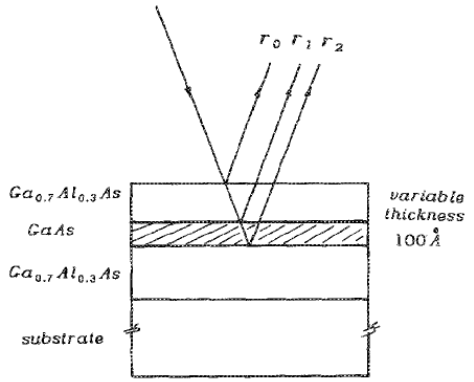

Figure 2.15: Reflected waves from single QW structure, r_0, r_1, r_2, and each layer has different thickness. [6].

The total reflectance from figure 2.15 is the sum of the reflectance from each interface, and also interference between all of them. In addition, the effect of interference between reflected waves at the interface of material contributes to the reflectance spectrum of heterostructure material [22].

Assuming that the pump source comes at the normal incidence expressed by [16],

$$\frac{E(refl)}{E(inc)} = r(\omega) \equiv \rho(\omega)e^{i\theta(\omega)} = \frac{n + iK - 1}{n + iK + 1} \tag{2.12}$$

The reflectivity coefficient $r(\omega)$ is a complex function defined at the crystal surface as the ratio of the reflected electric field $E(refl)$ to the incident electric field $E(inc)$. $\rho(\omega)$ is the amplitude component, while $\theta(\omega)$ is the phase component of the $r(\omega)$. Other variables are the refractive index $n(\omega)$ and the extinction coefficient $K(\omega)$. The reflectance R is the ratio between reflected intensity to the incident intensity shown by,

$$R = \frac{E^*(refl)E(refl)}{E^*(inc)E(inc)} = r^*r = \rho^2 \tag{2.13}$$

By definition, $n(\omega)$ and $K(\omega)$ are related to the dielectric function $\epsilon(\omega)$, which is also equal to complex refractive index $N(\omega)$ by,

$$\sqrt{\epsilon(\omega)} \equiv n(\omega) + iK(\omega) \equiv N(\omega) \tag{2.14}$$

The value of the dielectric constant ϵ consists of real part ϵ_r and imaginary part ϵ_i,

$$\epsilon(\omega) = \epsilon_r(\omega) + i\epsilon_i(\omega)$$

with the value of real and imaginary part as follows,

$$\epsilon_r(\omega) = n^2 - K^2 \qquad \epsilon_i(\omega) = 2nK. \tag{2.15}$$

The relationship between real and imaginary part of dielectric function are expressed by Kramers-Kronig relations. Using this relation will determine the phase $\theta(\omega)$ as well as imaginary part of the dielectric function $\epsilon''(\omega)$.

For the probe beam illuminating the sample in two different interfaces (figure 2.15), it comes with the angle of incidence correlating two different refractive index material, therefore the Fresnel equation used [9],

$$r_{TE} = \frac{n_0 \cos\theta_0 - n_1 \cos\theta_1}{n_0 \cos\theta_0 + n_1 \cos\theta_1} \tag{2.16}$$

$$r_{TM} = \frac{n_0 \sec\theta_0 - n_1 \sec\theta_1}{n_0 \sec\theta_0 + n_1 \sec\theta_1} = \frac{n_1 \cos\theta_0 - n_0 \cos\theta_1}{n_1 \cos\theta_0 + n_0 \cos\theta_1} \tag{2.17}$$

Since the materials in this study are concentrated on the substrate GaAs, QW formed by $Al_{0.8}Ga_{0.2}As$ or $Al_{0.3}Ga_{0.7}As$ and QDs established by InAs, therefore the result of the reflectance and dielectric function for these materials are required to be understood.

2.6.1 Reflectance and dielectric function of GaAs

Several researches [34–36] have been conducted in investigating the reflectance and dielectric function of GaAs (at normal incident), which are depicted in the figure 2.16a and figure 2.16b, respectively.

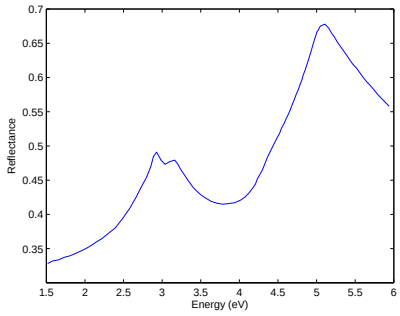

(a) Reflectance of GaAs.

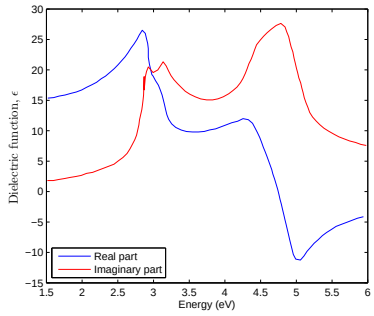

(b) Dielectric function of GaAs.

Figure 2.16: Reflectance and dielectric function of GaAs [36].

2.6.2 Reflectance and dielectric function of $Al_{0.8}Ga_{0.2}As$ and $Al_{0.3}Ga_{0.7}As$

In the case of the $Al_{0.8}Ga_{0.2}As$ and $Al_{0.3}Ga_{0.7}As$, the reflectance and dielectric function (at normal incident) [37] are depicted in the figure 2.17a and figure 2.17b, respectively.

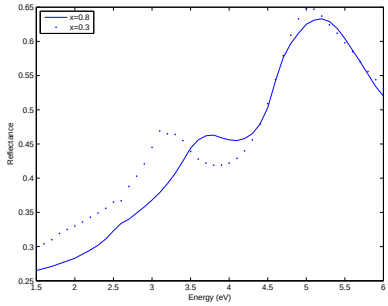

(a) Reflectance of $Al_xGa_{1-x}As$, x=0.3 and x=0.8.

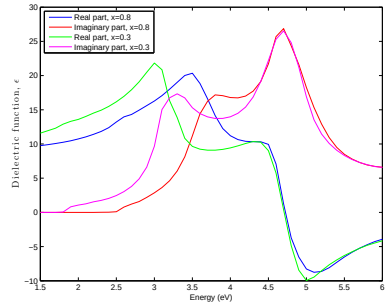

(b) Dielectric function of $Al_xGa_{1-x}As$, x=0.3 and x=0.8.

Figure 2.17: Reflectance and dielectric function of $Al_xGa_{1-x}As$ with x=0.8 and x=0.3 [37].

2.6.3 Reflectance and dielectric function of InAs

Result at normal incident for the reflectance and dielectric function of InAs [34, 36, 38, 39] are shown in figure 2.18a and figure 2.18b, respectively.

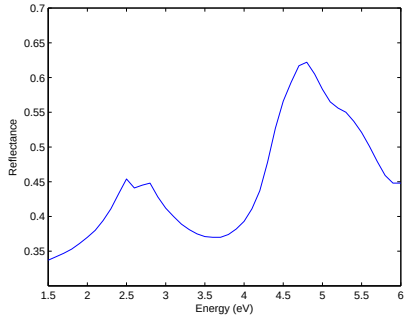

(a) Reflectance of InAs.

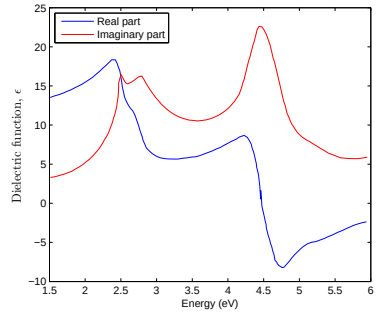

(b) Dielectric function of InAs.

Figure 2.18: Reflectance and dielectric function of InAs [36].

Chapter 3

Photoreflectance Optical Setup and Early Test

3.1 Previous Setup

The PR setup in applied physics group at NTNU has been developed by Hofstad [40]. In this study, the development will start from the last point of Hofstad's work, where he developed the PR setup shown in figure 3.1 along with the corresponding components listed in table 3.1. Noted that detector box, lock-in amplifier, computer and various power supplies and controllers, as well as the goniometer arm cover are not included in the figure 3.1.

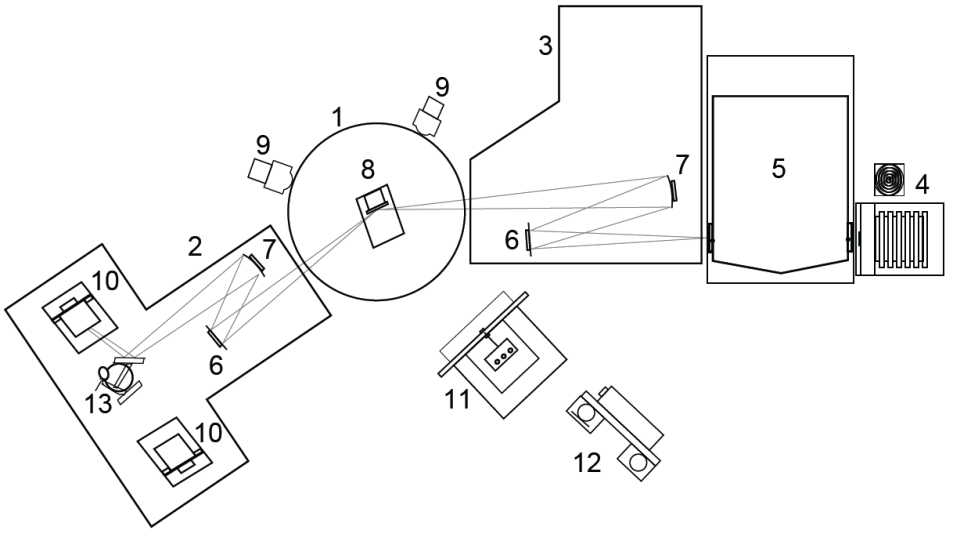

Figure 3.1: Schematic diagram of the PR setup developed by Hofstad [40].

Table 3.1: The components making up the PR setup, listed by numbers shown in figure 3.1 [40].

Number in figure	Corresponding component
1	Goniometer sample holder disc
2	Goniometer rotatable arm with light proof cover
3	Optical plate fixed to the goniometer
4	Light source with cooling fan
5	Monochromator
6	Flat mirrors, diameter of 1 inch
7	Concave mirrors, focal length of 25 cm, diameter 1 inch
8	Sample holder, vacuum operated
9	Stepper motors with gear systems
10	Detectors (Si and InGaAs)
11	Optical chopper
12	Laser
13	Motorized mirror arrangement

The components listed in table 3.1 have been explained in detail by Hofstad [40]. The light source of quartz tungsten halogen lamp is used as a probing to the sample. The light is dispersed by the monochromator. The optical pathways of the monochromatic light from the output of monochromator to the detector are provided by flat mirrors and concave mirrors. The monochromatic light will be focused on the sample surface by the concave mirror. Reflectance of monochromatic light from the sample surface down to the selected detector, either Si or InGaAs detector, is directed by flat mirrors and concave mirrors. Goniometer acts as rotating table, controlling the angle of the incident light. The reflection intensity from the sample surface is the DC signal. Excitation source comes from He-Ne laser, modulated by chopper before reaching the sample surface, and this modulation intensity is the AC signal, whose the signal with the frequency given by the chopper is locked by the lock-in amplifier. The physical concept of PR spectroscopy is alteration of material bandgap as it is exposed by the modulated excitation source, leading to the small change in reflection and this small change in reflection is compared to the reflection. The concept of the PR has been explained in chapter 2. Summary of the several components explained by Hofstad will be presented in the following section.

3.1.1 Components

3.1.1.1 Light source

The light source utilized in the setup is a 250 W quartz tungsten halogen lamp. To ensure that it works properly in a long period of measurement (usually 2-3 hours per measurement), a 80 mm fan is placed on top of the lamp to cool it. The spectrum of the lamp is given in figure 3.2 [41]

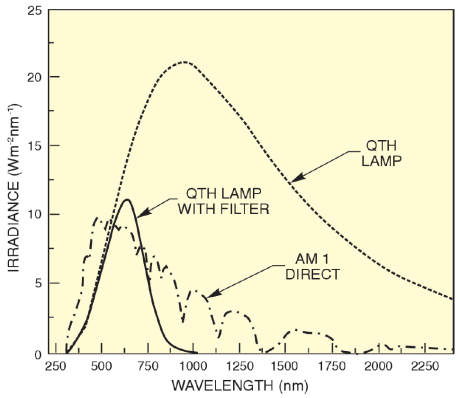

Figure 3.2: Typical spectrum of a quartz tungsten halogen lamp [41].

3.1.1.2 Monochromator

The monochromator disperses polychromatic light and passes only very narrow band of wavelength (monochromatic) in the output. Monochromator employed in this work is Bentham TM300V, which is a Czerny-Turner monochromator type. The diagram of this monochromator is depicted in figure 3.3. The slit is placed at the effective focus of a concave mirror so that the light from the slit reflected from the mirror is collimated. The collimated light is diffracted from the grating and then is directed toward another concave mirror. The collimated light which is refocused by the concave mirror, now dispersed on the exit slit. A rotation of the dispersing element determines band of colors relative to the exit slit. The range of colors leaving the exit slit is a function of width of the slits. Therefore, it is important to have exit slit as narrow as possible, in order to have high spectral resolution.

Bentham TM300V has a wavelength ranging from 250 nm to 2500 nm. It has three different gratings, listed in the table 3.2. High-pass optical filters of at least half the wavelength supposes to be let through are installed in order to stop higher diffraction orders at a given wavelength which will pollute higher wavelengths. The installed filter wheels are indexed in table 3.3. Both slit have adjustable width configured with a micrometer screw with a resolution of 10 μm.

Table 3.2: Grating installed in the TM300V monochromator [42].

Grating (l/mm)	Recommended wavelengths (nm)	Peak efficiency (nm)
1200	100-250	250
1200	250-1200	500
600	800-2500	1600

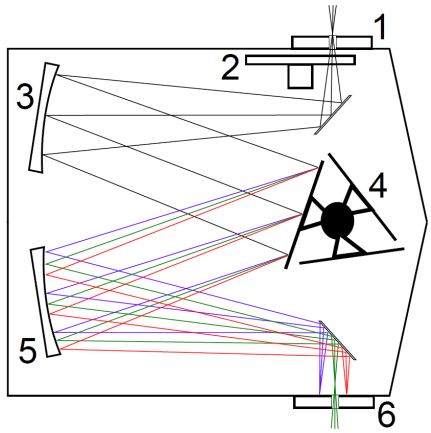

Figure 3.3: The Bentham TM300V monochromator. 1: Entrance slit, 2: Filter wheel, 3: Collimating mirror, 4: Grating wheel, 5: Focusing mirror, 6: Exit slit. Black line represent white light and in this figure, the monochromator is set to let the green light through [40].

Table 3.3: Filters installed in the TM300V monochromator. *OS* stands for Order Sorting, designed to stop higher diffraction orders and the numbers indicate which wavelength the filters block the light. [42].

Filter position	Filter
1	No filter
2	OS400
3	OS700
4	OS1250
5	OS2000
6	Shutter

3.1.1.3 Laser and chopper

The laser belongs to the solid-state diode laser with a wavelength of 532 nm and the output of 50 mW. With this wavelength, the given photon energy of laser is 2.33 eV. Since we do not need the output power of 50 mW, due to the reason of low-field limit on the PR lineshape, the variable neutral density filter is placed in front of the laser. The final output then becomes around 5 mW. Modulation introduced by the chopper, since it supplies lock-in amplifier with a reference signal, being the same frequency as the modulation. The chopper operates constantly at 293 Hz.

3.1.1.4 Si and InGaAs detector

Si detector ranges between 300 nm up to 1100 nm (see figure 3.4a), while the InGaAs detector (with amplification) extends from 800 nm to 1700 nm (see figure 3.4b). Both detectors produce output between 0-10 V.

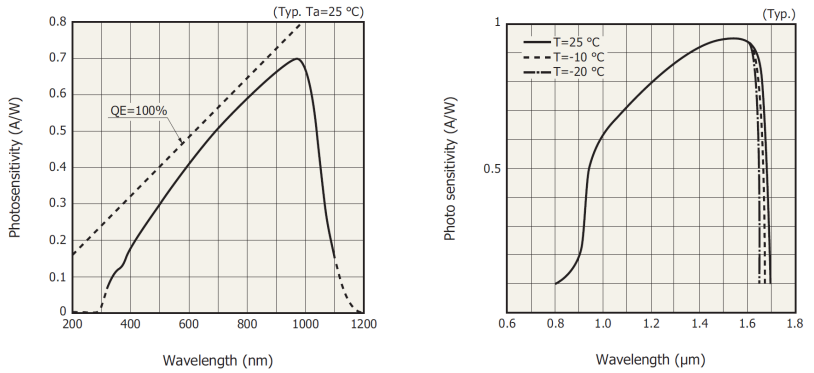

(a) The spectral response of the Si detector [43].

(b) The spectral response of the InGaAs detector [44].

Figure 3.4: Si and InGaAs detector spectral response.

3.1.1.5 Flat mirror, concave mirror and filter

Two flat mirrors and two concave mirrors with a focal length of 25 cm are used in this measurement. All of them have diameter of 1 inch (2.54 cm). Mirrors are preferred than lens because of lens performs much lower reflectivity in the near-IR range. The mirrors are positioned in such way that the distance from exit slit to concave mirror is the same as the distance between concave mirror to sample ($s = s'$). This placement is considered to produce one-to-one image and the focal length f of 25 cm can be used in here [40], using equation $\frac{1}{s} + \frac{1}{s'} = \frac{1}{f}$. Based on this judgement, the distance s is 50 cm, since $s = s'$ leads to the $2/s$ in the left side, while $f = 25$ cm in the right side. There is high probability of diffusively reflected laser beam from the sample to the surrounding, the long-pass filter (with the cut-off wavelength in the band of 520-550 nm) is placed deliberately in front of the detector.

3.1.2 Loss of light

.

Degradation of light intensity was identified by Hofstad in the PR setup [40]. This is occured in the process of guiding light from the exit slit of the monochromator to the sample and from sample to the detector. Hofstad addressed this issue caused by the angle of transmitted monochromatic light which was diverging too much, exceeding the surface area of the optical components yielding to the inability to receive amount of light from the original source. This problem limits the optical performance of the setup [40]. Hofstad suggested utilization of larger mirrors, but then realized that the spot size in the sample will get bigger. Choosing pinhole combined with the larger mirrors would also wasting gained light, even it reduces spot size. The inevitable factor which makes this issue emerged is because of the characteristic of the light source itself. In reality, the monochromatic light transmitted from the exit slit of monochromator is not point source, but line source. With the F-number of the Bentham TM300V of 4.1 [42], this number is equal to the acceptance

cone of light in front of the entrance slit of 14°. Outside this angle, the light becomes useless. In another word, the higher the F-number value indicates narrower acceptance cone. The finding shows a fantastic number of degradation of light reaching the sample: 99.3%! [40] With the distance from the exit slit to the first concave mirror, which was around 50 cm, the diverging angle from monochromator was many times larger than the largest acceptance angle of the mirror system (1.46°). In another word, the setup had many flaws. This degradation was not included with other loss, which is happened in each mirror due to the absorption.

3.2 Improved Setup

Loss of light intensity will become main focus to be solved in this setup. Due to the degradation of light intensity reaching sample and detector, opening more width of exit slit will become fastest way to solve this issue. By doing this, a new problem will be encountered: the band of wavelength will become wider than before, and has lower resolution. In finding the new optical setup, together with what kind of optical components should be replaced and added, a simulation software called Light Tools is being used.

Loss of light in the previous setup has been modeled, depicted in the figure 3.5

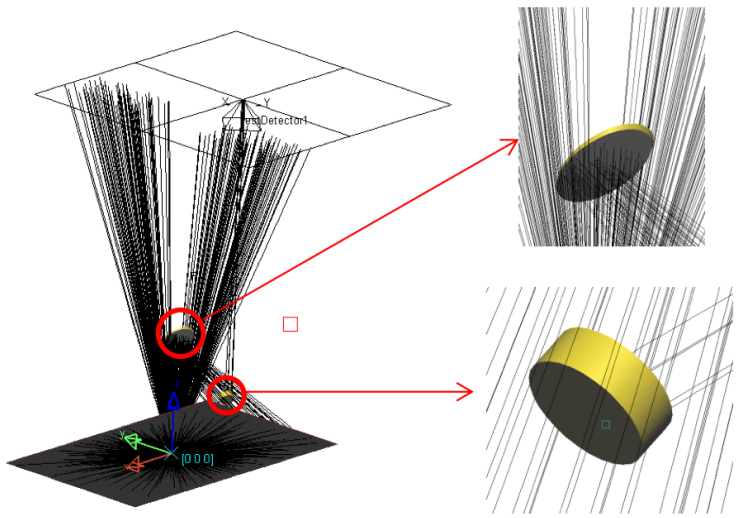

Figure 3.5: The propagation light rays from exit slit of monochromator (left). The light diverges so much, only small part of light captured by mirror (top right) and reflected into concave mirror (bottom right). Previous setup suffers lot of light intensity degradation.

Solution for this problems approached with the introduction of the off-axis parabolic mirror (OAP) 90°, placed right after the exit slit of the monochromator. Theoretically, divergence light which satisfies spesific distance from the OAP 90°, will be reflected with the light being collimated. The result of the simulation work shows the result given in figure 3.6,

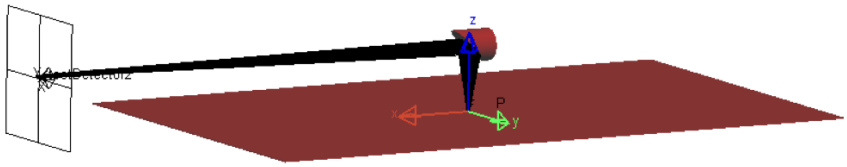

Figure 3.6: Introduction of OAP 90° forces divergence light to be reflected with the light being collimated.

By virtue of this simulation result, the old setup will be modified by introducing OAP 90°. This is a good start to properly solve the divergence of light after the exit slit of the monochromator. Later on, several new optical components are brought in the modified PR optical setup.

There are some data about the spot size measurement of probe light and pump beam. Maintaining spot size from probe beam to be equal with the spot size from pump beam is the objective of this work. Shay mentioned in his research, the spot size of the monochromatic light was 10 mm x 1.0 mm, so the area was 10 mm^2 [45]. Estrera et al. found the spot size of the pump and probe beam was 2 mm in diameter [7], so the area of the circle was 3.14 mm^2. Estrera et al. and Cánovas et al. used lens to focus probe light into the sample [7, 46]. As a consequence, a good focus obtained in the sample, but introducing lens can bring another problem: chromatic abberations, and this happened at specific wavelength. This abberations can introduce errors to the measurement. Also, lens is not used in order to avoid low reflectance signal from the sample in near-IR region. Modelling will be conducted in the first half-way of the setup (from the exit slit of monochromator until sample) since loss of light mainly occured at the first place in this part. Due to this reason, no major modification takes place in the second part of the setup meaning that no change in optical component, only in position. Managing light-guiding continuously down to the sample with minimizing lost of light intensity in the first part, will lead to the high probability of success rate in sending light from sample down to the detector.

In attempt to do this, the proposed optical components being employed in the new setup are explained as follows,

3.2.1 Components

3.2.1.1 Light source, monochromator, laser, chopper, detector, filter

No change being made in this part, as they are satisfying the need of the PR setup.

3.2.1.2 Off Axis Parabolic Mirror

OAP is a mirror whose reflective surface is a circular segment of paraboloid (named as the parent parabola) and its physical center does not match the optical axis (referring to off-axis) [47]. This type of mirror is basically a cutted part of the parabolic mirror (figure 3.7), and where it is cutted will determine the characteristics of that mirror itself. The incident

light falls in different parts of the parabolic mirror will produce reflected light in different direction and deflection. This type of mirror is very sensitive toward alteration of position coordinate. The fabrication of the OAP itself requres high precision cutting machine, so that it delivers reflected light in specific direction and angle as it is expected, without any flaw.

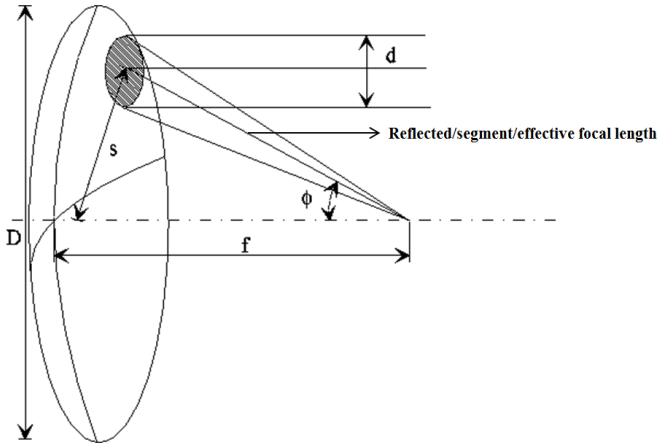

Figure 3.7: Parabolic mirror. The grey part is the OAP [47].

OAP is used to collimate diverged light or focus collimated light, and this is taking place if the distance between the source and OAP meet the requirement. Off-axis distance of the OAP is defined by the distance s between the center of the OAP and the axis of revolution of the paraboloid, measured along a perpendicular to the axis. There are several important parameters defining OAP: Parent focal length f, incident angle (off-axis angle) between axis with respect to the reflected focal length of the OAP (segment or effective focal length) ϕ and diameter of the OAP D. Detailed characteristics of the OAP can be read further in reference [48].

OAP 90°. The off-axis angle of this parabolic mirror is 90°. In order to achieve proper focus, collimated beam should be normal to the OAP 90°, as it is shown in figure 3.8. The OAP employed in the setup is built by Newport with the name of the model is 50329AL, made and coated with alumunium. Substantial information is given in table 3.4.

Table 3.4: OAP 90° substantial information [49].

Reflected Focal length	2.0 inch (5.08 cm)
Parent Focal Length	1.0 inch (2.54 cm)
Diameter	1.0 inch (2.54 cm) [50]
Thickness	1.25 inch (3.17 cm) [50]

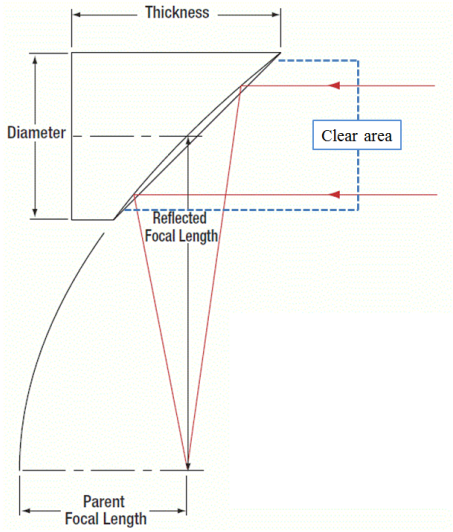

Figure 3.8: OAP 90°. The clear area is more than 90% diameter [51].

Figure 3.9 shows response of the OAP 90° in wavelength vs reflectance. In the wavelength between 0.2 μm - 0.4 μm, the reflectance of this mirror is very low (Au type). After that, the reflectivity gradually increasing and reach 98 % - 99 % in the near–IR region.

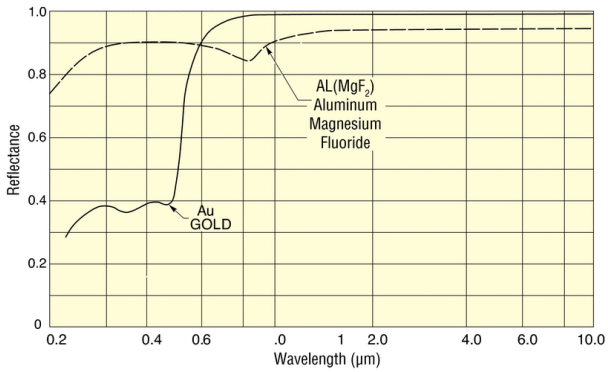

Figure 3.9: OAP 90° response to reflectivity based on the wavelength working range [49].

OAP 15°. The different way to use this compared to OAP 90° is by making angle of 15° between collimated beam and surface of the OAP 15°. The setup for this type of OAP is much harder than the previous one in terms of alignment. One thing to remember, that OAP is very sensitive toward small alteration in position. For this measurement, the chosen OAP is Edmund Optics model #69–155, coated with alumunium, as shown in figure 3.10 with the explanation of the symbol in table 3.5.

Table 3.5: OAP 15° substantial information (dimension in cm) [52].

Diameter	Parent FL	EFL	Y Offset	A	B	C
2.54	63.5	65.49	16.72	0.965	63.19	0.64

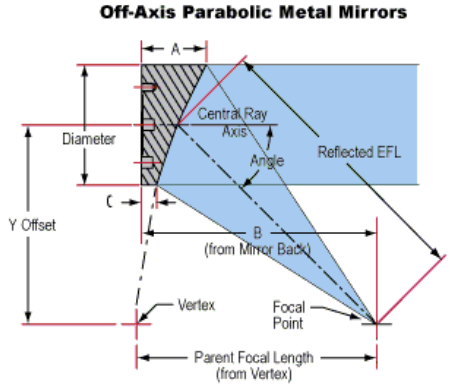

Figure 3.10: OAP 15° [52]. Clear area is not spescified in this component.

Reflectivity response of the OAP 15° in wavelength vs reflectance is given in figure 3.11. Overall performance of this OAP is much better than Newport OAP 90° even both of them made and coated from the same material. It gives reflectivity above 87 %, but sudden drop experienced to 85 % in the wavelength of 1000 nm. High reflectivity achieved in the near–IR region, with the reflectivity coefficient above 96 %.

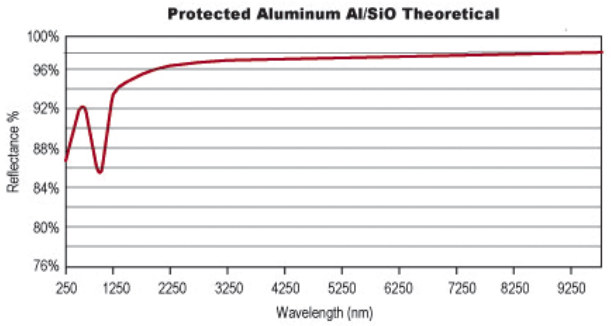

Figure 3.11: OAP 15° response to reflectivity based on the wavelength working range [52].

3.2.1.3 50 cm concave mirror

The last optical components to be added in the system is concave mirror with focal point of 50 cm, diameter of 2 inch (5.08 cm) coated with alumunium, shown in figure 3.12. The reflectivity response to wavelength is given in figure 3.13. Overall performance given in reflectance of 90 % but shows lowest reflectance response of 77.5% in 310 nm. It is written in datasheet of this component [53] as well as in figure 3.13, that the wavelength range is stretching from 250 nm - 600 nm. No further data above 600 nm, and since our PR working range is extending up to 1600 nm, we assume that there will be lost of some fraction of the light intensity and be readily know if there is unexpected result in the spectrum of low energy.

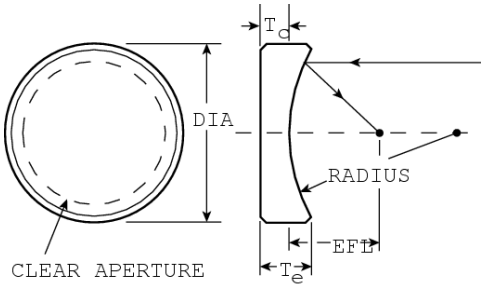

Figure 3.12: Concave Mirror with focal point of 50 cm and diameter of 2 inch (5.08 cm) [53].

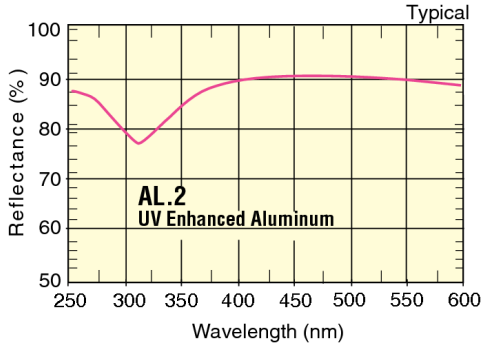

Figure 3.13: Concave mirror response to reflectivity based on the wavelength working range [53].

3.2.2 Optical Setup

There are several combinations of these components which have been tested, and among them will be presented three setups (first and second setup are presented in the appendix A) which considered as acceptable because they give good result in delivering focused light as well as maintaing light propagation from the exit slit of monochromator continuously down to the sample surface. Each setup will be explored the advantage and disadvantage so that they will account which one will be used for the PR data measurement.

As a reminder, this work has dealt with two different monochomators: iHR550 Jobin Yvon and Bentham TM300V. These two monochromators have distinct features one toward the other, but in the case of the optical system re-designing, the distance will be the main focus. It was intended that iHR550 would replace the old monochromator, TM300V. In the process, unfortunately the iHR550 faced many problems and to make sure this study finish on time, TM300V being used once more. Later in the optical setup, especially in 1st and 2nd optical design, iHR550 was used. The third setup, the optical design for both iHR550 and TM300V are presented, with difference in the distance of the OAP 90° with respect to the exit of monochromator.

Placement of the OAP 90°. One of the most important alignment in this setup is the positioning of OAP 90°. From section 3.2.1.2, the OAP 90° demands distance of 5.08 cm to be able transforming diverged light to collimated light. The setup of OAP 90° in front of exit slit of the monochromator is shown in figure 3.14.

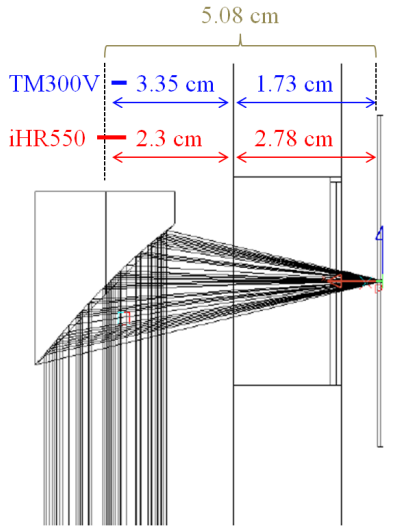

Figure 3.14: Placement of the OAP 90° with respect to monochromator exit slit.

Some assumptions are made in designing the exit slit of the monochromator together with the point source inside it. Rough calculation shows that distance between point source to the edge of the exit slit is 2.78 cm for iHR550 (1.73 cm for TM300V). Since the OAP 90° need distance of 5.08 cm from the center of the mirror surface to the point source, it means that OAP 90° must be moved 2.3 cm away from the exit slit (3.35 cm for TM300V). With the present distance, the condition is met, which we can see from the figure 3.14. Though in reality, a diverged light still found but it does not scattered too much from the center with the help of this device. This setup is fixed throughout three different optical setups.

Third setup. In the last setup, concave mirror with focal length of 50 cm is employed. Taking advantage from the second setup, this mirror substitutes concave mirror with focal length of 40 cm owing to the fact that there will be more 10 cm space available for other components. The other components are similar from previous setup, just that the position are shifted adapting the change of the new concave mirror. The proposed setup is shown in figure 3.15a. The purpose of the OAP 15° is to compensate imperfect paraxial light rays from the OAP 90°, but now it is placed further back in order to bring flat square mirror closer to the OAP 90° than the preceeding setup. The purpose of this extending distance is still the same as before: to achieve light rays fill the whole clear area of the concave mirror (f=50 cm), see figure 3.12. By placing the components further with respect to each other, they will increase the probability of the light rays to get larger, but not exceeding the surface area of the optical components.

The area of focused spot achieved with entrance slit of 0.5 mm and exit slit of 0.5 mm is 3×5 mm^2, the largest spot size achieved compared to the previous setups. In PR measurement, smaller spot is more desired than the bigger one, by virtue of the compatibility to sample size and laser spot size. There is one reason explaining this numbers: size of the light rays which are not able to fill the surface of concave mirror's clear area. This part is crucial if smallest spot want to be achieved. The decision to use 50 cm concave mirror with diameter of 5.08 cm has its own reason. Risk of getting bigger spot has been predicted, and this loss is not that significant compared to suffering of abberation in the edge of the mirror. Avoidance of the abberation error is compensated by the unwanted area of spot size. But, the spot size area is still tolerable and more importantly the spot size in detector is acceptable.

Simulation result of the third setup is given in figure 3.15b. It illustrates that a focal point falls further away than the sample. This result is expectedly occured since simulation environment assumes everything is ideal. This is apply for both OAP, where the diverged light will get perfectly collimated if the certain criteria is met. This criteria, which is distance, has set such that the OAP works as it is written in the datasheet. This is not happen in the real world. OAP 15° is the hardest components in this setup to align, since there is no standard measurement to calculate incident and reflected light to make an angle of 15°. The result of the OAP 15° makes difference between simulation and real world. As a note, OAP 90° also shows a deviation in the experimental, but it is tolerable compared to the result given by the OAP 15°. In simulation, OAP 15° causes collimated light to be focused at its focal length, i.e. 65.49 cm (see table 3.5). It means the distance s counted from focal point of OAP 15° to the 50 cm concave mirror is 80 cm. With the simple expression of $\frac{1}{f} = \frac{1}{s} + \frac{1}{s'}$, point where the formed image distance is in 133 cm away from the concave mirror. It is depicted exactly in the figure 3.15b with symbol 'F', located 2.5 times away compared from the sample to concave mirror.

Another similar simulation is conducted, illustrated in figure 3.15c. The difference with the simulation in figure 3.15b is the replacement of OAP 15° with the flat mirror. In the experimental condition, light from the OAP 15° does not focus during propagation in any point toward the to flat square mirror, only fix the imperfect paraxial light. The result of this simulation demonstrate the same outcome as in the real condition: focused spot in the sample surface. Due to the compactness factor and tolerable focused area in the sample as well as detector, this setup will be used for the PR measurement data.

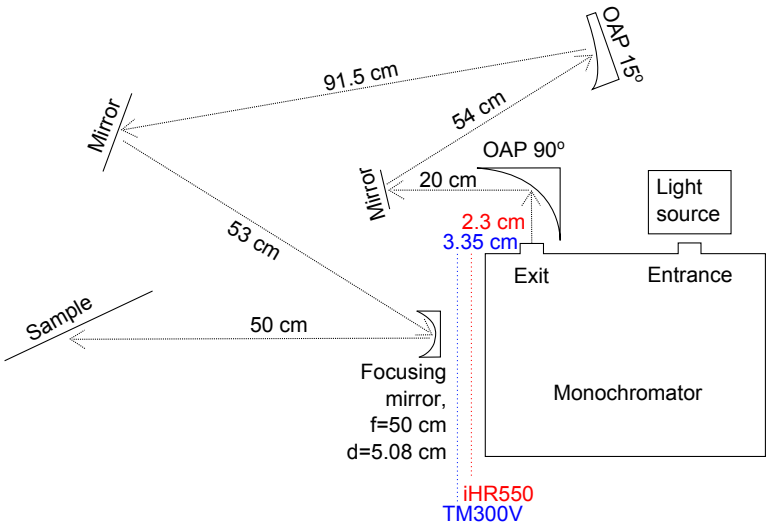

(a) Third setup of proposed optical design.

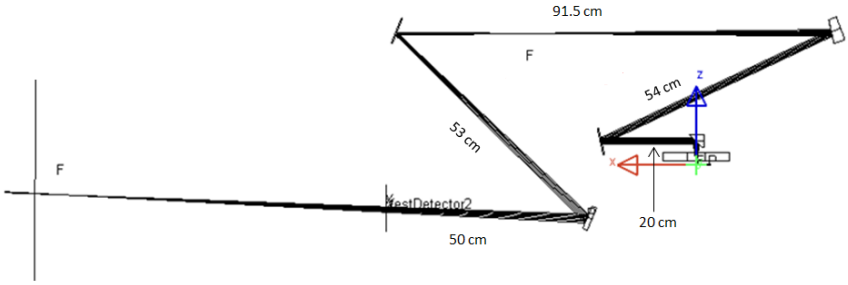

(b) Simulation of third setup optical design.

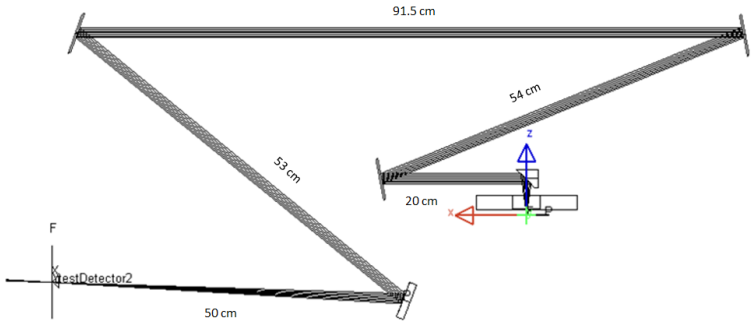

(c) Simulation of third setup optical design, compensated with the flat mirror replacing OAP 15°.

Figure 3.15: Third as a final setup.

Further simulation with the third setup. In simulation, point type source is used for modelling the light source, while in the experimental work, the light source is consisted of thousand point sources forming sphere source. It is explaining the reason of the imperfectly paraxial light rays in experiment. In order to make simulation work approaching experimental work, the line source is decided to be used, instead of sphere source considering of practicability and time-saving factors. It is pointless to model sphere source since the light rays which can pass the exit slit coming from the closest point sources to the slit. Extra sources will lead only to the accumulating in intensity of the detected light. The modelled line source consists of two columns with several lines of point sources (0.2×5 mm^2), placed in the vicinity to the slit width of the monochromator exit slit and each of the point source has opening angle of 14° (based on the F–number of the Bentham TM300V [42] and calculation by Hofstad [40]), depicted in figure 3.16.

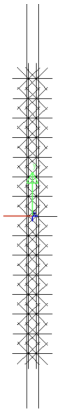

Figure 3.16: Line source with several 14° point sources arranged in 0.2×5 mm^2.

With the setup from figure 3.15b, installation of this new line source replacing the point source lead to the new result, as illustrated in figure 3.17

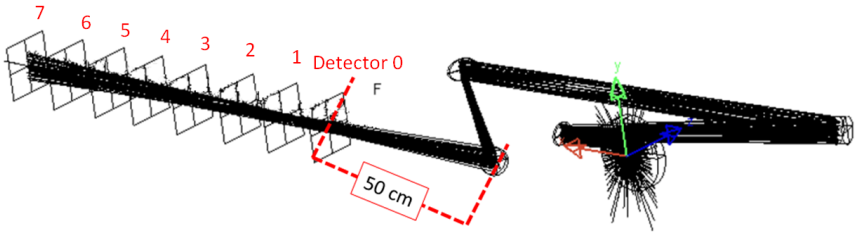

Figure 3.17: Result of light propagation using line source.

Several detectors are placed in front of the concave mirror (f=50 cm), with the "Detector 0" located 50 cm from it and the rest of the detector are 10 cm discrepancy with each other. The results are given in figure 3.18. The focused light falls on the detector 0 (figure 3.18a), therefore this simulation result has proven result of the empirical work.

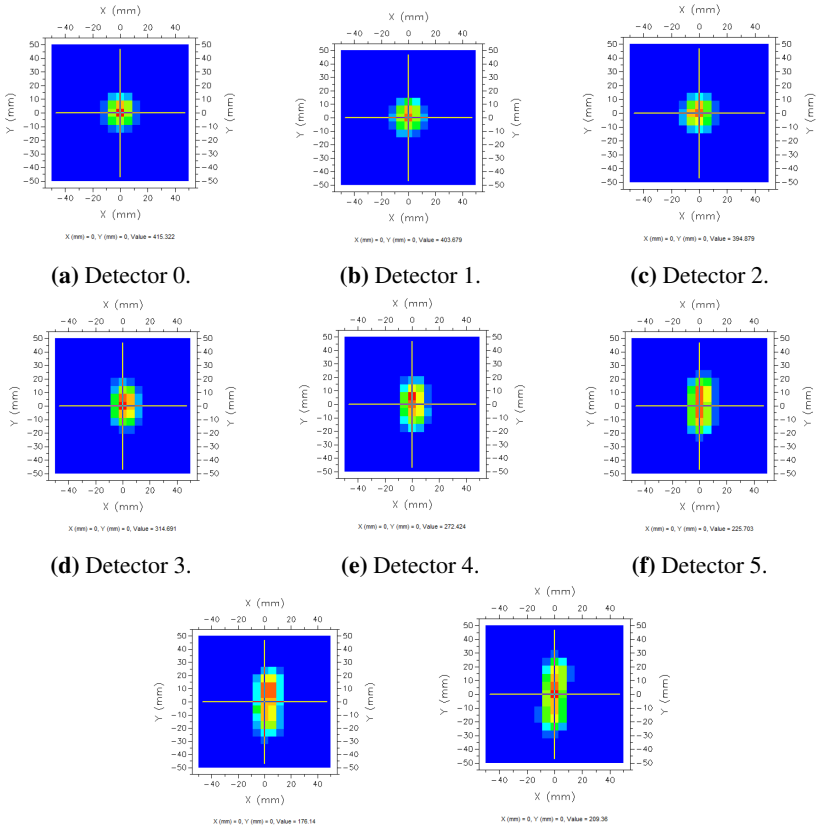

(a) Detector 0. **(b)** Detector 1. **(c)** Detector 2.

(d) Detector 3. **(e)** Detector 4. **(f)** Detector 5.

(g) Detector 6. **(h)** Detector 7.

Figure 3.18: Illuminance chart for each detector.

Miscellaneous. Since the spot size with the final setup is not forming a point, diverging lens (beam expander) must be added to make a laser beam diverged, to make it has equal spot size as probe beam in the sample surface.

In the experimental work of PR, the entrance slit is opened with the width of 1.9 mm, while the exit slit of 0.2 mm. This gives a bandwidth of 0.54 nm (500 nm peak efficiency) and 1.08 nm (1600 nm peak efficiency) [42]. The purpose of the wide opening in entrance slit is to let as much as the incoming light into the monochromator, but making the exit slit as narrow as possible to decrease the exit bandwidth i.e. wavelength resolution is higher. Compared to old setup, we have increased SNR in the new setup due to the lowered of exit slit (0.2 mm vs previously 0.5 mm).

The spurious modulated background signal reaching the detector due to luminescence from the sample (trapped photo-generated carriers in surface states) and scattered light from pump source will add complexity in analyzing the spectrum because of the interference effect with the signal of interest.

3.3 Early Test of Photoreflectance Data Measurement

The purpose of this test is to reproduce PR spectrum from the sample which has been measured in the old setup. Verification of the new setup is conducted to generate PR signal as well as demonstrates superiority above the old setup.

The samples which are going to be exploited are AS565 and AS577. The slit of the monochromator is adjusted at 1.9 mm and 0.2 mm for the entrance and exit slit, respectively. 1 s is the parameter set for the time constant in lock-in amplifier, referred to the suggestion by Hofstad [40], and the sensitivity is put in 100 μV.
The PR result of sample AS565 is given in figure 3.19.

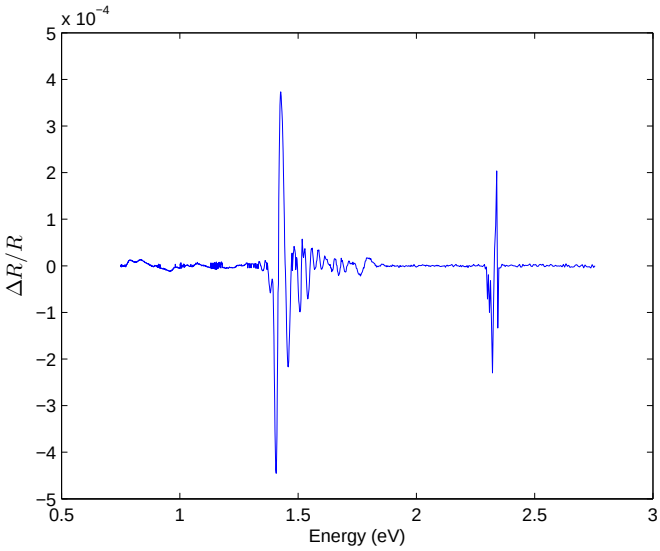

Figure 3.19: PR spectrum of sample AS565.

From figure 3.19, we observe four major events: peak at 1.424 eV, damped oscillation from 1.425 eV to 1.7 eV, small signal in 1.8 eV and random peak at 2.34 eV. These signals represent material characteristics under investigation. Peak at 1.424 eV is the position energy of the GaAs energy bandgap, while damped oscillations from 1.425 eV to 1.7 eV are the effect of the FK. Following these features, another small signals noticed at 1.8 eV are believed to be signal coming from $Al_{0.35}Ga_{0.65}As$ energy bandgap. According to the datasheet of AS565, this material composed of GaAs (420 nm), $Al_{0.35}Ga_{0.65}As$ (400 nm) and $Al_{0.8}Ga_{0.2}As$ (30 nm). The latter material has energy bandgap in 2.09 eV, but not observable due to the negligible thickness compared to other materials. Random peaks at 2.34 eV and its vicinity are response of the green filter in front of the detector box.

The result of AS565 from old setup is depicted in figure 3.20. Remember that the high amplitude of the order of 10^{-3} is a result from green filter. Signal of the GaAs is detected in 1.424 eV, followed by its FKO. The highest peak of the GaAs at 1.424 eV recorded at 1.5×10^{-4}, lower than value found in new setup, which is 4×10^{-4}. The inferiority

of the old setup shown by its failure to detect $Al_{0.35}Ga_{0.65}As$. This measurement used Si-detector only. No further information about the width slit in the entrance and exit slit

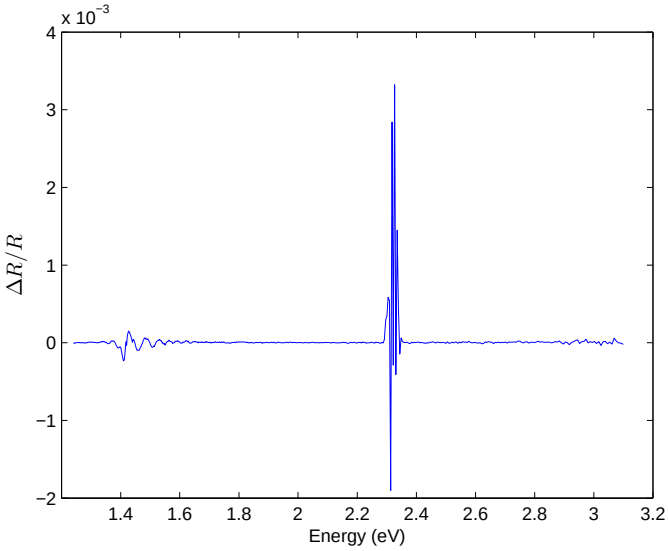

Figure 3.20: PR spectrum of sample AS565 from old setup.

The PR result of sample AS577 is shown in figure 3.21. The spectrum of AS577 is completely different from AS565. The same random oscillations in 2.34 eV also take place in AS577, due to the green filter, suppresing signal of green band wavelength (523 nm to 546 nm). The distinctive peak at 1.92 eV is most likely that the substrate is $Al_{0.35}Ga_{0.65}As$, which finds the agreement with the Nowaczyk et al. [54]. In addition, FKO is found at 2.01 eV to 2.138 eV exhibiting less number of oscillations compared to AS565. The faster damping is related with the increasing of broadening and/or some non-uniformity in the electric field [54]. Other than these feature, there are interesting long period oscillation observed in 1.5 eV to 1.73 eV as well as weak oscillation extending from 1.2 eV to 1.5 eV. The first one is associated with first transitions H1l, as described also by Sek et al. [55]. The weak oscillations ranging from 1.2 eV to 1.5 eV are most likely an interference signal from composed materials in the sample. No GaAs peak feature commenced from the spectrum concluding that AS577 is mainly formed by $Al_{0.35}Ga_{0.65}As$. Additional examination are not added since the database of this sample is not provided.

The same sample was measured with the old setup, given in figure 3.22. The measurement conducted from 800 nm up to 1650 nm or 0.75 eV to 1.55 eV. There is no record about how the data measurement taken, information about what detector used and slit width of the monochromator. Judging from figure 3.22, the detector employed is InGaAs. It is strange to notice a continuous drop started from 1.3 eV. This is caused most probable by insensitivity of difference when the modulation is present $R_{laserON}$ and absent $R_{laserOFF}$ as well as triggered by loss of light intensity during its propagation in the setup.

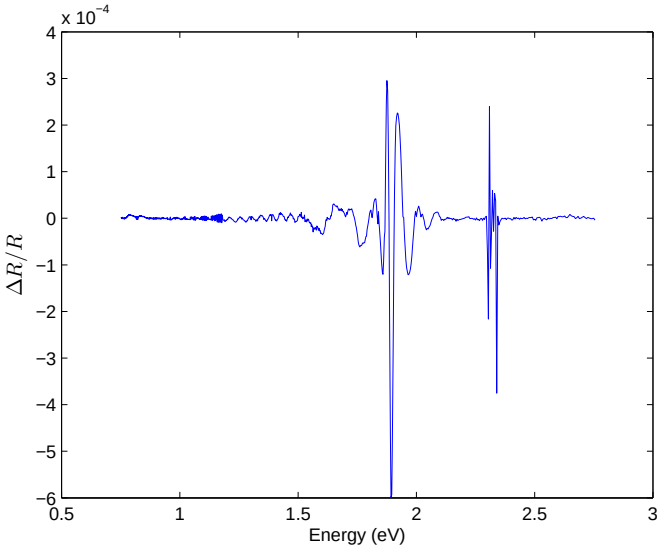

Figure 3.21: PR spectrum of sample AS577.

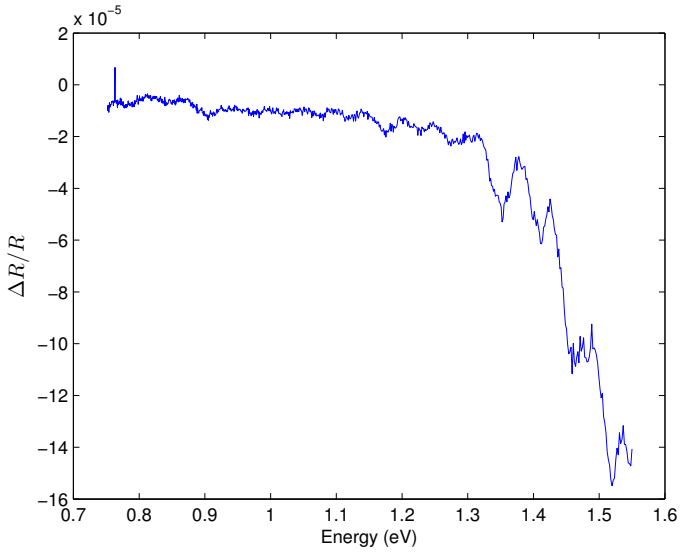

Figure 3.22: PR spectrum of sample AS577 from old setup.

Chapter 4

Mathematical Model

4.1 Franz-Keldysh Oscillations

Finding of small change in energy bandgap due to the FK effect which leads to FKO, determines the electric-field at the interface (built-in electric field). The importance of finding FKO is unavoidable, since it governs the evaluation of the built-in dc electric fields F_{dc}. By evaluating the values of the built-in dc electric fields F_{dc}, information of doping levels deduction are made possible [56].

According to Aspnes and Studna, The FKO related with the ratio between small change of reflectance ΔR to reflectance R, is expressed as follows (mentioned in chapter 2.5.2, equation 2.8), [31]

$$\frac{\Delta R}{R} \propto \frac{1}{E^2(E-E_g)} exp\left[-2(E-E_g)^{1/2}\frac{\Gamma}{(\hbar\Omega)^{3/2}}\right]\cos\left[\frac{4(E-E_g)^{3/2}}{3(\hbar\Omega)^{3/2}}+\chi\right] \quad (2.8)$$

Electro-optic energy is defined as the required energy to support band-bending occurence so that it can be conducted successfully, i.e. FKO. The last term in equation 2.8 is the expression for deciding number of extreme oscillation $n\pi$ caused by the FK effect, expressed by [20],

$$n\pi = \frac{4}{3}\left(\frac{E-E_g}{\hbar\Omega}\right)^{3/2} + \chi \quad (2.9)$$

Location of energy representing where the extreme oscillation n occured is denoted with E_n. Once the electro-optic energy found, it will lead to the built-in electric field F_{dc} which in the following equation is equal with ξ, from equation 2.6

$$\xi = \frac{(2\mu_{||}(\hbar\Omega)^3)^{1/2}}{e\hbar} \quad (4.1)$$

Many distinguished oscillations (above 20 extremes) caused by FK effect above the band gap energy (see figure 4.1) are demonstrating the existence of a strong uniform electric field in the very high quality epitaxial layer [54, 57].

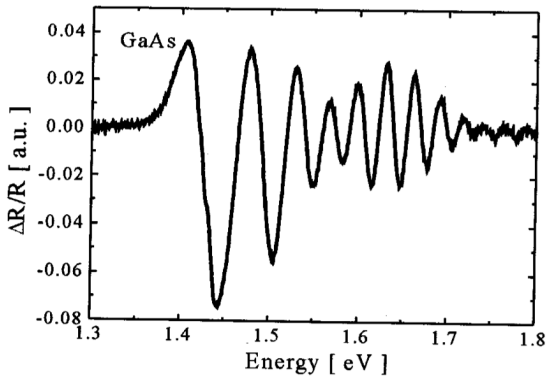

Figure 4.1: PR spectrum of the GaAs δ-doped sample, showing many FKO [54].

FKO is characterized by its occurence in the vicinity of the absorption edge, where the materal changes from being tranparent to absorbing. If there is another similar circumstance where oscillations take place in the energy location far from the bandgap of material, it is mostly not belong to the FKO.

In order to get insight of the quantitative value of presented equations, one example taken from [46], where the reproduced PR spectrum is shown in figure 4.2.

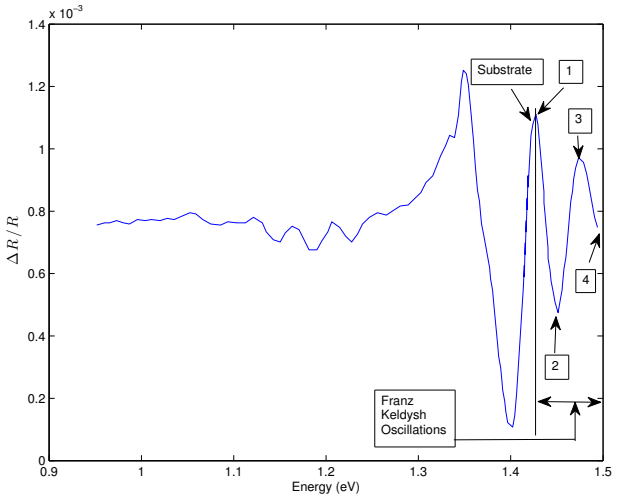

Figure 4.2: PR of an IBSC based on InAs/GaAs QDs [46].

GaAs substrate energy bandgap is 1.424 eV. The n-th extreme point has been labelled in the figure 4.2, identified that there are four of them. Table 4.1 recapitulates energy needed to conduct oscillations at the point n,

Table 4.1: n-th extreme point with its corresponding energy E_n

n	E_n (eV)
1	1.427
2	1.451
3	1.474
4	1.494

Arrangement in equation 2.9 yields to,

$$n(\hbar\Omega)^{3/2} = \frac{4}{3}\frac{(E - E_g)^{3/2}}{\pi} \tag{4.2}$$

To obtain the electro-optic energy $\hbar\Omega$, simple linearity plotting method is used, therefore the gradient of the line slope m stands for electro-optic energy. From equation 4.2, the x-axis is n and the y-axis is $\frac{4}{3}\frac{(E-E_g)^{3/2}}{\pi}$. The plotting of this data is depicted in figure 4.3,

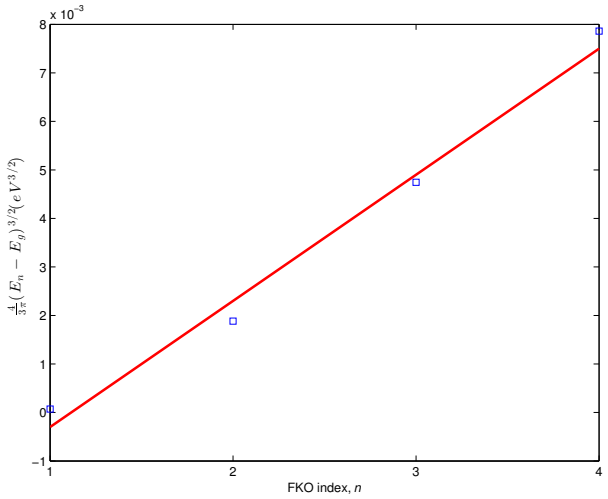

Figure 4.3: Linearity plot of the figure 4.2.

The line fitting from the figure 4.3 is,

$$y = 0.0026 - 0.0029x \qquad or \qquad (\hbar\Omega)^{3/2} = 0.0026 - 0.0029x \tag{4.3}$$

To find the gradient m using equation 4.3,

$$m = \frac{y_2 - y_1}{x_2 - x_1} \tag{4.4}$$

The value of electro-optic energy is 0.0189 eV. Using equation 4.1 with the value of GaAs interband effective mass $\mu_{||}$ ($\mu_{||} = \frac{m_e m_h}{m_e + m_h}$) of $0.0561 m_0$ (5.1027×10^{-32} kg), electron charge e of 1.6×10^{-19} C and Planck's constant $\hbar$ of 6.63×10^{-34}. The calculated built-in electric field is 31.5574 kV/cm.

The relations between PR lineshape ($\Delta R/R$) to Seraphin coefficients (α-β) and dielectric constant: real $\Delta\epsilon_r$ and imaginary $\Delta\epsilon_i$, are represented in equation 2.4. Since dielectric constant $\Delta\epsilon \sim$ first kind of Airy function $F(\eta)$, therefore, fitting of the FKO can be established using Airy function first kind $F(\eta)$ (equation 2.10),

$$F(\eta) = C\pi[Ai'^2(\eta) - \eta Ai^2(\eta)] - (-\eta)^{1/2} H(-\eta) \qquad \eta = \frac{E_g - E}{\hbar\Omega} \tag{2.10}$$

For real values of η, the Airy function can be defined by the

$$Ai(\eta) = \frac{1}{\pi} \int_0^\infty \cos\left(\frac{t^3}{3} + \eta t\right) \mathrm{d}t \tag{4.5}$$

The fitting result of this case is given in figure 4.4

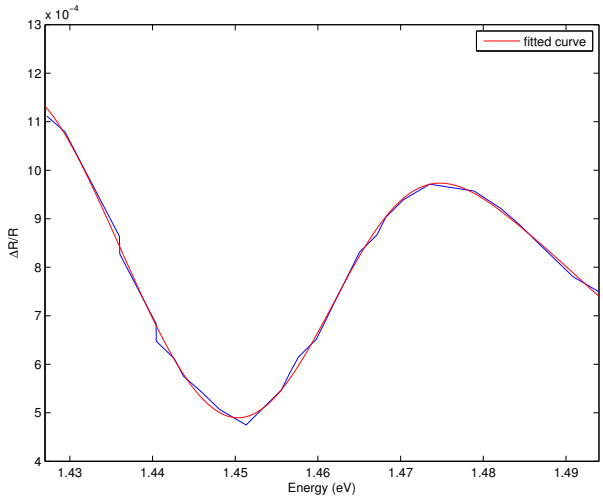

Figure 4.4: Airy fitting on the FKO of figure 4.2.

Result of the fitted parameter (with root mean square of 0.9965) from figure 4.4 in the region from 1.427 eV-1.494 eV is,

$$E_g = 1.423 \quad \text{eV} \qquad \text{and} \qquad \hbar\Omega = 0.016 \quad \text{eV}$$

The output of the GaAs bandgap E_g and electro-optic energy $\hbar\Omega$ fitting produces number which is close to the value obtained before. It indicates that this result is acceptable.

Estrera et al. built the line shape by adding critical point features as necessary to account for PR response. Meaning that the PR fitting has additional below band-gap features

modelled by first derivative lorentzian lineshape, stated in equation 4.6, in addition to FKO expressed in Airy lineshape [7]. The first PR sample comes from Si-doped (10^{15} cm^{-3}) metal organic chemical vapor deposition (MOCVD) GaAs, fitted with one Airy lineshape [7]. It shows satisfactory fitting at the band edge, but not adequate in higher energies. Additional of a second Airy component enhance the fitting quality in the FKO spectrum as in figure 4.5a .

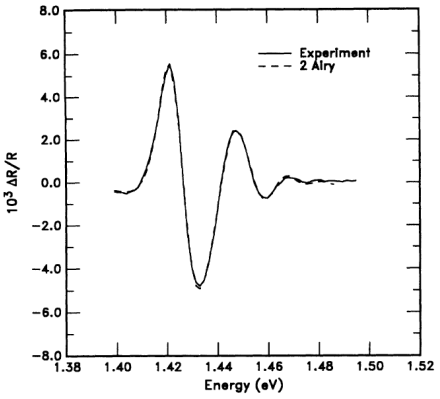

(a) Fitted with two Airy profiles (GaAs-1).

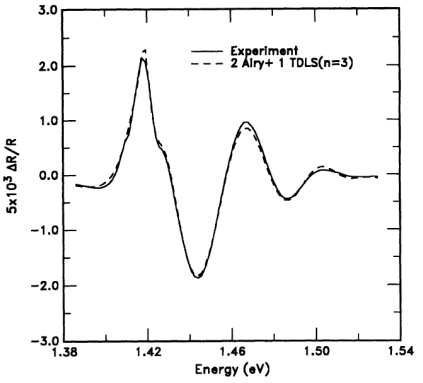

(b) Fitted with two Airy profiles and one first derivative lorentzian lineshape (GaAs-2).

Figure 4.5: FKO of intermediate-field PR spectrum fitted with various method [7].

Another presented example is MOCVD grown bulk GaAs with Si doping of 10^{16} cm^{-3}, with the result of the fitting in figure 4.5b. Kink around the band edge of GaAs is able to be resolved in the fitting. The fitting using combination of two Airy line shapes and one first derivative lorentzian lineshape below the band-gap energy are achieved with the third derivative two-dimensional critical point (m=3) (in figure 4.5b, the critical point is defined by n instead of m). Selected GaAs parameters in figure 4.5 are presented in table 4.2

Table 4.2: Selected GaAs parameters from figure 4.5 in the vicinity of E_0 and $E_0 + \Delta_0$. E_{cp} is the critical-point energy from the PR fitting and photoluminescence at 293 K (room temperature)-PL RT [7]

	GaAs-1	GaAs-2
$E_{cp}(eV)$	1.421	1.422
PL RT $E_0(eV)$	1.422	1.422
ξ (kV/cm)	14.5 ± 5	35 ± 5
μ_{LH}/μ_{HH}	0.71 ± 0.05	0.66 ± 0.05
Δ (meV)		3.33

4.2 Wetting Layer and Quantum Dots

After finding the electro-optic energy and built-in electric field in the FKO together with the fitting result of it, another interesting feature such as WL and QDs will be investigated. Redrawing figure 4.6 from reference [54],

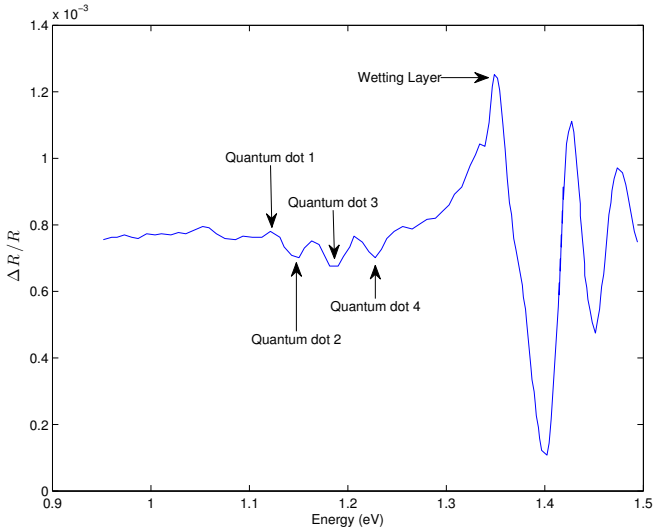

Figure 4.6: PR spectrum of the GaAs δ-doped sample, concentrating on WL and QDs features [54].

Recalling equation 2.7, since WL and QD are belong to confined structure, the PR spectrum is expressed as first derivative of the Lorentzian function [26–30], as follows,

$$\frac{\Delta R}{R} = Re\left[Ae^{i\phi}(E - E_g + i\Gamma)^{-2}\right] \tag{4.6}$$

The fitting result of the parameters listed in equation 4.6 are summarized in table 4.3.

Table 4.3: Experimental PR energy peaks for InAs/GaAs QDs compared to the result found by Cánovas et al. [46]

Peak	E_g (eV)	E_g (eV) [46]	Γ
WL	1.35	1.349	0.0245
QD 4	1.234	1.227	0.03521
QD 3	1.195	1.183	0.02016
QD 2	1.141	1.147	0.02155
QD 1	1.129	1.121	0.01529

Chapter 5

Result and Analysis

QD-IBSC samples which are going to be investgated in this work were grown by Thomassen using MBE method and the QDs in it fabricated by utilizing Stranski-Krastanov growth method [10]. There are five different samples which are belong to series 1, listed in table 5.1, with their associated parameters.

Table 5.1: Parameters attributed in series 1 samples. The samples investigated in this work grown by Thomassen [10].

Sample	T_{QD} $(^{\circ}C)$	In:As_2	T_{SL} $(^{\circ}C)$	QD layers	V_{OC} (V)	J_{SC} (mA/cm^2)	Fill factor (%)
1:1 (AS564)	435	1:9	435/590	5	0.706	8.38	76.1
1:2 (AS579)	435	1:9	435/590	20	0.716	7.07	73.5
1:3 (AS566)	475	1:9	475/590	5	0.710	8.68	75.8
1:4 (AS570)	475	1:37	475/590	5	0.699	8.72	77.4
1:5 (AS568)				0	0.944	8.58	79.2

Structure of series 1 is illustrated in the figure 5.1. Among samples in series 1, sample 1:5 is a reference sample, grown without QD in it, instead it is filled with intrinsic GaAs (i-GaAs). The original purpose of this sample was to become performance benchmarks to the other series. Sample 1:1-1:4 contain their own QD numbers, growth in different temperatures and number of layers as well as ratio of In to As_2. From table 5.1, sample 1:1 shows similar growth condition with sample 1:3 except for the Reell temperature T_{QD}. Sample 1:2 and sample 1:4 give insight of different parameter in number of layers and In:As_2 ratio, respectively. Thomassen conducted measurements in the external quantum efficiency (EQE) together with PL spectroscopy measurement, ranging from 400 nm to 1250 nm [10].

The sample structure of 1:5 and 1:1-1:4 are depicted in figure 5.1. The samples are generally composed of two materials: GaAs and $Al_xGa_{1-x}As$ with the composition of x claimed to be 0.8. The QD region consists of five or twenty periods of a 2.1 monolayer (ML) InAs QD layers and a 20 nm GaAs spacer doped with Si δ-doping in the middle

of each spacer. Sample 1:5 has 120 nm i-GaAs layer. All samples are doped with Be and Si for the p-GaAs and n-GaAs, respectively. The InAs QDs in sample 1:1 to 1:4 located in the middle part of the structure, sandwidched between p- and n-type of GaAs and $Al_{0.8}Ga_{0.2}As$ as shown in figure 5.1.

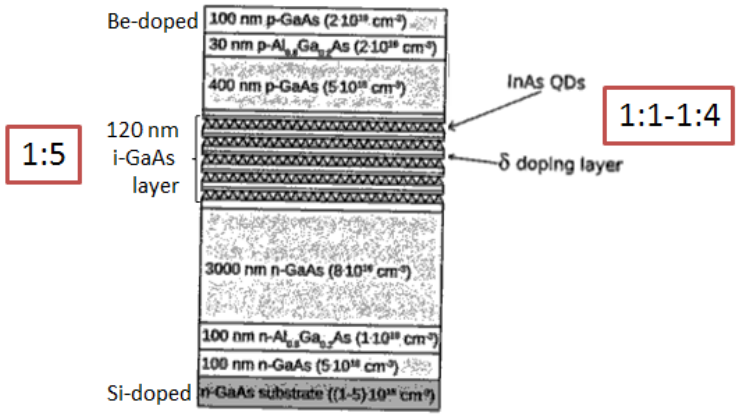

Figure 5.1: Solar cell structure of series 1. The QD region consists of 20 nm i-GaAs layer and five or twenty periods of 2.1 ML InAs QDs layers and 20 nm Si δ-doped GaAs spacer layers. The QD region is replaced by 120 nm i-GaAs layer in the GaAs reference cells [10].

Energy gap of the composing material in the series 1 is expressed in the following equations [58],

$$\text{GaAs} \quad E_g = 1.424\,eV \tag{5.1}$$

$$\text{Al}_x\text{Ga}_{1-x}\text{As} \quad E_g = (1.424 + 1.247x)\,eV \quad \text{for x<0.45} \tag{5.2}$$

$$= (1.9 + 0.125x + 0.143x^2)\,eV \quad \text{for x>0.45} \tag{5.3}$$

$$\text{InAs} \quad E_g = 0.354\,eV \tag{5.4}$$

5.1 Photoreflectance

5.1.1 Overview

All measurements are conducted in the range wavelength of 450 nm to 1650 nm or in the energy scale of 0.75 eV to 2.75 eV, with the detailed setup explained in the chapter 3.2. Anticipated random oscillations in the vicinity of 527.7 nm-541.5 nm (2.29 eV-2.35 eV) can be ignored for the further analysis. Another expected peaks are located in 1.424 eV for GaAs, 2.09 eV for $Al_{0.8}Ga_{0.2}As$ using equation 5.3 and oscillations raised up from InAs QDs transitions. The presented data have been smoothed so that it increases visibility.

The result of the PR spectrum for sample 1:1 through sample 1:5 are given in figure 5.2. The results for reflectivity, change in reflectivity and photoreflectance spectrum for each sample are given in appendix B.

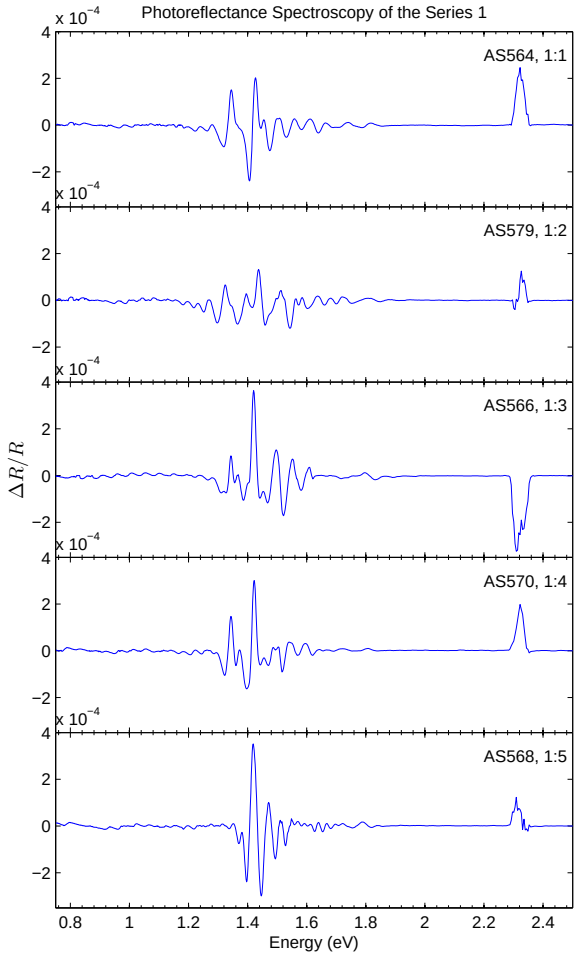

Figure 5.2: PR spectra of sample 1:1 through 1:5.

5.1.2 $Al_xGa_{1-x}As$

From figure 5.2, all samples in series 1 indicate absent of interesting features observed after 2 eV, only noise depicted as flat line without any peak. This finding tells us that expected energy gap of $Al_{0.8}Ga_{0.2}As$ in 2.09 eV does not exist. There is one possible answer for

this phenomenon: The $Al_xGa_{1-x}As$ energy gap has shifted to lower energy, implying that the x is not 0.8 as it was claimed before. The peak which is best predicted to be correlated with $Al_xGa_{1-x}As$ located in energy gap position of averagely 1.8 eV, and according to the calculation in equation 5.2, it has x of 0.3. The corrected fraction for the $Al_xGa_{1-x}As$ is then $Al_{0.3}Ga_{0.7}As$. The results of the fitting equation 4.6 of sample 1:1, 1:2, 1:3, 1:4 and 1:5 show E_g at 1.806 eV (Γ=57.74 meV), 1.841 eV (Γ=36.01 meV), 1.796 eV(Γ=59.18 meV), 1.808 eV (Γ=34.85 meV) and 1.782 eV (Γ=39.05 meV), respectively. The energy gap of $Al_{0.3}Ga_{0.7}As$ for all samples in series 1 are shown in figure 5.3. Similar result of the $Al_{0.3}Ga_{0.7}As$ energy gap by Sek et al. and Nowaczyk et al., which led to the finding energy position of 1.8 eV [54, 55, 59].

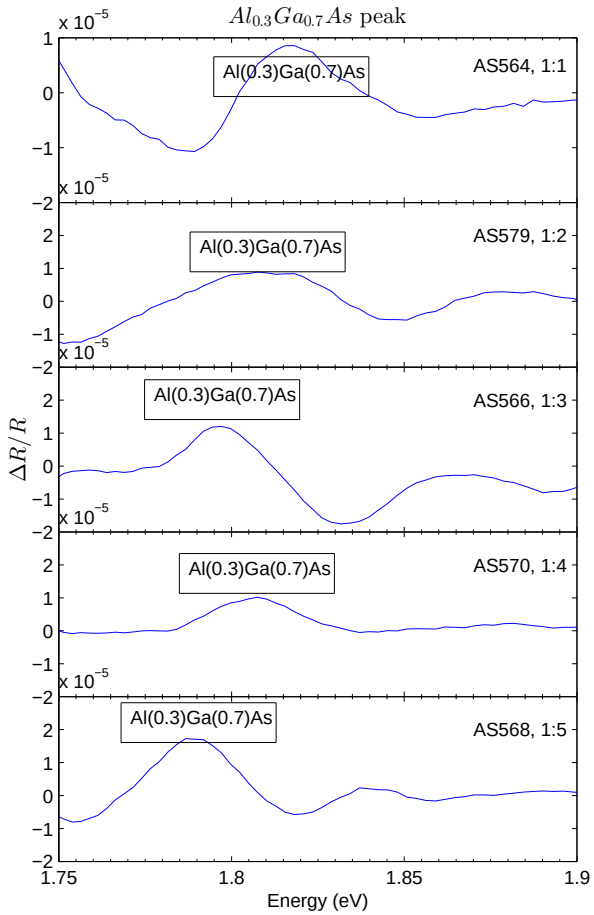

Figure 5.3: $Al_{0.3}Ga_{0.7}As$ peak at sample 1:1 through 1:5.

5.1.3 Franz-Keldysh Oscillations

5.1.3.1 GaAs

As part of the PR, FKO are observable to all sample depicted in figure 5.4 in the energy position after GaAs bandgap (1.424 eV) up to around 1.7 eV. This phenomenon is commonly found in the PR measurement [30, 33, 56, 60–66]. The FKO for sample 1:1 through 1:5 are given in figure 5.4.

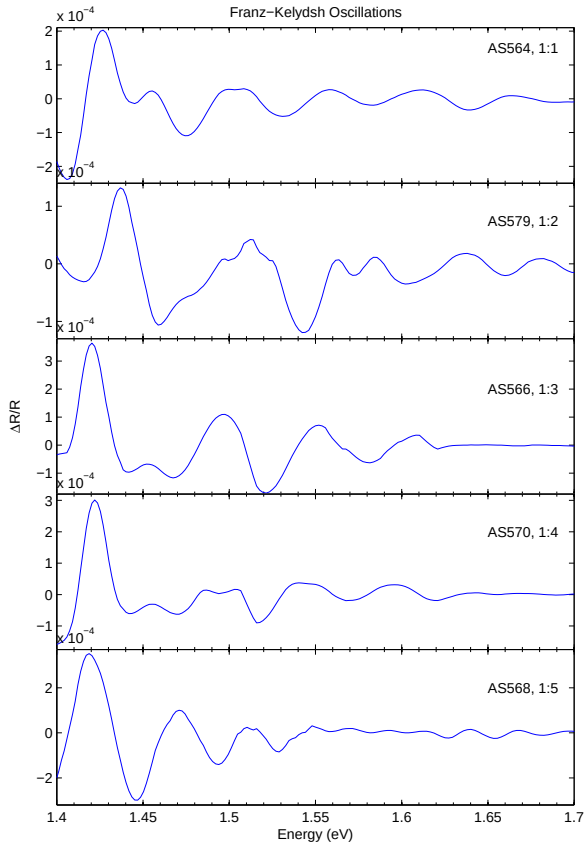

Figure 5.4: FKO of sample 1:1 to 1:5.

The calculations of electro-optic energy $\hbar\Omega$ and built-in electric field ξ based on the linearity plot as well as FKO fitting using Airy function will be based on the explanation in section 4.1. We will discuss in detail about these issues for each sample. It is important to keep the linearity of the line, and it will be our guideline in deciding when the oscillations vanish.

The linearity plot of sample 1:1 with its FKO is given in figure 5.5

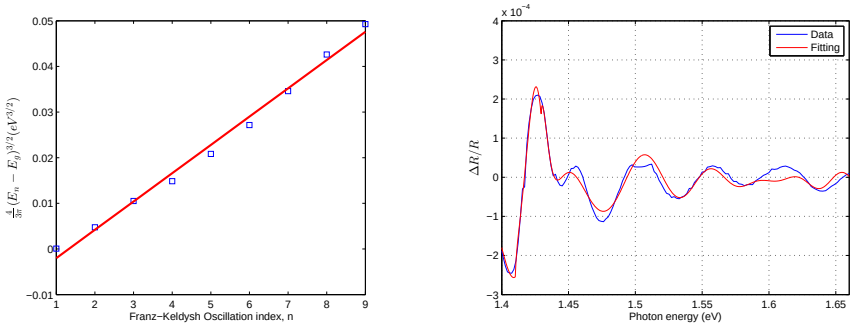

(a) linearity plot. **(b)** FKO.

Figure 5.5: Linearity plot and FKO of sample 1:1.

The theoretical result of the linearity plot (figure 5.5a) gives rise to electro-optic energy $\hbar\Omega$ of 0.0337 eV and built-in electric field ξ of 75.2523 kV/cm. Applying these values to predict the best fitting for Airy function (figure 5.5b), which shows the result energy gap E_g of 1.429 eV (Γ=18.97 meV) and electro-optic energy $\hbar\Omega$ of 0.03374 eV with the root mean square of 0.9615, which is better fit quality compared to the one without additional first derivatice lorentzian lineshape (0.8275).

The linearity plot of sample 1:2 with its FKO is given in figure 5.6

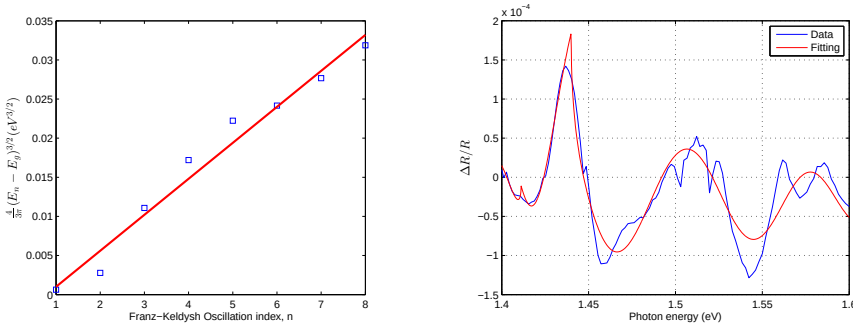

(a) linearity plot. **(b)** FKO.

Figure 5.6: Linearity plot and FKO of sample 1:2.

The theoretical result of the linearity plot (figure 5.6a) gives rise to electro-optic energy $\hbar\Omega$ of 0.0277 eV and built-in electric field ξ of 55.9858 kV/cm. The best fitting for Airy function (figure 5.6b) reveals the result energy gap E_g of 1.439 eV (Γ=39.21 meV) and electro-optic energy $\hbar\Omega$ of 0.03657 eV with the root mean square of 0.8652, achieving better fit quality compared to the one without additional first derivatice lorentzian lineshape (0.7439). The outcoming of the electro-optic calculation does not afford the fitting. The

reason for this dissimilarity is triggered by the dominating interference effect in the sample 1:2, where it changes the lineshape [66]. Analysis for this sample will be presented in the section 5.1.6.1.

The linearity plot of sample 1:3 with its FKO is given in figure 5.7

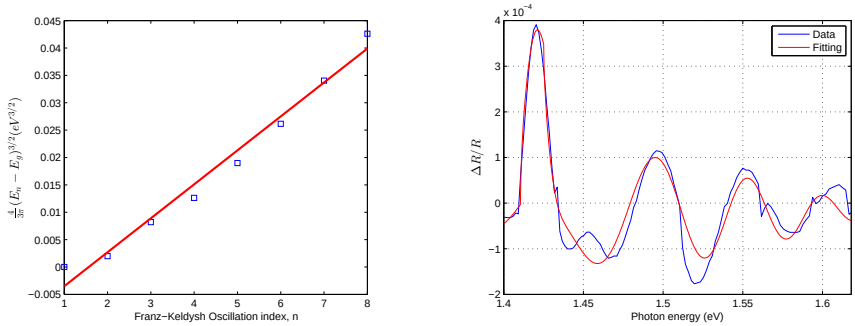

(a) linearity plot. **(b)** FKO.

Figure 5.7: Linearity plot and FKO of sample 1:3.

The theoretical result of the linearity plot (figure 5.7a) gives rise to electro-optic energy $\hbar\Omega$ of 0.0337 eV and built-in electric field ξ of 75.2523 kV/cm. These values lead to approximate values to get the best fitting for Airy function (figure 5.7b), which shows the result energy gap E_g of 1.425 eV (Γ=16.76 meV) and electro-optic energy $\hbar\Omega$ of 0.0344 eV with the root mean square of 0.9214, exceeding to the one without additional first derivatice lorentzian lineshape (0.8179).

The linearity plot of sample 1:4 with its FKO is given in figure 5.8

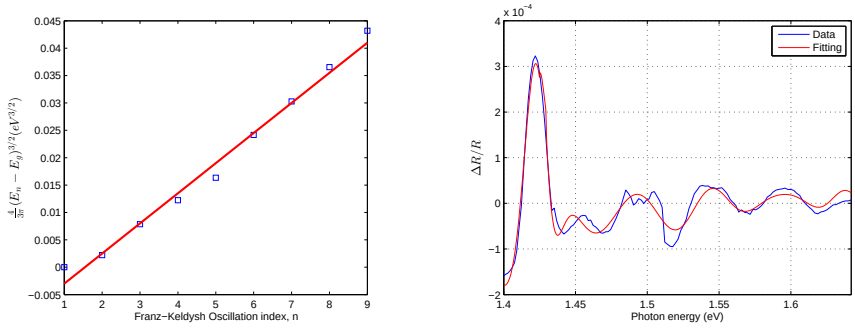

(a) linearity plot. **(b)** FKO.

Figure 5.8: Linearity plot and FKO of sample 1:4.

The theoretical result of the linearity plot (figure 5.8a) gives rise to electro-optic energy $\hbar\Omega$ of 0.0312 eV and built-in electric field ξ of 66.756 kV/cm. Based on this values, the best fitting for Airy function (figure 5.8b) produces the result energy gap E_g of 1.425 eV

(Γ=35.83 meV) and electro-optic energy $\hbar\Omega$ of 0.03138 eV with the root mean square of 0.9562, improved from the fitting without additional first derivatice lorentzian lineshape (0.8127).

The linearity plot of sample 1:5 with its FKO is given in figure 5.9

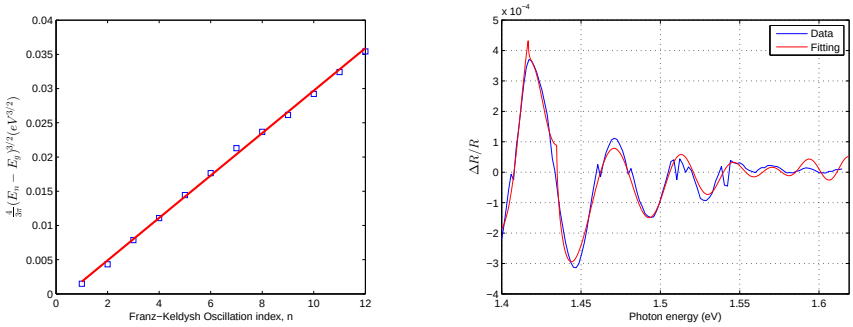

(a) linearity plot. **(b)** FKO.

Figure 5.9: Linearity plot and FKO of sample 1:5.

The theoretical result of the linearity plot (figure 5.9a) gives rise to electro-optic energy $\hbar\Omega$ of 0.0213 eV and built-in electric field ξ of 37.6261 kV/cm. By virtue of theoretical finding, the best fitting for Airy function is established (figure 5.9b), which arrive to the conclusion: energy gap E_g of 1.418 eV (Γ=21.52 meV) and electro-optic energy $\hbar\Omega$ of 0.02122 eV with the root mean square of 0.9623, surpassing fit quality of fitting without additional first derivatice lorentzian lineshape (0.8946).

The calculated results for each sample from 1:1 up to 1:5, both for electro-optic energy $\hbar\Omega$ and the built-in electric field ξ, provide us the qualitative general information about the sample structure. Overall, the outcome for electro-optic energy $\hbar\Omega$ and the built-in electric field ξ satisfy the intermediate-field regime. Sample 1:1 and 1:3 have the same value of electro-optic energy and built-in electric field (0.0337 eV and 75.2523 kv/cm). From table 5.1, it indicates that sample 1:1 and sample 1:3 show the same structure and share dissimilarity only in the growth temperature of T_{QD} and T_{SL}. Compared to another sample, 1:1 and 1:3 have the highest value of electro-optic energy and built-in electric field. Sample 1:4 has 0.0312 eV for electro-optic energy and the built-in electric field is 66.756 kV/cm; while sample 1:2 provides 0.0277 eV and 55.9858 kV/cm for electro-optic energy and built-in electric field, respectively. For the sample 1:5, the results are 0.0213 eV and 37.6261 kV/cm.

5.1.3.2 $Al_{0.3}Ga_{0.7}As$

Since GaAs shows FKO, then it is anticipated that the same ocillations $Al_{0.3}Ga_{0.7}As$ also takes place in this material. From figure 5.3, it is hard to observe FKO of $Al_{0.3}Ga_{0.7}As$ due to small intensity of PR amplitude. A high probability of small intensity is caused by thickness of $Al_{0.3}Ga_{0.7}As$ which is very thin compared to GaAs. Regarding the doping concentrations, both p- and n- doped between GaAs and $Al_{0.3}Ga_{0.7}As$ do not show too much

difference, although the concentration for GaAs is slightly higher than $Al_{0.3}Ga_{0.7}As$. The same phenomenon also discovered by Pan et al., where the low intensity of the AlGaAs bandgap energy at 1.7 eV was reported [66]. Pan et al. found that the factor determining the presence of the FK intensity lies in the number of doping concentration. The heavier the doping is, the more probable that the FKO appear. Complete etching in the substrate containing more doped concentrations eliminate the oscillations and also the reduction intensity of its lineshape, therefore giving rise to the the sharp features of the substrate below the material being etched [66].

5.1.4 GaAs and Wetting Layer

The energy bandgap of GaAs, which lies in 1.42 eV theoretically, has been proved that the strongest feature also established in the vicinity of 1.42 eV. The energy bandgap for GaAs of sample 1:1, 1:2, 1:3, 1:4 and 1:5 are 1.429 eV, 1.439 eV, 1.425 eV, 1.425 eV and 1.418 eV (see figure 5.10), respectively. Sample 1:2 indicates abnormal energy bandgap position of GaAs, since it shows the most deviated compared to another sample in series 1.

The reference solar cell (1:5) does not have extra peak standing lower to the GaAs substrate energy, like in another sample which possess QDs. This extra peak is called the WL (figure 5.10). Its shape is Gaussian-like shape, due to their confined QW nature (figure **??**). It introduces continuum density of states from its own energy level up to the CB and hence becomes a problem, since it has potential to disturb discrete confinement for carriers, which is from the nature of QDs. The 0-density of states between confined states and the CB lowers the probability of the quick relaxation of carriers [46]. The effect of the WL in the IBSC has been proven [10]. The QDs IBSC with WL lowers performance compared to the QDS IBSC without WL [10].

The WL is an initial layer of atoms grown epitaxially serving as basis where QDs are formed. In the electronic structure point of view, this thin layer is imagined as an ultranarrow rectangularlike QW [46]. The WL in the QDs causes two major changes: modification of the confinement potential and some influence on the intermixing degree of the WL [67]. The intermixing which is exploited in the experimental spectra is the result of the superposition of several transitions. The WL energy (fitting using equation 4.6) for the sample 1:1, 1:2, 1:3 and 1:4 are 1.343 eV (Γ=14.24 meV), 1.329 eV (Γ=21.13 meV) - 1.388 eV (Γ=44.49 meV), 1.349 eV (Γ=8.419 meV) - 1.366 eV (Γ=19.48 meV) and 1.349 eV (Γ=10.52 meV) - 1.37 eV (Γ=12.28 meV) as it is given in figure 5.10. There is a similarity of WL energy for the sample 1:1, 1:3 and 1:4, which is around 1.34 ± 1 eV, but not for sample 1:2. The deviation of the WL energy is influenced by the imperfect uniform local density of the QDs, implying to the difference in the distance to the nearest dot [67]. Judging from the energy position, The WL is supposed to be composed of $In_{0.07}Ga_{0.93}As$, which possess energy bandgap of 1.3458 eV. Overall, the results of the GaAs bandgap and WL position energy is similar according to [46].

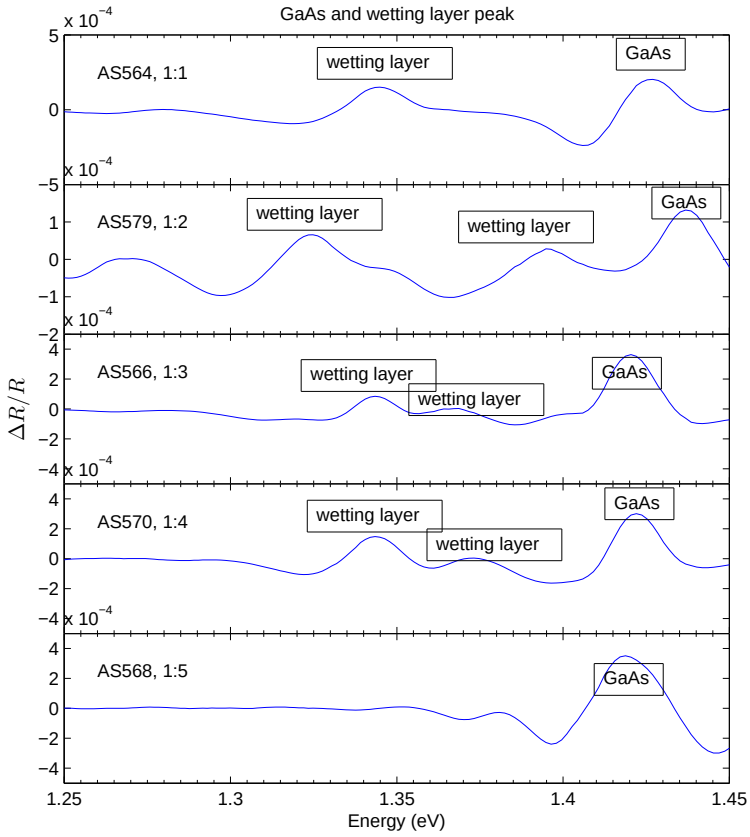

Figure 5.10: GaAs peak and WL of sample 1:1 through 1:5.

5.1.5 Quantum Dots

QDs fabrication employs Stranski-Krastanov method, utilizing the elastic energy when two materials with a large lattice mismatch from an epitaxial structure [67]. This method forms defect free islands since the local curvature close to surface region in the vicinity of the island serve to elastically deform the island and WL, reducing the accumulated strain. In the PR, preliminary method to distinguish QDs defined by the overlapping of the wave-functions adopting the oscillatory shape (free movement of the carriers through the bands generated by the dots). The difficulty found in here is the mixed feature of one to another whether the shape is oscillatory or gaussian. The method to determine whether it is gaussian or oscillatory can be done by comparing the PR spectrum versus its modulus. If the they do not maintain the same shape, so it has oscillatory behavior, like QDs. In other hand, if it maintains the same shape, it has gaussian features [46].

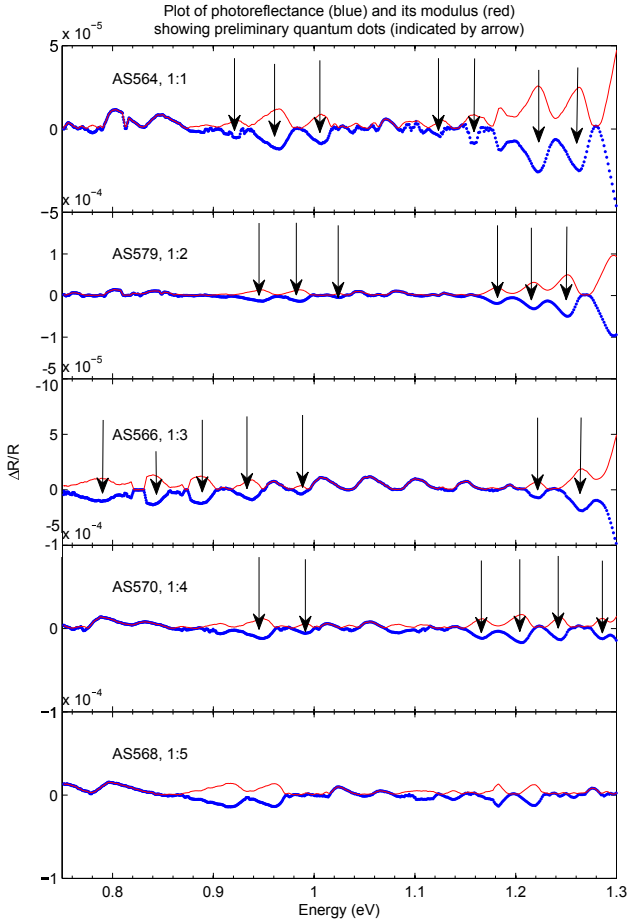

Figure 5.11: Preliminary method to determine QDs. PR spectrum with its modulus, showing QDs sample 1:1 through 1:5.

As given in figure 5.11, sample 1:1 to sample 1:4 show number of QDs, as expected. The reference solar cell, shows similar shape giving rise to a conclusion that there are several QDs in this sample. The QDs represents the transition in the intersubband (intraband). This is true for the sample 1:1 up to 1:4, but not expected for sample 1:5. Oscillations observed in sample 1:5 are part of the interference (section 5.1.6.3). Sample 1:1 and 1:2 show almost similar QDs energy one toward another, while sample 1:3 and 1:4 show similar behavior. Those two pairs of the samples share similar processing condition. Sample 1:1 and 1:2 have 470°C of Reell temperature, 586°C of barrier temperature with ratio of In:As_2 = 1:9. The only difference is the number of layers, which are 5 layers for 1:1 and 20 layers for 1:2. The same condition for sample 1:3 and 1:4, which has 520°C of Reell

temperature, 586°C of barrier temperature. The only difference lies in the ratio of In:As_2, 1:9 for sample 1:3 and 1:37 for sample 1:4.

Based on figure 5.11 and first derivative lorentzian lineshape (equation 4.6), we can estimate and conclude the QDs energy location for sample 1:1 to 1:4, given in table 5.2.

Table 5.2: Experimental PR energy peaks for InAs/GaAs QDs

Peak	1:1 (eV), Γ (meV)	1:2 (eV), Γ (meV)	1:3 (eV), Γ (meV)	1:4 (eV), Γ (meV)
QD4	1.273, 25.72	1.254, 35.79	1.235, 82.72	1.292, 31.16
QD3	1.225, 25.61	1.227, 31.45	1.22, 21.43	1.243, 24.88
QD2	1.179, 6.357	1.178, 14.58	–	1.198, 45.22
QD1	1.164, 45.05	–	–	1.153, 35.47
Defect	1.014, 42.79	1.027, 10.92	–	–

Ground state of QD for sample 1:1 to 1:4 is varying one to each other. Sample 1:1, 1:2, 1:3 and 1:4 indicate that the QD ground state transition are located in 1.164 eV, 1.178 eV, 1.22 eV and 1.153 eV, respectively. Besides transition in ground state, PR result also shows higher state transition of QDs, also called QDs excited states, in each sample. Each sample exhibits different transition energy of excited states. The excited states of the QDs, which are detrimental for the QD-IBSC performance, are not readily observed by PL [10].

Not all predicted QDs transition which are presented in figure 5.11 are correct. Generally, there are no QDs energy transition below 1 eV. It has been proved by Cánovas et al. [46]. A defect identified in the energy location around 1.014-1.027 eV, close to the experimental result of Cánovas et al., which is 1.05 eV and theoretically found by Kaniewska et al. at 1.03 eV. Most QDs transition found in sample 1:1 and 1:4. As the additional from the result of Cánovas et al., another transition at the energy higher than 1.22 eV are observed. Variation of energy transitions are met in different sample, reflecting different defect contained in each of the sample. The deviation of the QDs energy location exposed in sample 1:4 with the high QDs size, implying that it has most defect among all samples.

There are no QDs deposited in sample 1:5, but only i-GaAs layer. The n-layer substrates are Si-doped and it might have Cu impurities, also p-layer substrates doped with Be. These dopants and impurities result might the reason of the oscillatory shape. Another probability is the optical transitions in i-GaAs, i.e. intersubband transitions and involving Ga and As point defects, such as vacancy.

The capping layer will determine the electronic properties of QDs, strongly influenced by the strain-driven partial decomposition which increases the effective QDs size (as the concentration of capping layer, for example indium in $In_xGa_{1-x}As$, increasing). It will contribute to the observed low-energy shift of the QDs ground state transition [69].

5.1.6 Sample 1:2 And Sample 1:5

5.1.6.1 Characteristics of Sample 1:2

Sample 1:2 and 1:4 hold different parameter in terms of number of layers and ratio between In to As_2, respectively. For sample 1:2, it has 20 layers, while 1:4 has ratio of In:As_2 of

1:37 (The ratio means that the QDs size are much larger compared to ratio of 1:9). The other parameters are similar with the reference cell. The sample 1:2 with the more layers has smaller value of electro-optic energy and built-in electric field than the sample 1:4 with the higher ratio of In:As_2. As proven by Thomassen, sample 1:2 shows the overall lowest EQE compared to other samples [10]. This indicates formation of extended defects due to strain relaxation, even though the EQE is slightly higher in 880-1010 nm.

Compared to another sample, 1:2 has several strong oscillations before the substrate energy bandgap extending from 1.17-1.4, as depicted in figure 5.12,

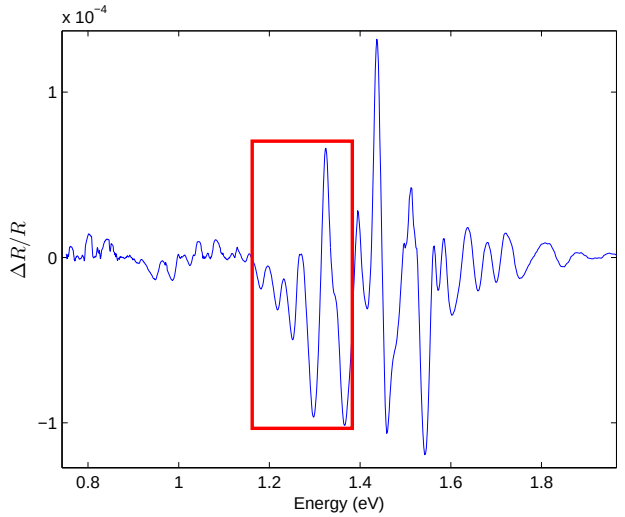

Figure 5.12: Strong oscillations in sample 1:2, below GaAs energy bandgap.

The prominent oscillations in figure 5.12 are identified as the existence of WL formation by QW in the upper layer, with no QDs developed in this layer [10]. The presence of the QD improves the electro-optic energy and built-in electric field, as we can see from the lowest value of those values in the reference cell, which does not possess QD. The fact of the low values of electro-optic energy and built-in electric field in sample 1:2 shows the number of QDs in this sample are smaller compared to another sample containing QDs.

This sample has the most shifted energy bandgap E_g of GaAs (1.439 eV) together with highest broadening parameter Γ (39.21 meV) among other samples. Regarding the FKO fitting showed in the sample 1:2 (see figure 5.6), it has low correlation of the calculation of electro-optic energy compared to the fitted electro-optic energy. The calculation shows the electro-optic energy at 0.0277 eV, while the fitted holds electro-optic energy of 0.03657 eV. This range is too wide if it compared with other samples. It shows that 20 layers composition have more domination of the interference effect, which is more prominent in the multilayer structure of QDs compared to the less layer structure. Multi-reflectance process is also accounted in addition, which is more vocal for the 20 layers than 5 layers. Interference effect, including constructice and destructive interference, along with the multi-reflectance derived from multi-interface of the sample structure give rise to the

observed PR spectrum like what we have in the experimental part.

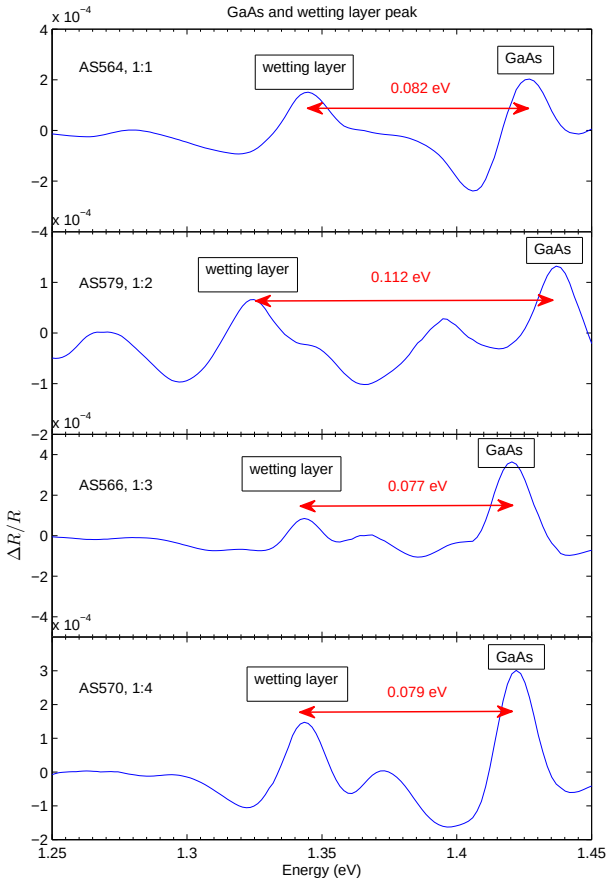

Figure 5.13: Strong oscillations in sample 1:2, below GaAs energy bandgap.

Let us discuss about the existence of the WL position in sample 1:1, 1:2, 1:3 and 1:4 (see figure 5.13). The peak for each sample is 1.345 eV, 1.325 eV, 1.343 eV and 1.343 eV, respectively. If we make a connection with the energy substrate of GaAs, then 1.427 eV, 1.437 eV, 1.42 eV, 1.422 eV and 1.419 eV corresponding to the 1:1, 1:2, 1:3 and 1:4, respectively and from this data, we can calculate the difference of energy between WL and energy substrate of GaAs.

We can see that 1:2 makes the farthest distance relative to the energy substrate of GaAs, followed by relatively the same in 1:1, 1:4 and 1:3. Based on the Thomassen result, 1:2 has the highest V_{oc} compared to the other samples. PR then, can solve shifting phenomena in WL which is not able to be solved in PL and EQE [10].

5.1.6.2 Band Structure of Sample 1:5

The band structure for the reference solar cell is depicted in figure 5.14. No QW observed from the figure 5.14, as expected from the reference solar cell, which is also applied to another sample. QW is formed when the smaller bandgap lies between the bigger bandgap (figure 2.1). This feature does not meet in the reference solar cell. The first example of this structure is GaAs/In_xGa_xAs/GaAs, with the content of In of 0.5. The energy bandgap for GaAs is 1.42 eV, while energy bandgap for $In_{0.5}Ga_{0.5}As$ is 0.89 eV [58]. When they are aligned, the InGaAs will form deep well between GaAs material [29]. Another material composing QW has been described by Misiewicz and Kudrawiec [4]. The arrangement of the QW originally comes from $Ga_{0.78}In_{0.28}N_xAs_{1-x}$/GaAs.

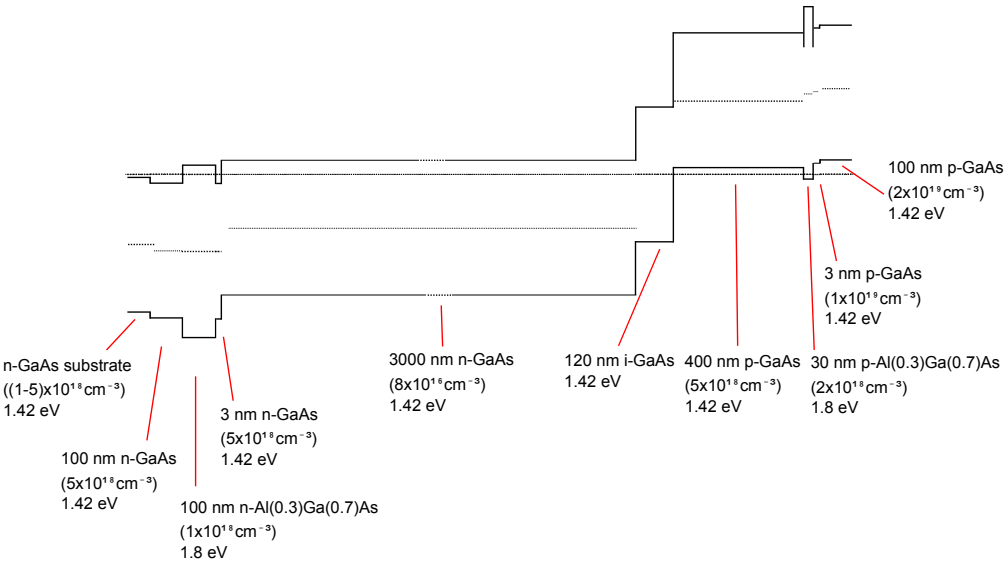

Figure 5.14: Band structure of the sample 1:5 (reference cell).

One method to extract the transition energies of QDs and WL is using fitting of the first derivative lorentzian lineshape. This fitting shows inhomogeneously broadened PR features for confined transitions [70]. The line shape nature and temperature independence of the linewidths of the QDs and WL indicate that the broadening is due to fluctuations in the QDs size and WL thickness of the nanostructures [71].

5.1.6.3 Oscillation Below 1.42 eV in Sample 1:5

It is detected earlier that in the region below 1.42 eV, there are oscillations dominating the energy lower than GaAs bandgap shown in figure 5.15.
Figure 5.15 tells that there are strong interference of secondary light beam reflected from different interfaces of the sample, and it is dominated from the Si-substrate/epilayer rather than GaAs/AlGaAs interfaces. Huang et al. did a research where they etched the substrate and the result of the etching showed that the mixtures region in the range of 1.45 eV-1.77

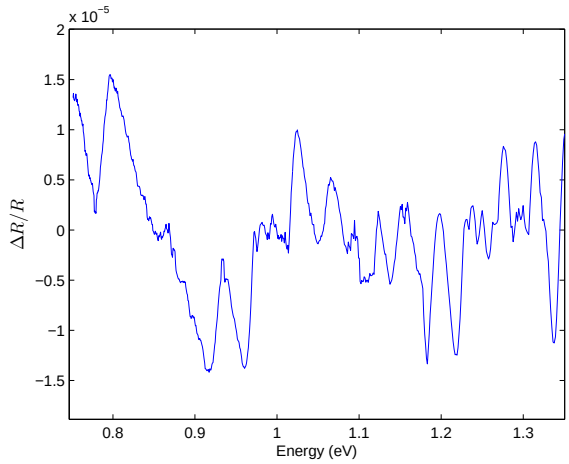

Figure 5.15: Oscillations region in the lower energy of GaAs bandgap in the sample 1:5.

eV were disappeared, but the oscillation with the energy lower than 1.424 eV are still present, but with longer period [72]. This finding agrees with Pan et al. and Kallergi et al. [66, 73]. Huang et al. showed that the oscillations are more likely happened to the Si-doped GaAs rather than Cr-doped (semi-insulating) [72]. It means that these circumstances are related to the Si-doped GaAs substrate and the epilayer interface. The oscillation effect is raised in the form of interference between two reflected beam, one from the sample surface and the other from the substrate/epilayer interface [72].

As we know from the principle of the electro-optic effect, where the modulation of electric field gives rise to the change in dielectric constant, which is also affecting the change in refractive index, this knowledge becomes aid in understanding the interference lineshape. In the modulation process of the sample, the oscillation features are aroused due to the additional generation of carriers by the modulated pump beam. This is where contactless electroreflectance excels in, where it does not generate extra carriers so that it avoids giving rise to interference effect [8, 74]. Besides interference, another possible cause for this oscillations is band filling of impurity states, if we consider our samples to be heavily doped (10^{19} cm^{-3}). The absorption spectrum of heavily doped semiconductor shows a tail in the energy range below GaAs bandgap. The tail is related to density of impurity states and depends strongly on the doping concentration. Regardless of this complication, interference oscillations can lead to the epilayer thickness and refractive index information [72, 74].

Controlling the oscillation features magnitude can be achieved by maintaining external parameters in the PR experiment, such as temperature, wavelength, frequency of modulated beam, the phase of the lock-in detection, and additional illumination of the sample. Using shorter wavelength of modulated beam can reduce the intensity of oscillation features [8], as well as exploits QW features which are not appear in the longer wavelength modulation [74]. The strength of ΔR is determined by how much the dielectric constant affected by the modulation. A short wavelength laser (532 nm, for example) has more

strongly absorbed and all layers are modulated. Long wavelength modulation source (980 nm, for example) makes layers to have lower absorption ability ($< 2\ \%$), and as a result, the SNR of the PR is very low. In the other hand, shorter wavelength laser (400 nm, for example) is able to suppress the oscillation features in the low energy, but features at higher energy is not observable since most of the excited electron will transfer its energy to thermal (non-radiative). The reduction in oscillation features are triggered by reduction of the penetration depth, as a consequence of lower wavelength, thus substrate region is much less modulated [74].

5.1.7 General Features

The defect quality mentioned by Thomassen for sample 1:1 and sample 1:3, the PR result also shows similar occurrence about this evident [10]. Sample 1:3 has higher amplitude compared to the sample 1:1, and also we can clearly see the oscillations in low energy ($<$ 1.2 eV) for sample 1:3 rather than vague oscillation in the 1:1. EQE, V_{oc} and I_{sc} for 1:3 and 1:4 are similar due to the same growth condition and only differs in the ratio of In:As_2 that prevents the formation of large-sized QDs in 1:3 [10], but the electro-optic energy and built-in electric field is lower for 1:4 compared to the 1:3 because of the occupancy of the WL instead of the QDs which are formed in the upper layer resulting less number of QDs in 1:4 compared to 1:3.

5.1.8 Factors In Photoreflectance Spectroscopy

5.1.8.1 Angle of incidence

The incidence angle has some physical effect on the sample result of PR measurement. This factor is a useful technique to probe the microstructure [75]. Since refractive index of air is smaller than the GaAs [37], we have external reflection in this work. For this experiment, approximately 60° is chosen due to the Brewster angle features [75], where the transverse electric is mostly reflected from the material, while transverse magnetic transmitted into the material [9].

5.1.8.2 Interference effects

PR technique is indeed a sensitive method to characterize the material, and its advantages are nondestructive nature and producing sharp features in the energy range near the critical points in the Brillouin zone. This technique does not need special mounting or preparation and it can be done at room temperature. The only problem is located on the high sensitivity features giving rise to difficulty in analyzing observed spectra, especially for multilayered structures such as heterostructures. The complexity arises in term of possibility in finding subband transitions in QWs, excitonic effects, FKO, impurity effects, miniband dispersion in coupled QWs and transitions associated with unconfined states [72, 75].

Interferences usually take place in the semiconductor microstructures consisting of number of multilayers. There is a report on oscillations in the PR spectrum in the energy range below the band gap of GaAs on samples of GaAs/AlGaAs [72–75]. The oscillation is affiliated with the interference effect of reflected light from different interfaces of the

sample. This phenomenon itself distorts the PR lineshape, i.e. deforms information of bulk semiconductors, especially at the low-energy region. The interference does not change the FKO period. The effects of interferences in the heterojunction interfaces can be studied by reflectance [66].

Manifestation of interference effect is translated in the form of contribution to dielectric constant alteration. For bulk and uniform material, the Seraphin coefficient for imaginary part is almost zero at the fundamental gap. But it does not prevail for semiconductor multilayer microstructure, where the interference effect takes over the value of imaginary part Seraphin coefficient to become non-zero. This effect is more profound in microstructures with the protective layer cladding [5].

5.2 Photoluminescence

5.2.1 Oscillation Below 1.42 eV in Sample 1:5

This section will focus on the PL measurement of sample 1:5 especially in the range below GaAs energy gap, where unintended oscillations are found. Though it has been discussed in the section 5.1.6.3, we will see this issue from PL perspective.

A signal detected below the GaAs substrate is classified as a defect. Usually, the signal exhibits a Gaussian lineshape, the same lineshape for the QDs and QWs (WL). The defect band and defect level recombination have been identified close to CB [76]. Defects and defects complexes formation occurred in the heavily doped GaAs, usually contains $> 10^{18}\text{cm}^{-3}$ of high dopant concentrations. In the sample 1:5, there are several heavily doped GaAs layer formed in the sample and due to this fact, defect is expected in the energy lower than GaAs energy bandgap. There are two defects complexes: Si-X (silicon-at-arsenic and gallium vacancy-stabilized by an arsenic antisite) and Si-Y (silicon substituting for a gallium and gallium vacancy second-nearest neighbor). It is known that Si-Y exhibits defects complex in deep level, which gives rise to PL band near 1.2 eV, and occurred for the GaAs doped with silicon as well. The defect identification in the subband gap PL emission near 1.2 eV as stemming from a vacancy related Si-Y complex. The defect of the sample 1:5 in 1.2 eV is shown in figure 5.15. The presence of the defect energy level makes the interaction of the electron-hole pair with the defect energy state more favorable leading to the Gaussian lineshape function [76], as it shown in the PR spectra.

5.2.2 Photoluminescence Measurement and Analysis on Sample 1:1

The PL experimental setups are described as follows,

- Excitation
    1. Wavelength: 520 nm-800 nm (IHR320)
    2. Increment of 20 nm
    3. Side entrance slit: 10 nm
    4. Front exit slit: 10 nm

5. Side exit slit: 10 nm
6. Grating: Density 1200 (Blaze: 330)

- Emission

1. Wavelength: 700 nm-1500 nm (IHR320)
2. Increment of 2 nm
3. Side entrance slit: 10 nm
4. Front exit slit: 10 nm
5. Side exit slit: 10 nm
6. Grating: Density 600 (Blaze: 1000)

- Detector: T1 (DSS-IGA020L) (SCD3)

Slit is opened wider to support high SNR. It is proven by the peak which is able to notice when the slit with the width of 10 nm compared to the slit width of 5 nm. Filter utilized in this experiment is the filter with wavelength of 865 nm, and this filter can accommodate higher diffraction order blocking in 1730 nm. The PL measurements are conducted in the room-temperature. The effect is the contribution of phonon towards the PL spectra. That is why it is better done in low temperature (6 K) in order to suppress phonon effect. Physically, phonon spectrum makes interested sharp spectra to have broader full width half maximum (FWHM). WL will not be well-resolved in this spectra1 due to the phonon making broadening and also small intensity so that it will be hard to see. QDs appear around 1.127 eV [77]. Another peak appear probably indicate doped Be material and some other materials such as Si, C or Cu. The results of the PL for sample 1:1 are described in figure 5.16: (Other results are give in appendix C)

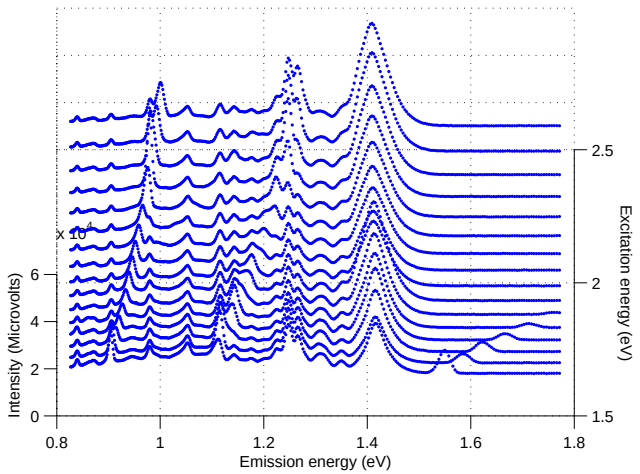

Figure 5.16: PL of sample 1:1 at x-y plane, at room temperature.

There are several peaks noticed from the measurement, and we will separate each part for the specific discussion. The GaAs energy transition is described at 1.409 eV in the high excitation energy and the energy transition of GaAs is increased up to 1.416 eV as the excitation energy is lowered with FWHM of 61 meV and 34 meV, respectively. Overall, the GaAs energy bandgap stays in their place as the excitation energy changes.

Several peaks observed in the excitation energy of 1.55 eV, 1.59 eV, 1.632 eV, 1.676 eV and 1.722 eV corresponding to the emission energy of 1.55 eV, 1.586 eV, 1.623 eV, 1.667 eV and 1.713 eV, respectively. If we look closely, the peaks occur when the excitation energy falls at the same energy as the emission energy. These peaks indicate as a Rayleigh scattering.

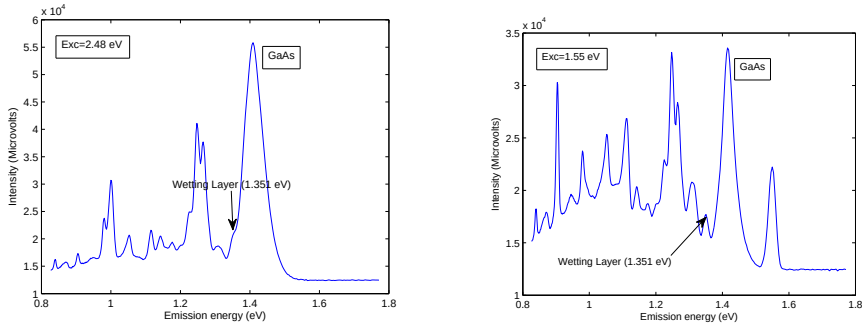

(a) Excitation energy at 2.48 eV

(b) Excitation energy at 1.55 eV.

Figure 5.17: Comparison of two excitation energy in the sample 1:1 PL measurement.

WL is found in 1.351 eV. WL position is more visible in the low excitation energy, i.e. resolved peak (5.17b), while in the higher energy excitation (e.g. 2.385 eV and above), the peak of the WL is not resolved (5.17a). The position of the WL is independent of the excitation energy. The finding of WL in PL measurement shows closeness in PR measurement, which is 1.343 eV. Compared to PR result (figure 5.10), WL identified in PL has much lower signal with respect to GaAs signal, which can be potentially difficult to analyze. Since we have PL in room temperature, phonon actively plays role in the PL spectrum, which makes the interested spectrum becomes wider, lowers the intensity and results in restraining other interesting feature, and in this case in the WL. Thomassen found the WL in the 2 K PL is well-resolved, and it is located in the around 1.3478 eV [10].

The energy bandgap of the material depends on the temperature where the material being held. Each material has their own energy band gap in relation with the temperature. The relation from the Varshni relation [78],

$$E_g(T) = E_0 - \frac{\alpha T^2}{T + \beta} \tag{5.5}$$

$E_g(T)$ is the energy band gap as a function of temperature, E_0 is the energy bandgap at 0 K, α and β are fitting parameter, while T is the desired temperature. The calculation result for Si, Ge, GaAs, AlAs, InAs, InP and GaP shows that the difference between E_g(0 K) and E_g(300 K) is around 0.1 eV lower for higher temperature (300 K) [79, 80].

Sample 1:1 is doped with Be (p-GaAs), Ashen et al. reveals lines of BE, carbon acceptor lines and Be acceptors on As site at 1.514, 1.490 and 1.493 eV, respectively [81]. While Künzel and Ploog determines peak at 1.485 eV in conjunction with Si acceptors on As site. Another peak found by Takamori et al. related to Cu and its phonon replicas (phonon coupling to the FE transitions [84]) are observed at 1.36 and 1.32 eV [83]. Based on this information, we can make approximation of the energy bandgap in our sample:

- GaAs : 1.424 eV
- C : 1.39 eV
- Be : 1.393 eV
- Si : 1.385 eV
- Cu and its phonon replicas : 1.26 eV and 1.22 eV

The final identification for sample 1:1 is therefore shown in figure 5.18, at the excitation of 2.48 eV and 1.55 eV are given in figure 5.18a and 5.18b, respectively.

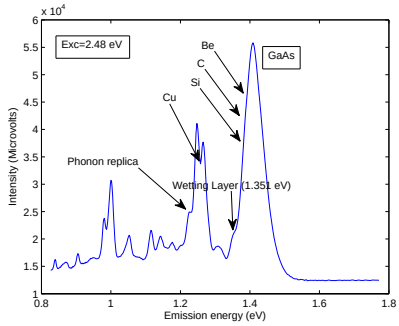

(a) Excitation energy at 2.48 eV

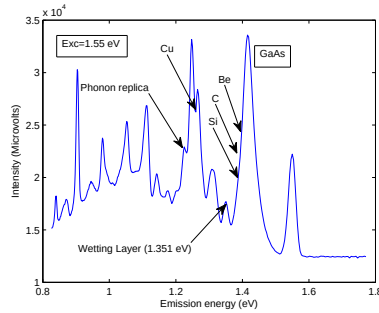

(b) Excitation energy at 1.55 eV.

Figure 5.18: Complete identification of two excitation energy in the sample 1:1 PL measurement.

Chapter 6

Outlook

The current monochromator is Bentham TM300V. The only drawback of PR is influence of unwanted luminescence from the sample and/or scattered light from pump source in PR spectrum. This spurious signal can be suppressed with the second monochromator [20], and we can utilize a new iHR550 Jobin Yvon in the lab.

There is a space between concave mirror with the focal point of 50 cm and sample, which is not used in this work. This space can be filled with the polarizer, so that there is a freedom in controlling the incoming polarization state of probe beam. Alongside with the polarizer, the goniometer also can be used to adjust the angle of incidence of probe beam and therefore becomes an alternative to modify whether the sample reflecting transverse electric or transverse magnetic.

The beam expander for the modulation source need to be adjusted so that it makes modulation spot to have the same size as focused spot from probe beam in sample, in order to make the modulation process becomes more effective. In the current setup, the laser spot is still smaller than the probe beam spot in the sample, indicating that there are area in the sample which are not completely modulated. Another perspective to solve this issue is by employing tunable laser source instead of broadband probe beam to achieve small spot with adjustable wavelength.

Inspecting wider bandgap material is achieved by using lower wavelength modulation source. Another advantage is its ability to suppress the oscillation features in the low energy.

Chapter 7

Conclusion

Optical characterization of InAs/GaAs QD-IBSC has been carried out by using PR and PL techniques. Development of PR setup is successfully conducted in delivering light from the exit slit of monochromator to the sample with minimal loss of light intensity by using OAP 15° and 90° along with concave mirror of 50 cm focal point. The resulting system has a flux enhancement, noise reduction as well as increased wavelength resolution.

Implementation of the mathematical models of the PR signal has been done in performing quantitative curve fitting. Electro-optic energy and built-in electric field have been recognized, which is later leading to the Airy function plotting that is able to explain FKO in the intermediate-range regime as the response to the applied electric field modulation. The first derivative lorentzian lineshape function has been employed to fit lineshape of confined structure.

PR measurement on the IBSC samples have been done. The spectra of this measurement gives rise to several recognizable peaks for all samples in which they share similarity and are also distinct from each other, due to their varied characteristcs. The FKO, as a result of electro-optic effect, are observed and the fitting are done by using Airy function. These oscillations can be used to determine electro-optic energy and the built-in electric field. Energy bandgap of $Al_{0.3}Ga_{0.7}As$, GaAs, WL and QDs are resolved using first derivative Lorentzian lineshape function.

To complement PR findings, PL measurements for a wide range of excitation energies are conducted at room-temperature. Oscillations in the low energy range shown by reference cell indicate defect transitions in the sample. The energy bandgap of WL is identified in the low PL excitation energy. The spectrum indicates low signal of WL with respect to GaAs. The possible reason for this phenomenon is the contribution of phonon in room-temperature. QDs, B, C and Si are not resolvable due to the same reason.

Bibliography

[1] D.E. Aspnes. Third-derivative modulation spectroscopy with low-field electroreflectance. *Surface Science*, 37(0):418 – 442, 1973. ISSN 0039-6028. doi: http://dx.doi.org/10.1016/0039-6028(73)90337-3. URL http://www.sciencedirect.com/science/article/pii/0039602873903373.

[2] Fred H. Pollak. Study of semiconductor surfaces and interfaces using electromodulation. *Surface and Interface Analysis*, 31(10):938–953, 2001. ISSN 1096-9918. doi: 10.1002/sia.1131. URL http://dx.doi.org/10.1002/sia.1131.

[3] A. H. Rodríguez, C. Trallero-Giner, Martín Muñoz, and María C. Tamargo. Electroreflectance spectroscopy in self-assembled quantum dots: lens symmetry. *Phys. Rev. B*, 72:045304, Jul 2005. doi: 10.1103/PhysRevB.72.045304. URL http://link.aps.org/doi/10.1103/PhysRevB.72.045304.

[4] J. Misiewicz and R. Kudrawiec. Contactless electroreflectance spectroscopy of optical transitions in low dimensional semiconductor structures. *Opto-Electronics Review*, 20(2):101–119, 2012. ISSN 1230-3402. doi: 10.2478/s11772-012-0022-1. URL http://dx.doi.org/10.2478/s11772-012-0022-1.

[5] Fred H. Pollak and H. Shen. Modulation spectroscopy of semiconductors: bulk/thin film, microstructures, surfaces/interfaces and devices. *Materials Science and Engineering: R: Reports*, 10(78):xv – 374, 1993. ISSN 0927-796X. doi: http://dx.doi.org/10.1016/0927-796X(93)90004-M. URL http://www.sciencedirect.com/science/article/pii/0927796X9390004M.

[6] X. L. Zheng, D. Heiman, B. Lax, and F. A. Chambers. Reflectance line shapes from GaAs/$Ga_{1-x}Al_xAs$ quantum well structures. *Applied Physics Letters*, 52(4):287–289, 1988. doi: 10.1063/1.99496. URL http://link.aip.org/link/?APL/52/287/1.

[7] J. P. Estrera, W. M. Duncan, and R. Glosser. Complex airy analysis of photoreflectance spectra for III-V semiconductors. *Phys. Rev. B*, 49:7281–7294, Mar 1994. doi: 10.1103/PhysRevB.49.7281. URL http://link.aps.org/doi/10.1103/PhysRevB.49.7281.

[8] R. Kudrawiec, P. Sitarek, J. Misiewicz, S. R. Bank, H. B. Yuen, M. A. Wistey, and Jr. James S. Harris. Interference effects in electromodulation spectroscopy applied to

gaas-based structures: A comparison of photoreflectance and contactless electroreflectance. *Applied Physics Letters*, 86(9):091115, 2005. doi: 10.1063/1.1873052. URL http://link.aip.org/link/?APL/86/091115/1.

[9] B.E.A. Saleh and M.C. Teich. *Fundamentals of Photonics*. Wiley, 2007.

[10] Sedsel Fretheim Thomassen. *InAs/(Al)GaAs quantum dots for intermediate band solar cells*. PhD thesis, 2012.

[11] Antonio Luque and Antonio Martí. Increasing the efficiency of ideal solar cells by photon induced transitions at intermediate levels. *Phys. Rev. Lett.*, 78:5014–5017, Jun 1997. doi: 10.1103/PhysRevLett.78.5014. URL http://link.aps.org/doi/10.1103/PhysRevLett.78.5014.

[12] J. Dalfors, Universitetet i Linköping. Department of Physics, and Measurement Technology. *Photoluminescence Studies of the Electronic Structure in Some III-V Quantum Structures*. PhD thesis, Linköpings Universitet, 1999.

[13] R. Hanson, L. P. Kouwenhoven, J. R. Petta, S. Tarucha, and L. M. K. Vandersypen. Spins in few-electron quantum dots. *Rev. Mod. Phys.*, 79:1217–1265, Oct 2007. doi: 10.1103/RevModPhys.79.1217. URL http://link.aps.org/doi/10.1103/RevModPhys.79.1217.

[14] Dordrecht, 1997. Kluwer, Kluwer.

[15] E. H. Sargent. Infrared quantum dots. *Advanced Materials*, 17(5):515–522, 2005. ISSN 1521-4095. doi: 10.1002/adma.200401552. URL http://dx.doi.org/10.1002/adma.200401552.

[16] C. Kittel. *Introduction to Solid State Physics*. Wiley, 2004.

[17] J. R. Haynes. Experimental proof of the existence of a new electronic complex in silicon. *Phys. Rev. Lett.*, 4:361–363, Apr 1960. doi: 10.1103/PhysRevLett.4.361. URL http://link.aps.org/doi/10.1103/PhysRevLett.4.361.

[18] R. Dingle, H.L. Strmer, A.C. Gossard, and W. Wiegmann. Electronic properties of the GaAs-AlGaAs interface with applications to multi-interface heterojunction superlattices. *Surface Science*, 98(13):90 – 100, 1980. ISSN 0039-6028. doi: http://dx.doi.org/10.1016/0039-6028(80)90478-1. URL http://www.sciencedirect.com/science/article/pii/0039602880904781.

[19] Antonio Marti, L. Cuadra, and Antonio Luque. Partial filling of a quantum dot intermediate band for solar cells. *Electron Devices, IEEE Transactions on*, 48(10):2394–2399, 2001. ISSN 0018-9383. doi: 10.1109/16.954482.

[20] J. Misiewicz, P. Sitarek, G. Sek, and R. Kudrawiec. Semiconductor heterostructures and devices structures investigated by photoreflectance spectroscopy. *Material Science*, 21(3):263–320, 2003. URL http://materialsscience.pwr.wroc.pl/bi/vol21no3/articles/ms_2003_015.pdf.

[21] J. Misiewicz, K. Jezierski, P. Sitarek, P. Markiewicz, R. Korbutowicz, M. Panek, B. ciana, and M. Taczaa. Photoreflectance characterisation of GaAs and GaAs/GaAlAs structures grown by MOCVD. *Advanced Materials for Optics and Electronics*, 5(6):321–327, 1995. ISSN 1099-0712. doi: 10.1002/amo.860050605. URL http://dx.doi.org/10.1002/amo.860050605.

[22] X. L. Zheng, D. Helman, B. Lax, and F. A. Chambers. Photoreflectance and the seraphin coefficients in quantum well structures. pages 43–47, 1988. doi: 10.1117/12.947411. URL +http://dx.doi.org/10.1117/12.947411.

[23] Hideo Wada, K. Eriguchi, Akira Fujimoto, T. Kanashima, and Masanori Okuyama. Photoreflectance spectroscopic technique: a new model for estimation of plasma-induced defect density in Si substrate. In *Plasma Process-Induced Damage, 1998 3rd International Symposium on*, pages 152–155, 1998. doi: 10.1109/PPID.1998.725597.

[24] S. Monéger, A. Tabata, C. Bru, G. Guillot, A. Georgakilas, K. Zekentes, and G. Halkias. Room temperature photoreflectance as a powerful tool to characterize the crystalline quality of inalas layers grown on InP substrates. *Materials Science and Engineering: B*, 21(23):177 – 180, 1993. ISSN 0921-5107. doi: http://dx.doi.org/10.1016/0921-5107(93)90343-L. URL http://www.sciencedirect.com/science/article/pii/092151079390343L.

[25] T Miya, Y Terunuma, T Hosaka, and T Miyashita. Ultimate low-loss single-mode fiber at 1.55 μm. *Electronics Letters*, 15(4):106–108, 1979. ISSN 0013-5194. doi: {10.1049/el:19790077}.

[26] S. L. Tyan, M. L. Lee, Y. C. Wang, W. Y. Chou, and J. S. Hwang. Investigation of modulation-doped GaAs/AlGaAs single quantum well by photoreflectance. *Journal of Vacuum Science and Technology B: Microelectronics and Nanometer Structures*, 13(3):1010–1013, 1995. doi: 10.1116/1.587894. URL http://link.aip.org/link/?JVB/13/1010/1.

[27] C. F. Li, D. Y. Lin, Y. S. Huang, Y. F. Chen, and K. K. Tiong. Temperature dependence of quantized states in an $In_{0.86}Ga_{0.14}As_{0.3}P_{0.7}$/InP quantum well heterostructure. *Journal of Applied Physics*, 81(1):400–405, 1997. doi: 10.1063/1.364071. URL http://link.aip.org/link/?JAP/81/400/1.

[28] Y. C. Wang, S. L. Tyan, and Y. D. Juang. Photoreflectance and photoluminescence spectroscopy of the lattice-matched InGaAs/InAlAs single quantum well. *Journal of Applied Physics*, 92(2):920–926, 2002. doi: 10.1063/1.1487906. URL http://link.aip.org/link/?JAP/92/920/1.

[29] Avakyants L.P., Bokov P.Yu., Glazyrin E.V., Kazakov I.P., and Chervyakov A.V. Photoreflectance spectroscopy of electron-hole states in a graded-width GaAs/InGaAs/GaAs quantum well. *Semiconductors*, 45(3):320–324, 2011. ISSN 1063-7826. doi: 10.1134/S1063782611030043. URL http://dx.doi.org/10.1134/S1063782611030043.

[30] C.T. Huang, J.D. Wu, C.F. Liu, Y.S. Huang, C.T. Wan, Y.K. Su, and K.K. Tiong. Optical characterization of a strain-compensated $GaAs_{0.64}Sb_{0.36}/GaAs_{0.79}P_{0.21}$ quantum well structure grown by metal organic vapor phase epitaxy. *Materials Chemistry and Physics*, 134(23):797 – 802, 2012. ISSN 0254-0584. doi: http://dx.doi.org/10.1016/j.matchemphys.2012.03.071. URL http://www.sciencedirect.com/science/article/pii/S0254058412003215.

[31] D. E. Aspnes and A. A. Studna. Schottky-barrier electroreflectance: Application to GaAs. *Phys. Rev. B*, 7:4605–4625, May 1973. doi: 10.1103/PhysRevB.7.4605. URL http://link.aps.org/doi/10.1103/PhysRevB.7.4605.

[32] David E. Aspnes. Electric field effects on the dielectric constant of solids. *Phys. Rev.*, 153:972–982, Jan 1967. doi: 10.1103/PhysRev.153.972. URL http://link.aps.org/doi/10.1103/PhysRev.153.972.

[33] P. Shi-hong, W. Zhong-he, L. Yi, Z. Cun-zhou, Z. Xiao-chuan, J. Jian, and X. Gui-chang. Franz-Keldysh oscillation from the space charge region of MBE GaAs films. *Acta Physica Sinica*, 2:619–629, August 1993. doi: 10.1088/1004-423X/2/8/008.

[34] H. R. Philipp and H. Ehrenreich. Optical properties of semiconductors. *Phys. Rev.*, 129:1550–1560, Feb 1963. doi: 10.1103/PhysRev.129.1550. URL http://link.aps.org/doi/10.1103/PhysRev.129.1550.

[35] J. S. Blakemore. Semiconducting and other major properties of Gallium Arsenide. *Journal of Applied Physics*, 53(10):R123–R181, 1982. doi: 10.1063/1.331665. URL http://link.aip.org/link/?JAP/53/R123/1.

[36] D. E. Aspnes and A. A. Studna. Dielectric functions and optical parameters of Si, Ge, GaP, GaAs, GaSb, InP, InAs, and InSb from 1.5 to 6.0 ev. *Phys. Rev. B*, 27:985–1009, Jan 1983. doi: 10.1103/PhysRevB.27.985. URL http://link.aps.org/doi/10.1103/PhysRevB.27.985.

[37] D. E. Aspnes, S. M. Kelso, R. A. Logan, and R. Bhat. Optical properties of $Al_xGa_{1-x}As$. *Journal of Applied Physics*, 60(2):754–767, 1986. doi: 10.1063/1.337426. URL http://link.aip.org/link/?JAP/60/754/1.

[38] Robert E. Morrison. Reflectivity and optical constants of Indium Arsenide, Indium Antimonide, and Gallium Arsenide. *Phys. Rev.*, 124:1314–1317, Dec 1961. doi: 10.1103/PhysRev.124.1314. URL http://link.aps.org/doi/10.1103/PhysRev.124.1314.

[39] Sadao Adachi. Optical dispersion relations for GaP, GaAs, GaSb, InP, InAs, InsSb, $Al_xGa_{1-x}As$, and $In_{1-x}Ga_xAs_yP_{1-y}$. *Journal of Applied Physics*, 66(12):6030–6040, 1989. doi: 10.1063/1.343580. URL http://link.aip.org/link/?JAP/66/6030/1.

[40] Kjetil Hofstad. Instrument design of photoreflectance spectroscopy. Master's thesis, NTNU, 2010.

[41] Quartz tungsten halogen lamp spectrum. URL http://www.newport.com/Technical-Note-Simulation-of-Solar-Irradiation/411986/1033/content.aspx.

[42] Bentham TM300V datasheet, 1991.

[43] Silicon detector spectral response. URL http://www.hamamatsu.com/resources/pdf/ssd/s12158-01ct_kpin1084e01.pdf.

[44] InGaAs detector spectral response. URL http://www.hamamatsu.com/resources/pdf/ssd/g8605_series_kird1049e06.pdf.

[45] J. L. Shay. Photoreflectance line shape at the fundamental edge in ultrapure GaAs. *Phys. Rev. B*, 2:803–807, Aug 1970. doi: 10.1103/PhysRevB.2.803. URL http://link.aps.org/doi/10.1103/PhysRevB.2.803.

[46] E. Cánovas, A. Martí, N. López, E. Antolín, P.G. Linares, C.D. Farmer, C.R. Stanley, and A. Luque. Application of the photoreflectance technique to the characterization of quantum dot intermediate band materials for solar cells. *Thin Solid Films*, 516(20): 6943 – 6947, 2008. ISSN 0040-6090. doi: http://dx.doi.org/10.1016/j.tsf.2007.12.038. URL http://www.sciencedirect.com/science/article/pii/S0040609007020767. ¡ce:title¿Proceedings on Advanced Materials and Concepts for Photovoltaics {EMRS} 2007 Conference, Strasbourg, France¡/ce:title¿.

[47] Adriano Ghedina and Roberto Ragazzoni. Optimum configurations for two off–axis parabolae optical relay, 1997. URL http://dipastro.pd.astro.it/planets/tngproject/TechRep/rep62/node1.html#fig1.

[48] Off–axis parabolic mirrors definitions, . URL http://www.web-essentiel.com/05-ardop/wp-content/uploads/downloads/2012/03/Off_Axis_Parabolas.pdf.

[49] 50329al off–axis replicated parabolic mirror, . URL http://search.newport.com/?q=*&x2=sku&q2=50329AL.

[50] 1 inch 90° off–axis parabolic mirror, . URL http://www.thorlabs.com/newgrouppage9.cfm?objectgroup_id=5447.

[51] Off–axis prabolic mirror, . URL http://www.thorlabs.com/newgrouppage9.cfm?objectgroup_id=5447.

[52] 1 inch 15° off–axis parabolic mirror, . URL http://www.edmundoptics.com/optics/optical-mirrors/focusing-concave-mirrors/off-axis-parabolic-metal-mirrors/2307.

[53] Concave mirror f=50 cm and d=2 inch. URL http://search.newport.com/?q=*&x2=sku&q2=20DC1000AL.2.

[54] M Nowaczyk, G Sk, J Misiewicz, B ciana, D Radziewicz, and M Taczaa. Photoreflectance study of δ-doped semiconductor layers by a fast fourier transformation. *Thin Solid Films*, 380(12):243 – 245, 2000. ISSN 0040-6090. doi: http://dx.doi.org/10.1016/S0040-6090(00)01515-7. URL http://www.sciencedirect.com/science/article/pii/S0040609000015157.

[55] G. Sek, Jan Misiewicz, Maria Kaniewska, Kazimierz Reginski, and Jan Muszalski. GaAs/AlGaAs complex structures examined by photoreflectance spectroscopy. pages 137–140, 1997. doi: 10.1117/12.276212. URL +http://dx.doi.org/10.1117/12.276212.

[56] X. Yin, Fred H. Pollak, L. Pawlowicz, T. O'Neill, and M. Hafizi. Characterization of GaAs/$Ga_{1-x}Al_xAs$ heterojunction bipolar transistor structures using photoreflectance. *Applied Physics Letters*, 56(13):1278–1280, 1990. doi: 10.1063/1.102536. URL http://link.aip.org/link/?APL/56/1278/1.

[57] Y. S. Huang, H. Qiang, Fred H. Pollak, Johnson Lee, and B. Elman. Electroreflectance study of a symmetrically coupled GaAs/$Ga_{0.77}Al_{0.23}As$ double quantum well system. *Journal of Applied Physics*, 70(7):3808–3814, 1991. doi: 10.1063/1.349184. URL http://link.aip.org/link/?JAP/70/3808/1.

[58] Semiconductors database. URL http://www.ioffe.ru/SVA/NSM/Semicond/index.html.

[59] G. Sek, J. Misiewicz, and T. S. Cheng. Photoreflectance spectroscopy of low-dimensional gaas/algaas structures. *Advanced Materials for Optics and Electronics*, 7(5):241–247, 1997. ISSN 1099-0712. doi: 10.1002/(SICI)1099-0712(199709)7:5⟨241::AID-AMO312⟩3.0.CO;2-K. URL http://dx.doi.org/10.1002/(SICI)1099-0712(199709)7:5<241::AID-AMO312>3.0.CO;2-K.

[60] S.A. Dickey, A. Majerfeld, J.L. Snchez-Rojas, A. Sacedn, E. Muoz, A. Sanz-Hervs, M. Aguilar, and B.W. Kim. Direct determination of the piezoelectric field in (111) strained ingaas/gaas multiple quantum well p-i-n structures by photoreflectance. *Microelectronic Engineering*, 4344(0):171 – 177, 1998. ISSN 0167-9317. doi: http://dx.doi.org/10.1016/S0167-9317(98)00160-9. URL http://www.sciencedirect.com/science/article/pii/S0167931798001609.

[61] C. Van Hoof, K. Deneffe, J. De Boeck, D. J. Arent, and G. Borghs. Franz–keldysh oscillations originating from a well-controlled electric field in the gaas depletion region. *Applied Physics Letters*, 54(7):608–610, 1989. doi: 10.1063/1.100893. URL http://link.aip.org/link/?APL/54/608/1.

[62] X. Yin, H-M. Chen, F. H. Pollak, Y. Chan, P. A. Montano, P. D. Kirchner, G. D. Pettit, and J. M. Woodall. Photoreflectance study of surface photovoltage effects at (100)GaAs surfaces/interfaces. *Applied Physics Letters*, 58(3):260–262, 1991. doi: 10.1063/1.104682. URL http://link.aip.org/link/?APL/58/260/1.

[63] M. Schmid, M. Oehme, M. Kaschel, J. Werner, E. Kasper, and J. Schulze. Franz-keldysh effect in germanium p-i-n photodetectors on silicon. In *Group IV Photonics*

(GFP), 2010 7th IEEE International Conference on, pages 329–331, 2010. doi: 10.1109/GROUP4.2010.5643337.

[64] Orest J. Glembocki. Modulation spectroscopy of semiconductor materials, interfaces, and microstructures: an overview. pages 2–30, 1990. doi: 10.1117/12.20833. URL +http://dx.doi.org/10.1117/12.20833.

[65] T. S. Wang, K. I. Lin, and J. S. Hwang. Characteristics of InGaPN/GaAs heterostructures investigated by photoreflectance spectroscopy. *Journal of Applied Physics*, 100 (9):093709, 2006. doi: 10.1063/1.2358327. URL http://link.aip.org/link/?JAP/100/093709/1.

[66] N. Pan, X. L. Zheng, H. Hendriks, and J. Carter. Photoreflectance characterization of AlGaAs/GaAs modulation-doped heterostructures. *Journal of Applied Physics*, 68 (5):2355–2360, 1990. doi: 10.1063/1.346544. URL http://link.aip.org/link/?JAP/68/2355/1.

[67] G. Sek, K. Ryczko, M. Motyka, J. Andrzejewski, K. Wysocka, J. Misiewicz, L. H. Li, A. Fiore, and G. Patriarche. Wetting layer states of inas/gaas self-assembled quantum dot structures: Effect of intermixing and capping layer. *Journal of Applied Physics*, 101(6):063539, 2007. doi: 10.1063/1.2711146. URL http://link.aip.org/link/?JAP/101/063539/1.

[68] M. Kaniewska, O. Engstrm, A. Barcz, and M. Pacholak-Cybulska. Electrical activity of deep levels in the presence of InAs/GaAs quantum dots. *Materials Science in Semiconductor Processing*, 9(13):36 – 40, 2006. ISSN 1369-8001. doi: http://dx.doi.org/10.1016/j.mssp.2006.01.004. URL http://www.sciencedirect.com/science/article/pii/S1369800106000084. 11th International Conference on Defects - Recognition Imaging and Physics in Semiconductors (DRIP-XI)Sept. 13-19 in Beijing.

[69] F. Guffarth, R. Heitz, A. Schliwa, O. Stier, N. N. Ledentsov, A. R. Kovsh, V. M. Ustinov, and D. Bimberg. Strain engineering of self-organized InAs quantum dots. *Phys. Rev. B*, 64:085305, Aug 2001. doi: 10.1103/PhysRevB.64.085305. URL http://link.aps.org/doi/10.1103/PhysRevB.64.085305.

[70] G Sek, K Ryczko, J Misiewicz, M Bayer, F Klopf, J.P Reithmaier, and A Forchel. Photoreflectance spectroscopy of vertically coupled InGaAs/GaAs double quantum dots. *Solid State Communications*, 117(7):401 – 406, 2001. ISSN 0038-1098. doi: http://dx.doi.org/10.1016/S0038-1098(00)00490-7. URL http://www.sciencedirect.com/science/article/pii/S0038109800004907.

[71] Lionel Aigouy, Todd Holden, Fred H. Pollak, N. N. Ledentsov, W. M. Ustinov, P. S. Kop'ev, and D. Bimberg. Contactless electroreflectance study of a vertically coupled quantum dot-based InAs/GaAs laser structure. *Applied Physics Letters*, 70 (25):3329–3331, 1997. doi: 10.1063/1.119160. URL http://link.aip.org/link/?APL/70/3329/1.

[72] D. Huang, D. Mui, and H. Morkoç. Interference effects probed by photoreflectance spectroscopy. *Journal of Applied Physics*, 66(1):358–361, 1989. doi: 10.1063/1.343882. URL http://link.aip.org/link/?JAP/66/358/1.

[73] N. Kallergi, B. Roughani, J. Aubel, and S. Sundaram. Correlation of interference effects in photoreflectance spectra with GaAs homolayer thickness. *Journal of Applied Physics*, 68(9):4656–4661, 1990. doi: 10.1063/1.346176. URL http://link.aip.org/link/?JAP/68/4656/1.

[74] G. Blume, T. J. C. Hosea, and S. J. Sweeney. A study of the low-energy interference oscillations in photoreflectance of gaassb/gaas quantum well structures. *physica status solidi (a)*, 202(7):1244–1254, 2005. ISSN 1862-6319. doi: 10.1002/pssa.200460904. URL http://dx.doi.org/10.1002/pssa.200460904.

[75] Gwo-Jen Jan, Kuo-Tung Hsu, Poh-Kun Tseng, Chung-Ping Liu, and I-Fan Chang. Angle dependence of photoreflectance on gaas multiple quantum wells. pages 200–206, 1990. doi: 10.1117/12.20848. URL +http://dx.doi.org/10.1117/12.20848.

[76] T. Sauncy, C. P. Palsule, M. Holtz, S. Gangopadhyay, and S. Massie. Lifetime studies of self-activated photoluminescence in heavily silicon-doped GaAs. *Phys. Rev. B*, 53:1900–1906, Jan 1996. doi: 10.1103/PhysRevB.53.1900. URL http://link.aps.org/doi/10.1103/PhysRevB.53.1900.

[77] R. Heitz, M. Veit, N. N. Ledentsov, A. Hoffmann, D. Bimberg, V. M. Ustinov, P. S. Kop'ev, and Zh. I. Alferov. Energy relaxation by multiphonon processes in InAs/GaAs quantum dots. *Phys. Rev. B*, 56:10435–10445, Oct 1997. doi: 10.1103/PhysRevB.56.10435. URL http://link.aps.org/doi/10.1103/PhysRevB.56.10435.

[78] Y.P. Varshni. Temperature dependence of the energy gap in semiconductors. *Physica*, 34(1):149 – 154, 1967. ISSN 0031-8914. doi: http://dx.doi.org/10.1016/0031-8914(67)90062-6. URL http://www.sciencedirect.com/science/article/pii/0031891467900626.

[79] Temperature dependence of the bandgap I. URL http://www.iue.tuwien.ac.at/phd/palankovski/node37.html.

[80] Temperature dependence of the bandgap II. URL http://ecee.colorado.edu/~bart/book/eband5.htm.

[81] D.J. Ashen, P.J. Dean, D.T.J. Hurle, J.B. Mullin, A.M. White, and P.D. Greene. The incorporation and characterisation of acceptors in epitaxial GaAs. *Journal of Physics and Chemistry of Solids*, 36(10):1041 – 1053, 1975. ISSN 0022-3697. doi: http://dx.doi.org/10.1016/0022-3697(75)90043-8. URL http://www.sciencedirect.com/science/article/pii/0022369775900438.

[82] H. Künzel and K. Ploog. The effect of As_2 and As_4 molecular beam species on photoluminescence of molecular beam epitaxially grown GaAs. *Applied Physics*

Letters, 37(4):416–418, 1980. doi: 10.1063/1.91927. URL http://link.aip.org/link/?APL/37/416/1.

[83] Akira Takamori, Eizo Miyauchi, Hiroshi Arimoto, Yasuo Bamba, and Hisao Hashimoto. Gaas molecular beam epitaxy on be implanted GaAs layers. *Japanese Journal of Applied Physics*, 22(Part 2, No. 8):L520–L522, 1983. doi: 10.1143/JJAP.22.L520. URL http://jjap.jsap.jp/link?JJAP/22/L520/.

[84] D. C. Reynolds, D. C. Look, R. Kaspi, and D. N. Talwar. Phonon replicas in the photoluminescence emission of $Al_xGa_{1-x}As$ alloys. *Applied Physics Letters*, 66 (25):3447–3449, 1995. doi: 10.1063/1.113383. URL http://link.aip.org/link/?APL/66/3447/1.

Appendix A: First and Second Optical Setup

First setup. Optical design for this setup can be seen in figure A.1. This is the simplest setup and does not use OAP 15° and concave mirror (f=50 cm), compared to other second and third setup. Figure A.1a shows the proposed optical design, and the simulation result is depicted in figure A.1b.

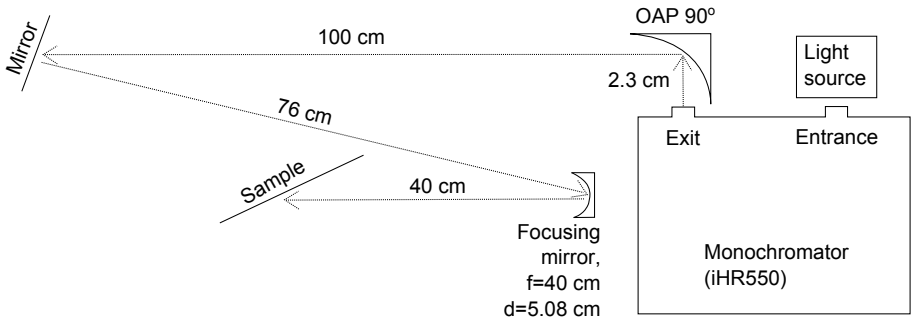

(a) First setup of proposed optical design.

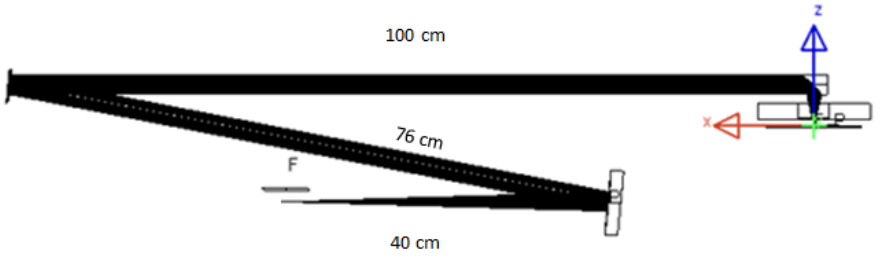

(b) Simulation of first setup optical design.

Figure A.1: First setup.

Diverged light which comes out from exit slit of monchromator to OAP 90° in figure A.1b are transformed to perfect collimated light. In experimental work, this result is not able to obtain, meaning that the light reflected from this parabolic mirror is still deviating, becomes bigger as the increasing distance. Nevertheless, the outcome with OAP 90° is much tolerable (lost of light intensity is not encountered in the flat mirror) compared with the light guiding without this component.

This setup requires lot of space, where one flat mirror placed 100 cm in front of the OAP 90°, as we can see in figure A.1. This placement is envitable, since the clear area

(similar to figure 3.12) of the focusing mirror (f=40 cm, d=2 inch=5.08 cm) required to be filled with light from the flat mirror (the area of optical component surface is designed such that light fill the clear area). With entrance and exit slit width of 0.7 mm, it produces spot with the size 2×2 mm^2 observed in the sample (denoted as F in figure A.1b). If the flat mirror is placed closer to the OAP 90°, the focused light will get bigger, while no impact found if it shifted further away from OAP 90°. This setup has major flaw, where it requires big space and it is not efficient at all.

Second setup. Responsing unfavorable circumstance fact in the first setup, major change of optical components position are taken as well as introducing OAP 15° and another flat mirror. The idea of utilizing OAP 15° is correcting effort to the imperfect collimated light from the OAP 90°, in addition to reduce distance of the flat mirror with respect to the OAP 90°, shown in figure A.2. The proposed setup and simulation result are shown in figure A.2a and A.2b, respectively.

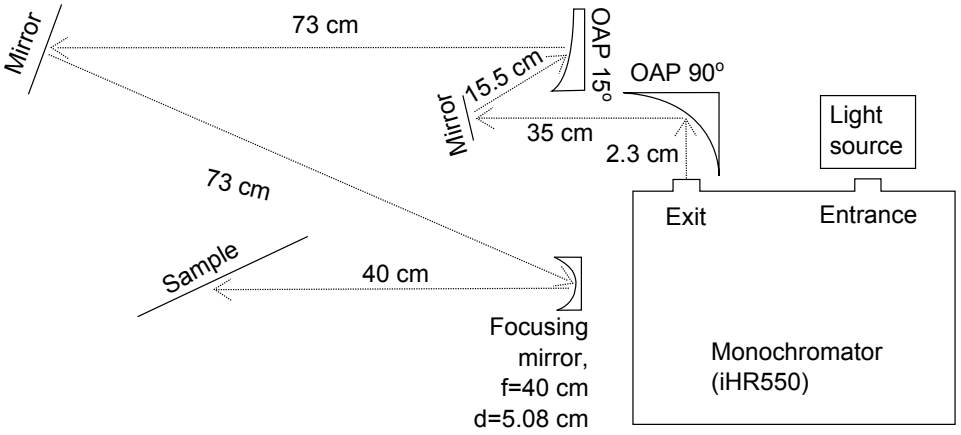

(a) Second setup of proposed optical design.

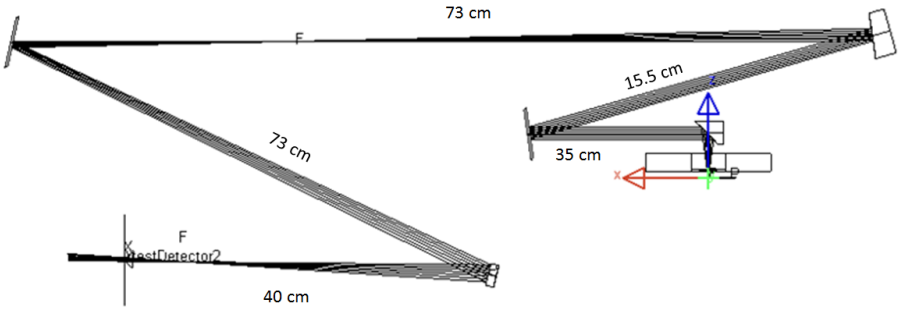

(b) Simulation of second setup optical design.

Figure A.2: Second setup.

The additional flat mirror and OAP 15° gives extra distance for the light rays to travel, which is compensating 27 cm shorter compared to first setup. Spot size measured in the sample is 2.5 × 3.75 mm^2 with the entrance slit width and exit slit width of 3 mm and 0.3 mm, respectively. The spot size for this setup is bigger than the first setup, which was 2×2 mm^2, but this lacked result is remunerated by the compactness of the setup. This setup is not adequate with the future use, because of the space between focusing mirror (f=40 cm) and the sample are too narrow to be filled with other components such as polarizers and/or wave retarders.

Appendix B: Complete Set of Photoreflectance Spectrum

Sample 1:1 (AS564)

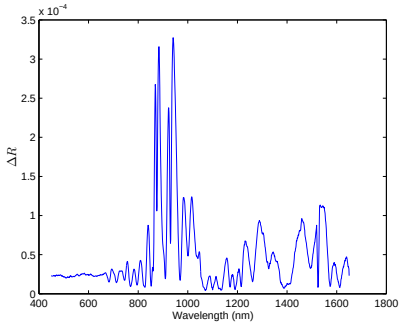

(a) Modulation reflection spectrum.

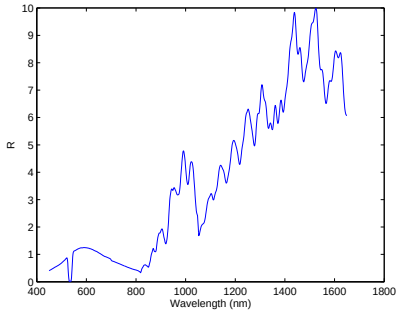

(b) Reflection spectrum.

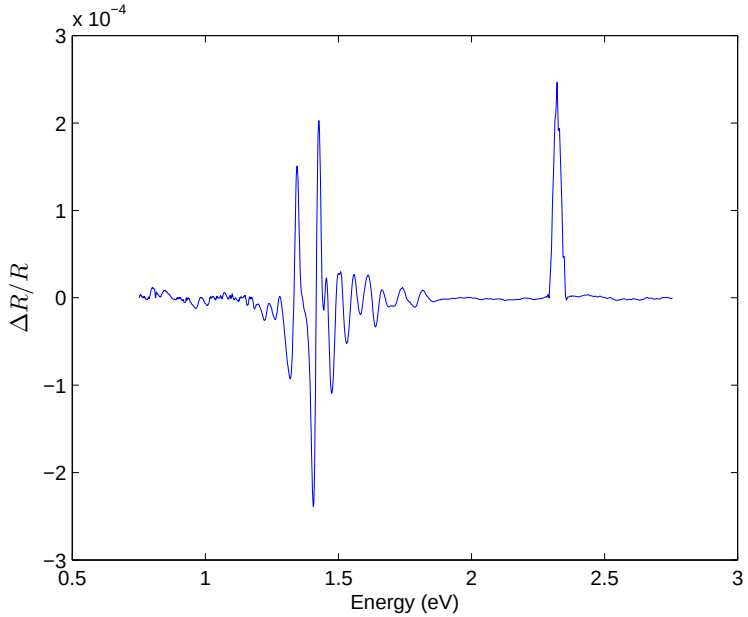

(c) PR spectrum.

Figure B.1: Spectrum set of sample 1:1.

Sample 1:2 (AS579)

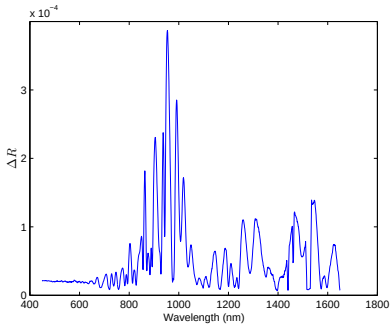

(a) Modulation reflection spectrum.

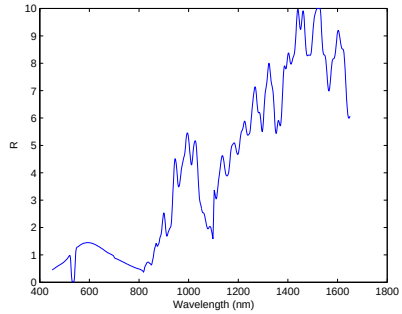

(b) Reflection spectrum.

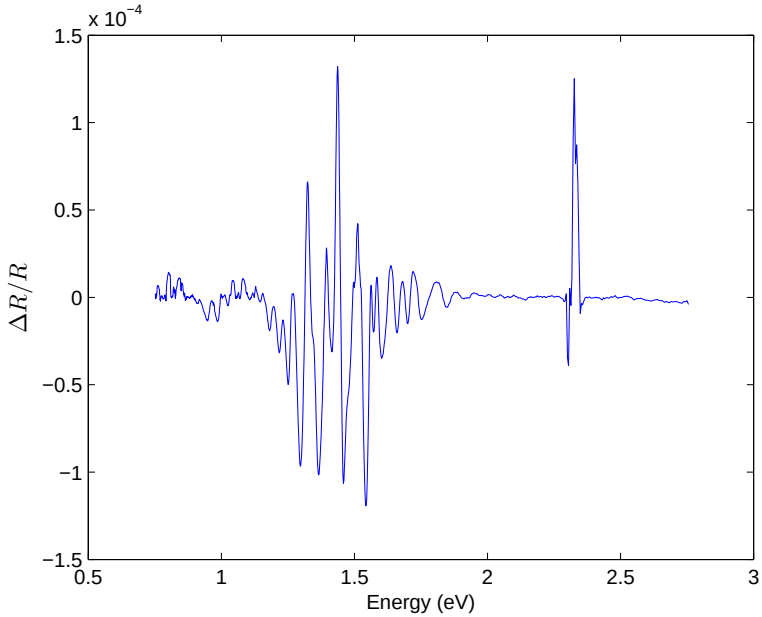

(c) PR spectrum.

Figure B.2: Spectrum set of sample 1:2.

Sample 1:3 (AS566)

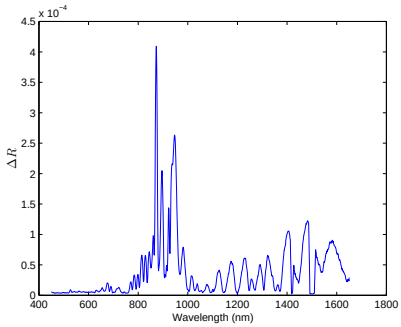

(a) Modulation reflection spectrum.

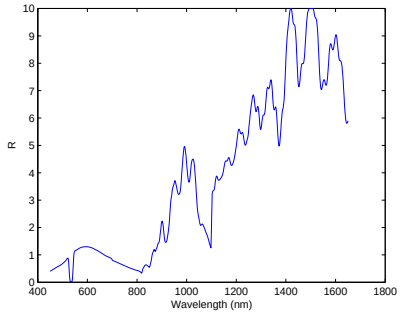

(b) Reflection spectrum.

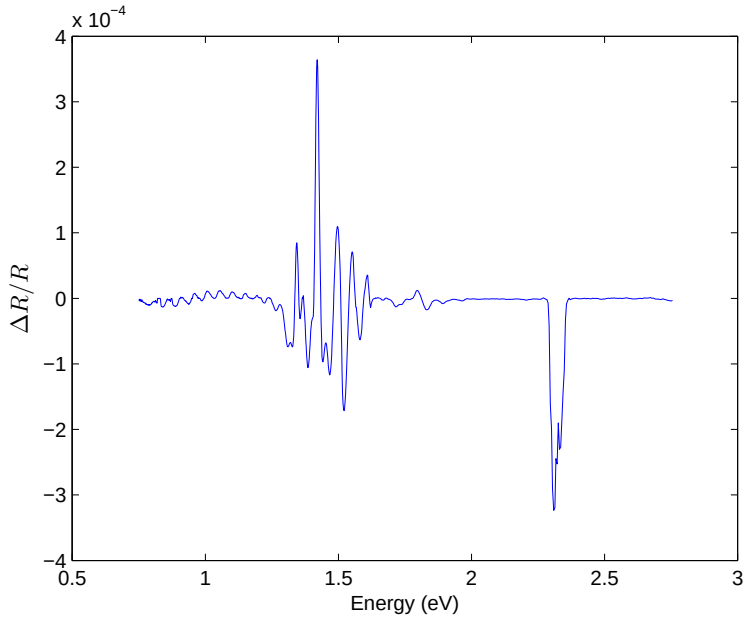

(c) PR spectrum.

Figure B.3: Spectrum set of sample 1:3.

Sample 1:4 (AS570)

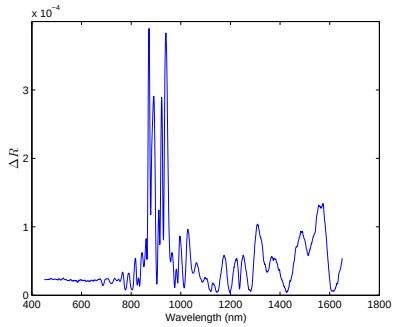

(a) Modulation reflection spectrum.

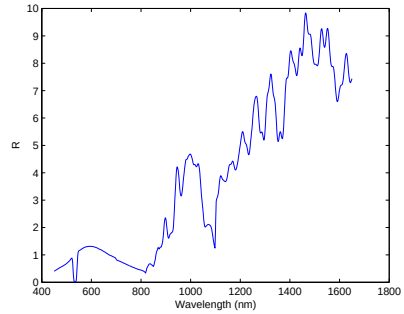

(b) Reflection spectrum.

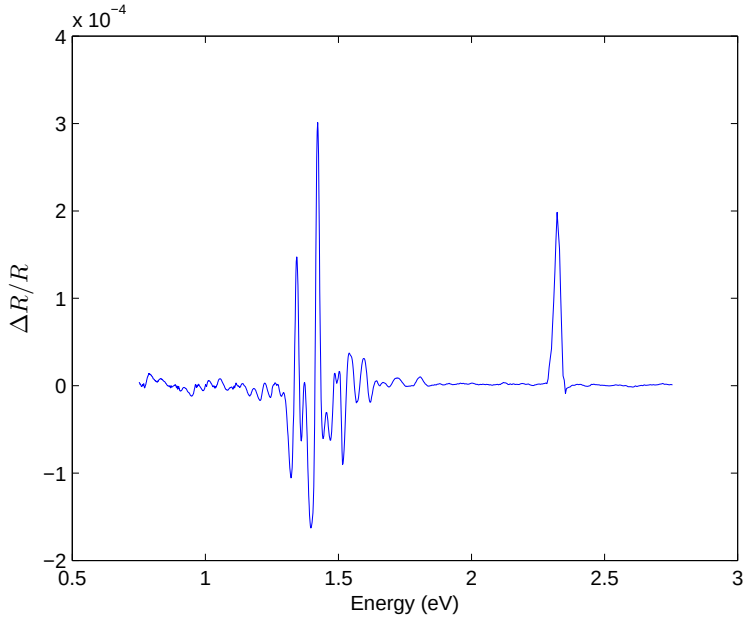

(c) PR spectrum.

Figure B.4: Spectrum set of sample 1:4.

Sample 1:5 (AS568)

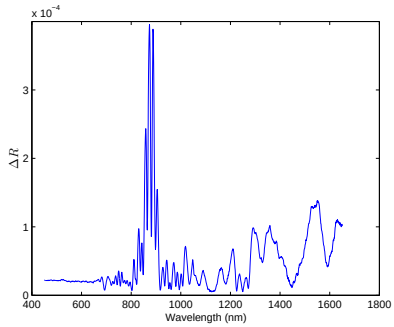

(a) Modulation reflection spectrum.

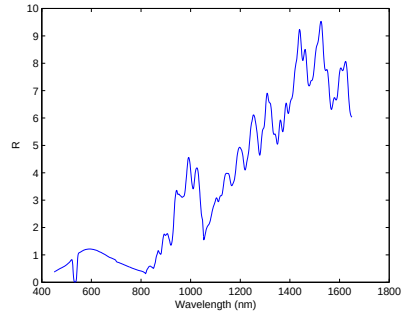

(b) Reflection spectrum.

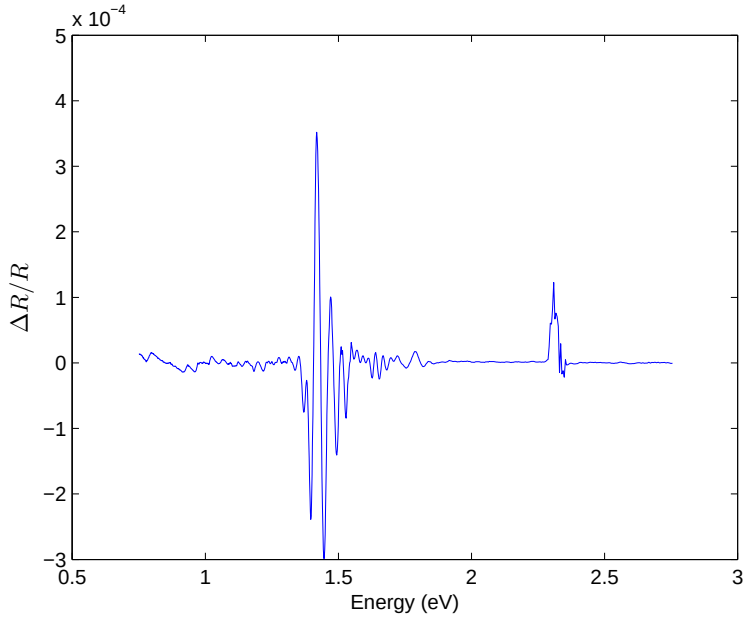

(c) PR spectrum.

Figure B.5: Spectrum set of sample 1:5.

Appendix C: Photoluminescence Setup

The PL carried out in the chapter 5.2 has the setup depicted in figure C.1,

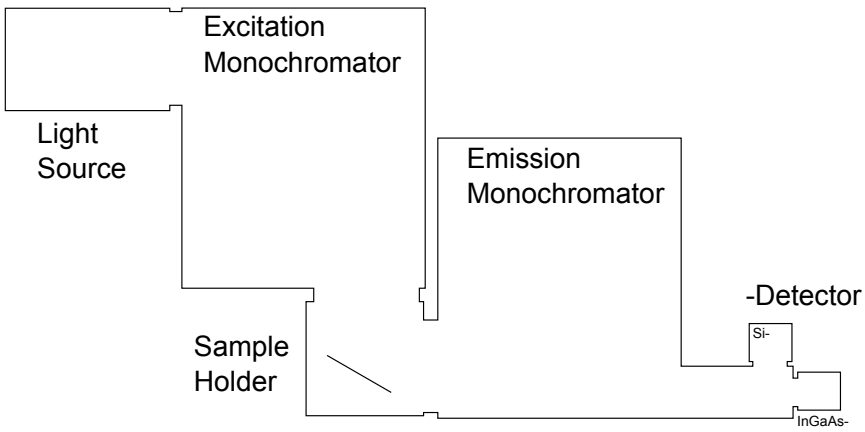

Figure C.1: PL setup.

The concept of the PL is obtaining excited states while avoiding temperature increment which turns to peaks broadening. It has the ability to adjust the excitation source, namely a tunable excitation source. For this purpose, utilized light source is a broadband source of Xenon lamp, where the excitation wavelength is selected using excitation monochromator. The selected wavelength will then transmitted to sample and if the excitation energy is resonant with excited state of transitions of the sample, photons will be absorbed, and electron-hole pairs are created. The pairs will relax rapidly to the ground state, where the recombination process occured and thus luminescence takes place. The emitted light from the sample will go to the emission monochromator, in which only narrow wavelength can pass and recorded in the detector. Since the detector records only light from ground state emission, the displayed spectrum will give emission peaks at the position energy of excited states [12]. It is possible to find more than one peak in the PL spectrum in heterostructure material, since it is composed of more than one atom, which each of them has different energy bandgap. It indicates that there are many transitions will take place over one sample, and they are recorded in detector as the emitted photons from each transition satisfy selected emission wavelengths of monochromator. there are two types of detector being employed in here: Si (300 nm - 1100 nm) and InGaAs (800 nm - 1750 nm).

The measurement are taken both in room-temperature and low-temperature (achieved at 7 K), which the result introduced in chapter 5.2 only for the room-temperature of sample 1:1. The low-temperature result show results which are hard to analysis, since this is the

first PL result carried out in the Prof. Turrid laboratory, in which the setup needs further study and calibration for the low-temperature condition, therefore no further analysis being conducted. In this part, the PL measurement data for all samples at room-temperature and sample 1:1 at low-temperature will be presented. The PL setting are described as follows,

Table C.1: PL setting at room-temperature

Parameter	Excitation	Emission
Wavelength (nm) / Energy (eV)	520-800 /1.55-2.38	700-1500 / 0.83-1.77
Increment (nm)	20	2
Side entrance slit (nm)	10	10
Front entrance slit (nm)	10	10
Side exit slit (nm)	10	10
Grating Density (Blaze)	1200 (330)	600 (1000)
Detector	–	InGaAs

From the figure C.2 - figure C.6, they shows their unique PL spectra. The analysis of the sample has been done in sample 1:1, explained in section 5.2. The results of all samples are given as follows,

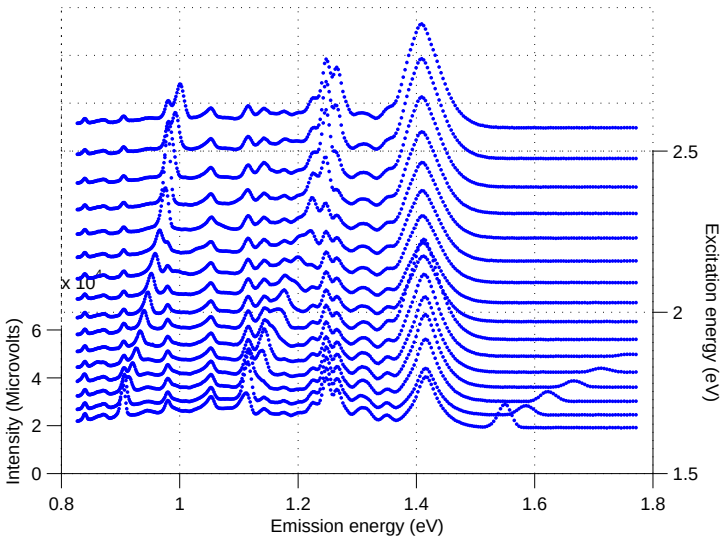

Figure C.2: PL of sample 1:1.

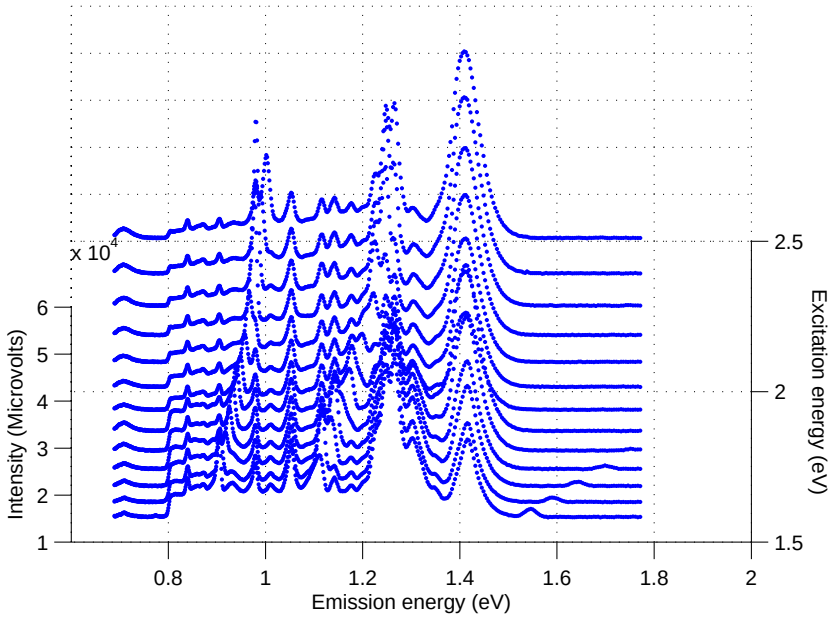

Figure C.3: PL of sample 1:2.

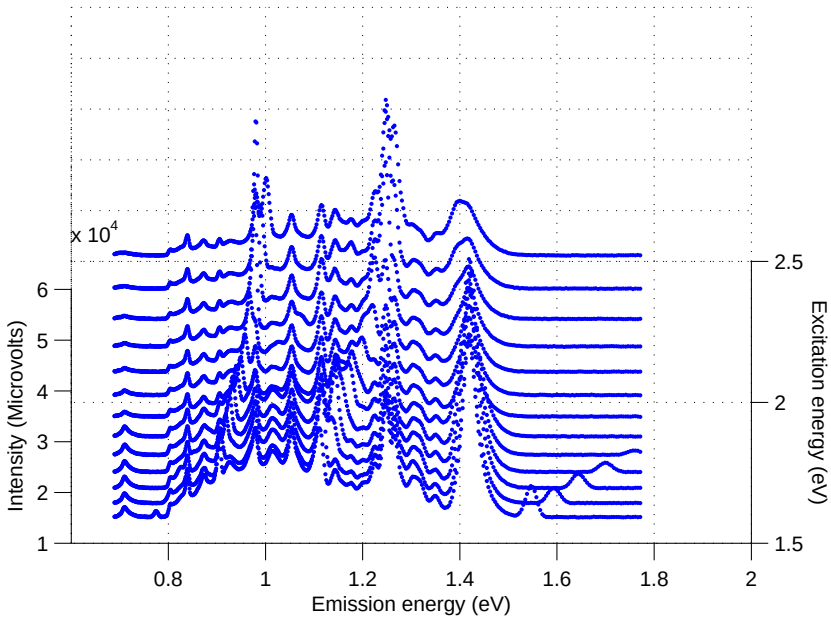

Figure C.4: PL of sample 1:3.

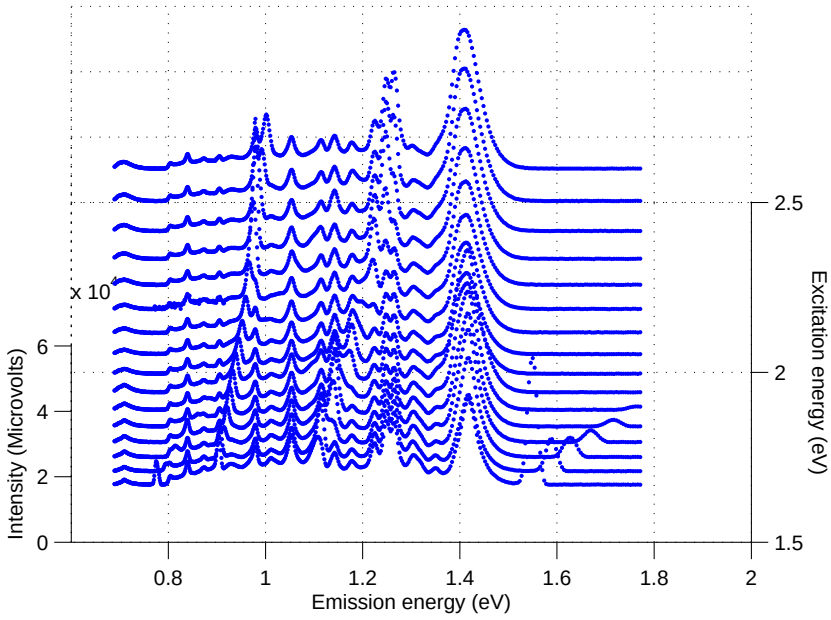

Figure C.5: PL of sample 1:4.

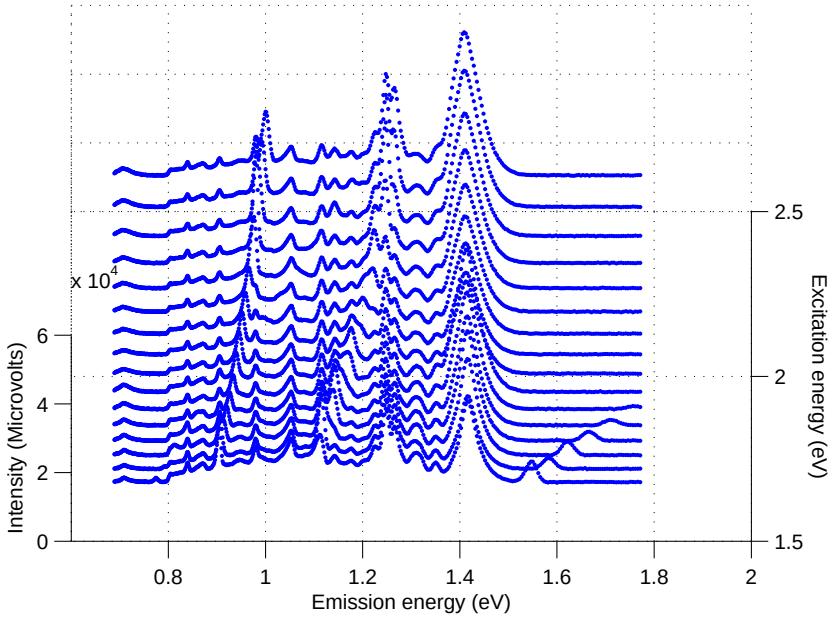

Figure C.6: PL of sample 1:5.

The low-temperature measurement is conveyed by isolating the sample in chamber, where the temperature inside controlled to become 7 K. The parameters are given in table C.2. Sample 1:1 is the only sample measured in this condition. The measurement is not further continued due to the complexity and abrupt result. The result shown in figure C.7 is for the excitation energy of the 1.72 eV, with the emission energy from 0.8 eV - 1.67 eV. As the excitation energy getting higher, the expected WL vanishes. The research finding indicates location of the GaAs and WL at 1.265 eV and 0.95 eV, which supposed to be at 1.493 eV and 1.34 eV, respectively [10]. Owing to this conclusion, low-temperature PL measurement required to be calibrated and studied for the future use.

Table C.2: PL setting at low-temperature

Parameter	Excitation	Emission
Wavelength (nm) / Energy (eV)	720 / 1.72	740-1500 / 0.8-1.67
Increment (nm)	20	2
Side entrance slit (nm)	5	5
Front entrance slit (nm)	5	5
Side exit slit (nm)	5	5
Grating Density (Blaze)	1200 (330)	600 (1000)
Detector	–	InGaAs

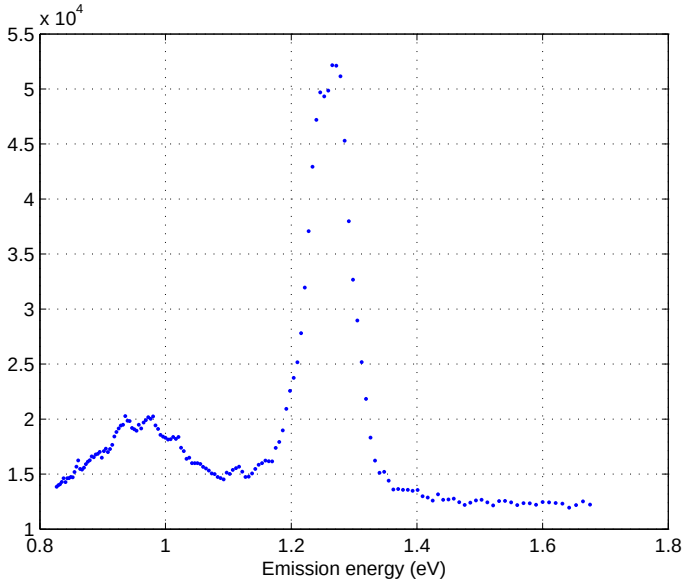

Figure C.7: PL at low-temperature of sample 1:1.